A&A 664, A73 (2022)
https://doi.org/10.1051/0004-6361/202142554

Astronomy & Astrophysics

The ALMA-ALPINE [CII] survey

The star formation history and the dust emission of star-forming galaxies at $4.5 < z < 6.2$*

D. Burgarella[1], J. Bogdanoska[1], A. Nanni[2], S. Bardelli[3], M. Béthermin[1], M. Boquien[4], V. Buat[1,32], A. L. Faisst[5], M. Dessauges-Zavadsky[6], Y. Fudamoto[7,8], S. Fujimoto[9,10], M. Giavalisco[11], M. Ginolfi[12], C. Gruppioni[13], N. P. Hathi[14], E. Ibar[15], G. C. Jones[16,17], A. M. Koekemoer[14], K. Kohno[18,19], B. C. Lemaux[20,21], D. Narayanan[22], P. Oesch[6,9,10], M. Ouchi[18,23,24], D. A. Riechers[25], F. Pozzi[3,26], M. Romano[2,27,28], D. Schaerer[6,29], M. Talia[3,30], P. Theulé[1], D. Vergani[3], G. Zamorani[3], E. Zucca[3], P. Cassata[31], and the ALPINE team

(Affiliations can be found after the references)

Received 30 October 2021 / Accepted 8 February 2022

ABSTRACT

Star-forming galaxies are composed of various types of galaxies. However, the luminosity functions at $z \gtrsim 4$–5 suggest that most galaxies have a relatively low stellar mass ($\log M_{\rm star} \sim 10$) and a low dust attenuation ($A_{\rm FUV} \sim 1.0$). The physical properties of these objects are quite homogeneous. We used an approach where we combined their rest-frame far-infrared and submillimeter emissions and utilized the universe and the redshift as a spectrograph to increase the amount of information in a collective way. From a subsample of 27 ALMA-detected galaxies at $z > 4.5$, we built an infrared spectral energy distribution composite template. It was used to fit, with CIGALE, the 105 galaxies (detections and upper limits) in the sample from the far-ultraviolet to the far-infrared. The derived physical parameters provide information to decipher the nature of the dust cycle and of the stellar populations in these galaxies. The derived IR composite template is consistent with the galaxies in the studied sample. A delayed star formation history with $\tau_{\rm main} = 500$ Myr is slightly favored by the statistical analysis as compared to a delayed with a final burst or a continuous star formation history. The position of the sample in the star formation rate (SFR) versus $M_{\rm star}$ diagram is consistent with previous papers. The redshift evolution of the $\log M_{\rm star}$ versus $A_{\rm FUV}$ relation is in agreement with an evolution in redshift of this relation. This evolution is necessary to explain the cosmic evolution of the average dust attenuation of galaxies. Evolution is also observed in the $L_{\rm dust}/L_{\rm FUV}$ (IRX) versus UV slope $\beta_{\rm FUV}$ diagram: younger galaxies have bluer $\beta_{\rm FUV}$. We modeled the shift of galaxies in the IRX versus the $\beta_{\rm FUV}$ diagram with the mass-weighted age as a free parameter, and we provide an equation to make predictions. The large sample studied in this paper is generally consistent with models that assume rapid dust formation from supernovae and removal of dust by outflows and supernovae blasts. However, we find that high mass dusty star-forming galaxies cannot be explained by the models.

Key words. galaxies: formation – galaxies: evolution – early Universe – submillimeter: galaxies – ultraviolet: galaxies – infrared: galaxies

1. Introduction

Since the very first papers (e.g., Madau et al. 1996) on high redshift galaxies such as the Lyman break galaxies (LBGs), the issue of how much of their energy is emitted in the far-infrared (far-IR) has been an open question in the early universe. Today, a new question is coming to the forefront and we wonder what the dust cycle in high redshift galaxies is, that is how are large dust masses of dust formed at very high redshifts and efficiently destroyed or removed later, and what are the characteristics of these dust grains.

Thanks to deep observations with the *Herschel* space observatory (*Herschel*), the Atacama Large Millimeter/Submillimiter Array (ALMA) in the Southern Hemisphere, and the Northern Extended Millimeter Array (NOEMA) in the Northern Hemisphere, we have started to explore the dusty part of the spectral energy distributions (SEDs) of high redshift star-forming galaxies (Hiz-SFGs; Bouwens et al. 2016; Burgarella et al. 2020; Sugahara et al. 2021; Hashimoto et al. 2019; Koprowski et al. 2020; Faisst et al. 2020a,b, and others) to obtain an overall view of the energy budget of normal star-forming galaxies in the early universe.

Still, except for lensed objects, targeted studies are not very successful and most of the Hiz-SFGs are not individually detected in the rest-frame far-IR, that is in the observed submillimeter (submm) and millimeter ranges (e.g., Bouwens et al. 2016; Bethermin et al. 2020; Burgarella et al. 2020; Faisst et al. 2020b). Stacking remains the preferred tool to learn what the statistical dust properties of these galaxies are (e.g., Álvarez-Márquez et al. 2016, 2019; Carvajal et al. 2020).

Another interesting way to study these objects is through the far-IR fine-structure lines. These lines have been observed with the aim of understanding the interstellar medium properties and gas cooling in the neutral and ionized phases of local low-metallicity star-forming galaxies (e.g., Madden et al. 2013; Cormier et al. 2019; Fernández-Ontiveros et al. 2016). In the high redshift universe, several of these lines have also been identified (Harikane et al. 2014; De Breuck et al. 2019; Cunningham et al. 2020; Pavesi et al. 2019, for instance). We note that [OIII]88 µm is very strong and may be the most intense line at high redshift where we expect that most galaxies contain a large population of O stars and have a low metallicity (Arata et al. 2020). Attempts at detecting [OIII]88 µm

* Full Tables D.1, E.1, and E.2 are only available at the CDS via anonymous ftp to cdsarc.u-strasbg.fr (130.79.128.5) or via http://cdsarc.u-strasbg.fr/viz-bin/cat/J/A+A/664/A73

have indeed been quite successful (e.g., Inoue et al. 2016; Hashimoto et al. 2019; Álvarez-Márquez et al. 2019). Since some of these lines (e.g., [OIII]88 µm and [CII]158 µm) are correlated with the star formation rate (SFR) of the galaxies, they can also be helpful when performing SED fitting by providing additional constraints on the recent SFR. Recently, the ALPINE-ALMA [CII] survey (Le Fèvre et al. 2020; Faisst et al. 2020a; Bethermin et al. 2020) initiated an effort to detect the [CII]158 µm line of 118 Hiz-SFGs in the redshift range $4.4 < z < 5.9$. The [CII]158 µm line is one of the dominant gas coolants (Lagache et al. 2018). This line is detected in the ALPINE observations with an overall detection rate of 64% and a signal-to-noise ratio (S/N) threshold larger than 3.5σ. The ALPINE observations also allowed for the dust continuum of 23 of the 118 galaxies above 3.5σ to be detected (Bethermin et al. 2020).

The dust mass ($M_{\rm dust}$) can be estimated from the observed flux density once we can assume a dust temperature ($T_{\rm dust}$) and other dust-related physical parameters (e.g., Pozzi et al. 2021). However, even though it might seem obvious, estimating $M_{\rm dust}$ is much safer when using multiple data from the far-IR SEDs at different wavelengths. There is some degeneracy between $T_{\rm dust}$ and $M_{\rm dust}$, and more than a few data points lying both on the Rayleigh-Jeans (RJ) side, above the wavelength of the peak of the dust emission and on the Wien side, and below the peak wavelength of the dust emission. This information is important to constrain the SED (Liang et al. 2019). Because the individual approach is still quite a difficult task when dealing with the dust emission of galaxies close to or in the epoch of reionization (EoR), we need to combine the information from individual galaxies – assuming they share characteristic dust emission – to improve our wavelength coverage.

In this paper, we adopt a statistical approach using a sample of ALMA-observed high-redshift star-forming galaxies (ALPINE, Le Fèvre et al. 2020) the methodology already described in Burgarella et al. (2020) and Nanni et al. (2020). The redshifts of the final sample cover a range $4.5 \lesssim z \lesssim 6.2$ near or in the EoR that will be explored by the *James Webb* Space Telescope (JWST). The ALPINE sample is a unique source of data, which we combined to the one from Burgarella et al. (2020)[1] to build an IR composite template corresponding to the characteristic far-IR dust emission of Hiz-SFGs in the early universe. Some original works (e.g., Ouchi et al. 1999) have tried to use local starburst galaxies to build such templates and therefore estimate upper limits of submm flux densities. Similar to in Shapley et al. (2003) where a high S/N spectrum of $z \sim 3$ LBGs was derived, and even in a more similar way in Pearson et al. (2013) in which 40 H-ATLAS sources with previously measured redshifts in the range $0.5 < z < 4.2$ were used to derive a suitable average template for high-redshift H-ATLAS sources, the observed data from our sample were used to build the template.

In addition to using the composite IR SED to derive the dust properties of the galaxies via SED fitting, these data are also unique to help understand the stellar populations of these Hiz-SFGs and to calibrate important diagnostic diagrams in the early universe. Once an IR composite template is safely estimated from the observed ALMA detection, the spectral information in the rest-frame ultraviolet (UV), optical, and near IR is combined and we can come back to the individual approach to fit each galaxy.

[1] The combined ALPINE plus Burgarella et al. (2020) and Nanni et al. (2020) samples studied in this paper are referred to as our sample hereafter.

In this paper, we assume a Chabrier initial mass function (IMF, Chabrier 2003). We use WMAP7 cosmology (Komatsu et al. 2011).

2. The sample of studied galaxies

The ALPINE sample is representative of the overall Hiz-SFGs population in the redshift range $4.5 \lesssim z \lesssim 5.5$. It is not dominated by IR-bright (i.e., in dust continuum) submm galaxies (SMGs). The ALPINE galaxies are mainly located on or near the main sequence (e.g., Rodighiero et al. 2011; Gruppioni et al. 2013; Donnari et al. 2019; Sherman et al. 2021) in the SFR versus stellar mass ($M_{\rm star}$) relation observed at these redshifts (Speagle et al. 2014; Pearson et al. 2018). It is mostly dominated by UV-selected galaxies (see Table 1 in Faisst et al. 2020a) with about 62% of the sample identified with the dropout technique, that is LBGs and 28% that are Lyman α emitters which were selected with narrow bands. We added, to the ALPINE galaxies, seven LBGs from Burgarella et al. (2020) and Nanni et al. (2020) to build our sample. The data of the latter seven LBGs were collected from several works (Bouwens et al. 2016; Capak et al. 2015; Faisst et al. 2017; Scoville et al. 2016; Willott et al. 2015; Hashimoto et al. 2018). This selection is certainly not complete and will very likely introduce biases on the results we obtained, but this is as good as we can currently do. The origins of the data are listed in Table 1.

Using Band-7 of ALMA, the ALPINE project observed a sample of galaxies with spectroscopic redshifts in two well-observed fields: 105 galaxies in the Cosmic Evolution Survey field (COSMOS, Scoville et al. 2007) and the remaining 13 in the Extended *Chandra* Deep Field South (ECDFS, Giacconi et al. 2002), with extensive multiband *Hubble* space telescope (HST) data from CANDELS (Grogin et al. 2011; Koekemoer et al. 2011). In this survey, 64% of the galaxies have been detected in [CII] at 3.5σ above the noise, as well as 21% of the galaxies detected in the continuum (S/N threshold corresponding to a 95% purity). The sample is divided into two redshift ranges at $4.40 < z < 4.65$ (median redshift $\langle z \rangle = 4.5$, containing 67 galaxies) and $5.05 < z < 5.90$ (median redshift $\langle z \rangle = 5.5$, containing 51 galaxies), separated by a gap in the transmission of the atmosphere. We note that type I active galactic nuclei (AGN), identified from broad spectral lines, are excluded from the present sample.

As the galaxies included in the ALPINE sample belong to well-studied fields, they come with a rich ancillary data set (Faisst et al. 2020a). Due to the nature of the selection of these galaxies, they all have spectroscopic observations in rest-frame UV, performed with the Keck telescope and the European Very Large Telescope (VLT). A plethora of photometric observations are also available, from ground-based observatories in the UV to optical, from the HST in the UV, as well as from *Spitzer* above the Balmer break (all rest-frame features).

3. Methodology

The objective of the paper is to study the physical properties of the sample of Hiz-SFGs, and more specifically their stellar populations and dust grains. Because we do not have a wide wavelength coverage of their IR dust emission, we built an IR composite template from the subsample of ALMA-detected objects. To this aim, we applied the methodology described in Fig. 1 and it is detailed.

Table 1. Origins of the data used in this paper.

Source	Number of objects	Selection	Redshift	Notes
Le Fèvre et al. (2020); Faisst et al. (2020a); Bethermin et al. (2020)	118	SFG	$z \sim 4.5$	– 20 ALMA-7 detections with S/N > 3
			$z \sim 5.5$	– 78 ALMA-7 upper limits – 18 ALMA-7 not selected (not enough data) – $S/N_{UV\text{-}optical\text{-}NIR} > 2.5$. – SFG with > 5 data points in UV-optical only – [CII]158 µm measurements for 64% of the sample
Capak et al. (2015); Faisst et al. (2017)	4 (HZ4, HZ6, HZ9, HZ10	UV	$z \sim 5.6$	– [CII]158 µm for all Hi-z LBGs – ALMA-7 detections: HZ4, HZ6 (3) HZ9 & HZ10 (5) – ALMA-7 upper limits for the others – HZ5 detected in *Chandra* and not included in the sample – Additional data from Pavesi et al. (2016)
Scoville et al. (2016)	1 (566428)	UV	$z = 5.89$	– ALMA-6 detection – [CII]158 µm measurement
Willott et al. (2015)	2 (CLM1 & WMH5)	UV	$z \sim 6.1$	– ALMA-6 detections – [CII]158 µm measurement

Notes. The final sample used in this paper contains 105 objects: 27 with ALMA detections and 78 with ALMA upper limits. The other objects were discarded from the sample because they do not have enough data in the UV-optical-near-IR range to perform a safe SED fitting.

3.1. Building the IR composite template

3.1.1. Phase 0: Selection of the galaxies used to build the IR composite template

From the ALPINE sample and the one compiled by Burgarella et al. (2020), we selected the objects for which the dust continuum was detected with ALMA. More details on the selection are provided in Table 1. The final sample of ALMA-detected objects contains 27 galaxies.

3.1.2. Phase 1: CIGALE initial individual fits of ALMA-detected galaxies to estimate the normalization at $\lambda = 200\,\mu$m

The objective of this initial phase is to estimate a normalization factor for the SEDs of all the ALMA-detected galaxies. Galaxies with upper limits in the far-IR were not selected to build the IR composite SED. This normalization factor was derived from the estimated flux density at $\lambda = 200\,\mu$m (rest-frame), which is approximately the maximum wavelength above which we have no observed data. The SEDs of all the ALMA-detected objects at $\lambda = 200\,\mu$m were set to 1.0 to build the IR composite SED. All the other data were modified accordingly. The spectral models selected in this initial fit are described in detail in Appendix A. We selected a wide range of models, especially for the dust emission which is important for this work.

We fit all the ALMA-detected galaxies using several options with CIGALE (Burgarella et al. 2005; Boquien et al. 2009, see Appendix A for details on the priors for the models). CIGALE cannot model emission lines from photo-dissociation regions (PDRs). We used the [CII]158 µm fluxes to estimate the star formation rate ($SFR_{[CII]158\,\mu m}$), which we evaluated with the relation from Schaerer et al. (2020). These $SFR_{[CII]158\,\mu m}$ values, along with the associated uncertainties derived from the line uncertainties, were added as properties to constrain the CIGALE SED fitting[2]. To perform this analysis, we selected three types of dust emission available in CIGALE: (i) a mid-IR power law and a general modified blackbody (Casey 2012): PL+G_MBB, (ii) a mid-IR power law and an optically thin modified blackbody (Casey 2012): PL+OT_MBB, and, (iii) the models from Draine et al. (2014): DL2014.

It is specifically worth checking whether the prior assumptions made on the emissivity index (β_{RJ}) of the modified blackbody could bias the final result. We could not safely estimate β_{RJ} for the individual objects but we could do so better with the IR composite template because more data points are used, thus we also fixed $\beta_{RJ} = 1.0$, 1.5, and 2.0 to test the impact on the level of the luminosity at 200 µm (rest-frame) used for the normalization of the individual SEDs. Table 2 shows that the bias introduced by the initial prior on β_{RJ} is much lower that the uncertainties coming from the values derived by an SED fitting. However, we would like to stress that a wide range of SED shapes were used to estimate the normalization, including several β_{RJ}, T_{dust}, and DL2014 models.

3.1.3. Phase 2: Building of the IR composite template

In this second phase, we proceeded by actually building the observed composite IR template. For this, we made use of the normalized SEDs of each of the 27 ALMA-detected objects.

– Phase 2.1: Checking the homogeneity in the galaxy sample → IRV1 template: By making use of the normalization factors and benefiting from the redshift coverage ($4.3 < z < 6.2$), we

[2] By comparing the results of the fits with and without [CII]158 µm, we get the following: M_{star}([w/CII]) / M_{star}([w/CII]) = 0.90 ± 0.27, SFR([w/CII]) / SFR([w/CII]) = 1.22 ± 0.32, L_{dust}([w/CII]) / L_{dust}([w/CII]) = 1.22 ± 0.27, and L_{FUV}([w/CII]) / L_{FUV}([w/CII]) = 1.02 ± 0.02 with no significant difference for the selected dust emission type.

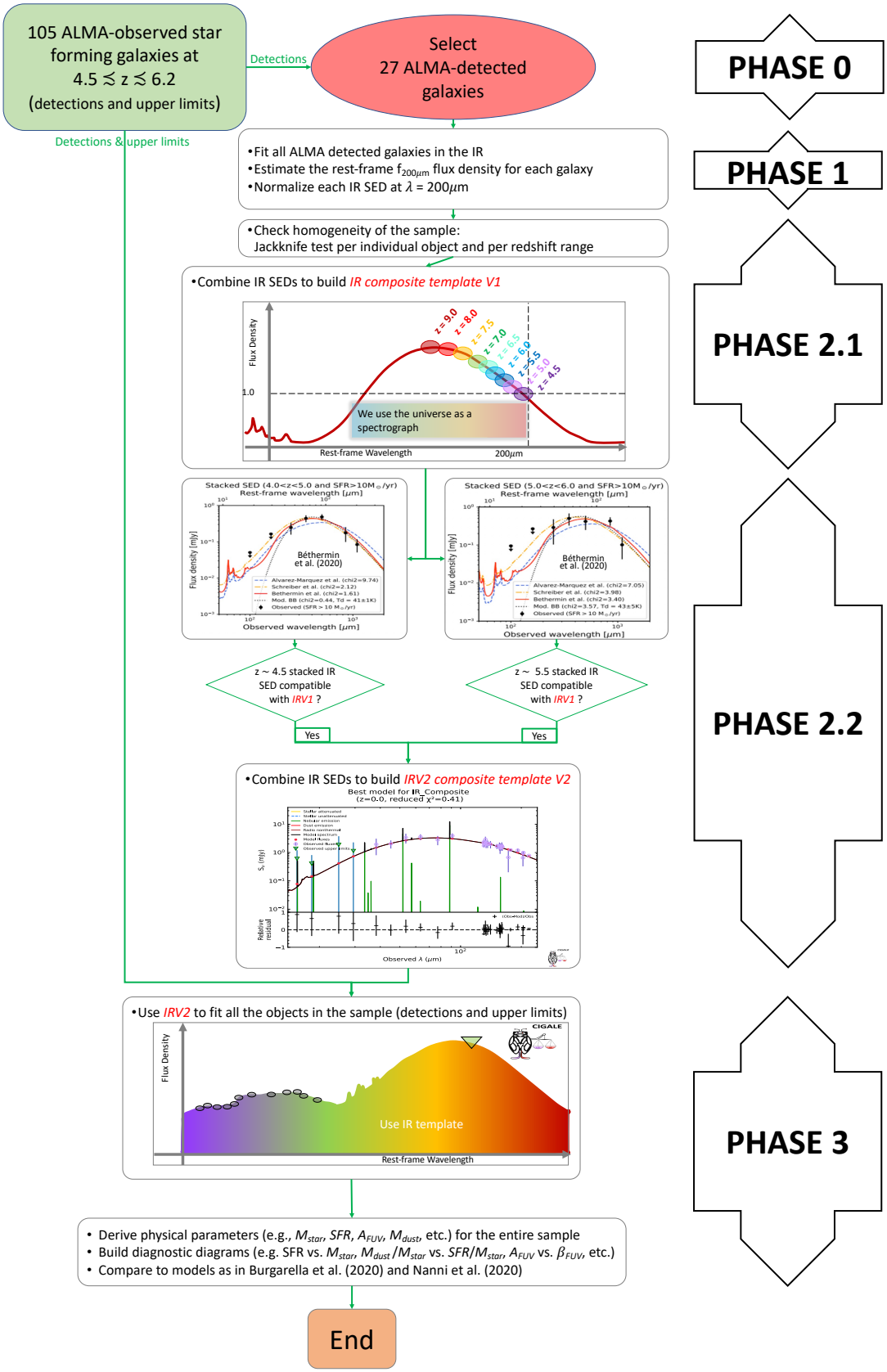

Fig. 1. Flow chart of the process followed to build the composite IR SED for the Hiz-SFGs sample. The various phases of this process are shown on the right side of the figures. They are also described in more detail in the text (see Sect. 3) In the first phase, we selected only ALMA-detected objects to build the first IR template (IRV1). Next, we added the data from the $z \sim 4.5$ and ~5.5 stacks from Bethermin et al. (2020) to build the second and final IR template (IRV2). Adding UV and optical data to IRV2, we fit the entire (detected and upper limits) sample.

Table 2. Parameters of the dust emission.

β_{RJ}	$\Delta L_{200\,\mu m} = \frac{\langle L_{200\,\mu m}\rangle - L^{\beta_{RJ}}_{200\,\mu m}}{\langle L_{200\,\mu m}\rangle}$	$\sigma(\Delta L_{200\,\mu m})$	$[\Delta L_{200\,\mu m}]_{err}$ from SED fitting
1.0	−0.022	0.118	0.501
1.5	−0.013	0.049	0.466
2.0	0.035	0.060	0.825

Notes. The results show that whatever the prior on the value of β_{RJ}, the dispersion on the resulting normalization factor is negligible and much smaller than the uncertainties on the luminosity at $\lambda = 200\,\mu m$ (rest frame) derived from the SED fitting and used for the normalization of the individual SEDs. This means that the method adopted to estimate the normalization factor does not significantly impact the shape of the final IR composite template.

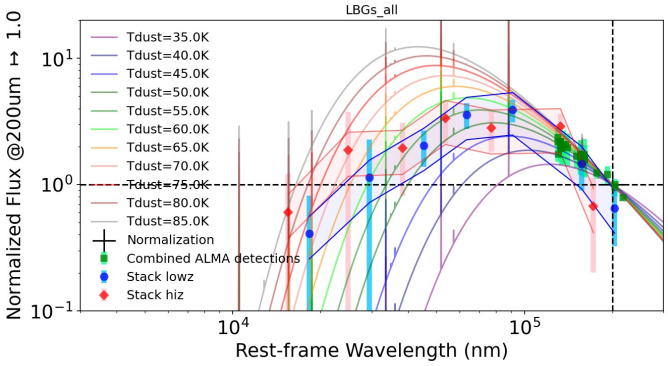

Fig. 2. IR combined SED built from the ALMA-detected objects from the ALPINE sample, from Burgarella et al. (2020), and with the two stacks from Bethermin et al. (2020) and the associated uncertainty regions. We note that the four left-most points for the stacks are upper limits, as shown by the error bars reaching the bottom of the figure. The SEDs corresponding to optically thin modified black bodies are superimposed to the observed SEDs. Qualitatively, we can see that the IR-combined SED seems to be in agreement with greenish modified blackbody SEDs, that is $T_{dust} \sim 50$–60 K. A qualitative analysis is performed later in this paper.

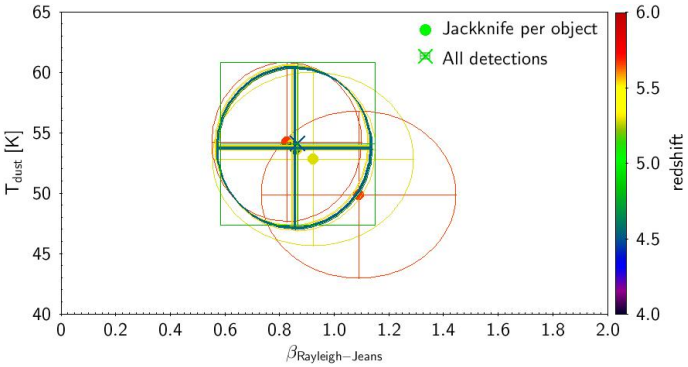

Fig. 3. Degeneracies in T_{dust} and β_{RJ}. The knife jacking method allowed us to estimate whether the characteristics of the dust emission, i.e., T_{dust} and β_{RJ}, vary when removing and adding back individual galaxies from the sample used to build the composite template. The ellipses show the uncertainties. The outlier point at $\beta_{RJ} \sim 1.1$ and $T_{dust} \sim 51$ K was obtained when taking off HZ10 at $z = 5.659$ with five pieces of data in the far-IR+submm range. Only when removing it did the average locus move to slightly larger values of β_{RJ}, but with larger uncertainties.

Table 3. Degeneracy of β_{RJ} and T_{dust}.

Removed z range	$N_{removed\text{-}obj}$	β_{RJ}	T_{dust}
$4.0 < z < 5.0$	62	0.84 ± 0.28	54.3 ± 6.7
$5.0 < z < 6.0$	41	1.30 ± 0.55	47.6 ± 8.4
$6.0 < z < 7.0$	2	0.85 ± 0.28	53.7 ± 6.6

Notes. Results of the knife jacking method applied on the entire sample when removing and adding back objects in the given redshift ranges from the first column to build the composite template. The dust parameters are stable. Even though it is still consistent with the other ones, the results without one redshift range (namely $5.0 < z < 6.0$) differ. This could be explained because the $5.0 < z < 6.0$ range contains the widest wavelength range and it is therefore more constraining to estimate β_{RJ} and T_{dust}. So, we cannot rule out a small variation of these two parameters with the redshift inside the quoted uncertainties.

used the universe as a spectrograph and we combined the SEDs of 27 ALMA-detected objects to form an initial version (IRV1) of the observed composite SED (Figs. 1 and 2). We note that this process is different from the stacking method whose aim is to detect the average flux density at a given wavelength of a sample of detected and/or undetected objects.

We began by verifying whether the subsample of ALMA-detected galaxies is homogeneous enough to build a single IR composite template. For instance, one single object or all the objects in a given redshift range might significantly impact the parameters of the dust emission and bias the IR composite template. Here, we only show the results of this test assuming PL+OT_MBB, but we checked that the results were the same regardless of the assumed dust emission option.

To reach this goal, we used the knife-jacking method, where we removed the SED of each galaxy (or a series of galaxies in a redshift range) sequentially from the list of objects, built the composite template, and fit it with CIGALE. Then, we put the removed objects back in the detected subsample and we reproduced this operation recursively as many times as there were objects (or series of galaxies in a redshift range) in the subsample. At the end, we could compare the parameters from the several composite templates built from N_{obj}–$N_{removed\text{-}obj}$ and we checked whether they were consistent.

From the analysis on individual objects (Fig. 3), we discovered that only when removing HZ10 at $z = 5.659$ did we get slightly different values for T_{dust} and β_{RJ}. However, it does not significantly bias the parameters defining the shape of the composite template. We decided to keep it in the sample because it contributes to the representativity of the studied galaxies. The dust parameters are very stable with average values at $T_{dust} \approx 54$ K and $\beta_{RJ} \approx 0.9$.

From the analysis on redshift ranges, we discovered that the redshift range $5.0 < z < 6.0$ brings the objects with the widest wavelength range to the IR composite SED. Without the ALMA-detected galaxies in the range $5.0 < z < 6.0$, there was a difference for T_{dust} and β_{RJ} (Table 3). But again, the results are in agreement within the uncertainties, even though an evolution within the uncertainties cannot be ruled out.

This second phase provided an IR composite template IRV1 shown as green points in Fig. 2.

– Phase 2.2: Checking if the stacked data from Bethermin et al. (2020) are in agreement with the IRV1 → IRV2 template: In addition to the main ALPINE data, Bethermin et al. (2020) stacked data from two galaxy samples at $z \sim 4.5$ and $z \sim 5.5$ with *Herschel* (Pilbratt et al. 2010) data from the PEP (Lutz et al. 2011) and HerMES (Oliver et al. 2012) surveys and AzTEC/ASTE data from Aretxaga et al. (2011) at 1.1 mm. At 850 µm, they used the SCUBA2 data from

Casey et al. (2013). This data set can be very useful because it extends the wavelength range to the mid-IR. However, because there are not enough ALPINE sources to obtain a sufficiently high S/N in the stacked *Herschel* data, the ALPINE selection was not used for the stacking. Bethermin et al. (2020) define two redshift bins ($4 < z < 5$ and $5 < z < 6$) that match the redshift ranges probed by ALPINE. Before further continuing to fulfill our task of building the LBG composite IR template, we first need to assess whether the $z \sim 4.5$ and/or $z \sim 5.5$ stacks are consistent with the IRV1 composite IR template.

Our analysis allows us to conclude that both stacks are consistent (all χ^2_ν from the SED fitting have $\sim 0.3 - 0.4$) with the ALMA-detected galaxies' composite IR template built by combining the full sample of the 27 ALMA-detected objects. The final IR composite template (IRV2, Fig. 2) was built from the ALMA-detected galaxies from Burgarella et al. (2020), the ALPINE sample, in addition to the two stacks from Bethermin et al. (2020).

In Table C.1, we provide the IR composite template based on the observed data and show the fits with the three dust emissions from 1 µm to 1000 µm fitted in Fig. 4. The modeled SEDs from 20 µm to 1 mm are listed in Table D.1.

3.1.4. Fitting the IR composite template

The main dust parameters derived from fitting the observed IRV2 IR composite template (Fig. 4) are listed in Table 4. The objects in the present sample are Hiz-SFGs with a low dust attenuation (e.g., Faisst et al. 2020a, and later in this paper). This assumption is valid for the ALPINE sample (Faisst et al. 2020a). Therefore, we assume that the best emission models for these objects should be optically thin. We checked this hypothesis by estimating the following (Eq. (2) in Jones et al. 2020):

$$\tau_\nu = \frac{M_{\rm dust}}{A_{\rm gal}} \kappa_\nu$$

where τ_ν is the optical depth, $M_{\rm dust}$ is the dust mass, $A_{\rm gal}$ is the area covered by the galaxy, and κ_ν is the dust mass absorption coefficient:

$$\kappa_\nu = \kappa_0 \, (\nu / \nu_0)^{\beta_{\rm RJ}}$$

where ν_0 is the frequency where the optical depth equals unity and $\beta_{\rm RJ}$ is the spectral emissivity index from the Rayleigh-Jeans range. We tested the opacity both with the optically thin and with the general modified black bodies (Casey 2012). The median radius of the galaxies are $r_{e,[\rm CII]} = 2.1 \pm 0.16$ kpc (Fujimoto et al. 2020) to estimate $A_{\rm gal}$. Both provide values that are in the range $[10^{-4}$–$10^{-2}]$, that is $\tau_\nu \ll 1.0$, which confirms that the optically thin assumption is valid here. In the rest of the paper, we only make use of DL2014 and PL+OT_MBB dust emissions.

After fitting the IR composite template, we derived values for $T_{\rm dust}$ and $\beta_{\rm RJ}$ (Table 4). However, these dust parameters are known to be degenerate depending on the S/N and the wavelength sampling of the far-IR SED (e.g., Juvela et al. 2013; Tabatabaei et al. 2014). This degeneracy is a serious problem when using only one or a few data points in the far-IR. However, using the derived IR composite template helps to remove the degeneracy. We tested how well $T_{\rm dust}$ and $\beta_{\rm RJ}$ can be estimated by performing fits with fixed $T_{\rm dust}$ and varying $\beta_{\rm RJ}$, then by fixing $\beta_{\rm RJ}$ and keeping $T_{\rm dust}$ free. The results are compared to the parameters derived by keeping both parameters free in Fig. 5. Even though we can see the usual regular evolution of $T_{\rm dust}$ with $\beta_{\rm RJ}$ (or vice versa), the quality of the fit with fixed parameters improves when getting closer to the Bayesian values derived with CIGALE when both parameters are free (Table 4).

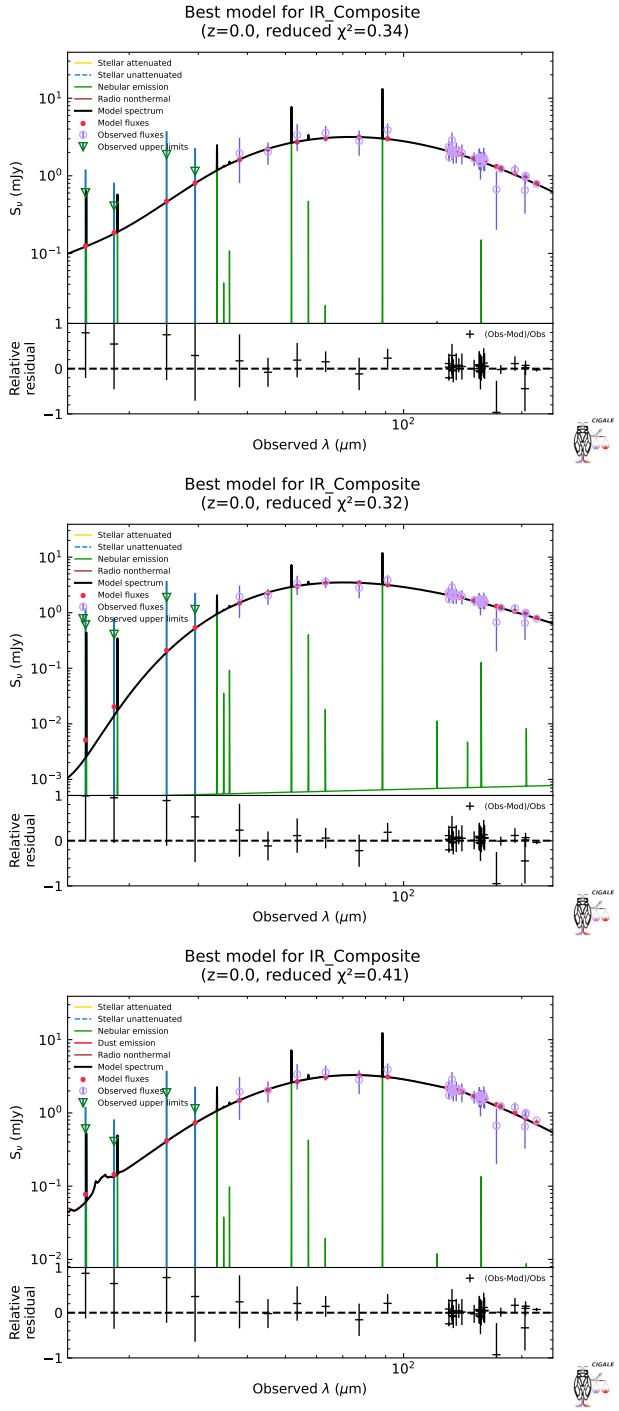

Fig. 4. Comparison of the various fits of the IR composite SED built with data from Burgarella et al. (2020), from ALPINE, and from the $z \sim 4.5$ and $z \sim 5.5$ stacks from Bethermin et al. (2020). *Top*: fit with a modified general blackbody and power law in the mid-IR as in Casey (2012). *Middle*: fit with an optically thin modified blackbody and power law in the mid-IR as in Casey (2012). *Bottom*: Fit with a model from Draine et al. (2014). The fits are all statistically equivalently good with reduced $\chi^2 \approx 0.3$–0.4.

The value of $\beta_{\rm RJ} = 0.87 \pm 0.28$ for a power law plus optically thin modified blackbody found in this paper is low, but comparable to the minimum values found by Bendo et al. (2003), Galametz et al. (2012), for example, for nearby galaxies

Table 4. Main relevant physical parameters derived by fitting the IR template with the various assumptions of the dust emission.

	PL+G_MBB	PL+OT_MBB	DL2014
$\alpha_{\rm MIR}$	2.23 ± 0.63	2.00 ± 0.82	N/A
$\beta_{\rm RJ}$	1.43 ± 0.47	0.87 ± 0.28	N/A
$T_{\rm dust}$[K]	65.5 ± 5.1	54.1 ± 6.7	N/A
$q_{\rm PAH}$	N/A	N/A	0.47
α	N/A	N/A	2.39 ± 0.44
$u_{\rm min}$	N/A	N/A	18.1 ± 12.7
γ	N/A	N/A	0.54 ± 0.35
$L_{\rm dust}/10^{20}$ [W]	2.84 ± 0.14	2.43 ± 0.12	2.57 ± 0.13

Notes. PL+G_MBB is based on a power law in the mid-IR plus the general blackbody formula as in Casey (2012); PL+OT_MBB is a power law in the mid-IR ($\alpha_{\rm MIR}$) plus an optically thin blackbody, which is again similar to Casey (2012); and DL2014 stands for Draine et al. (2014) models. The parameters are described in Appendix A. Because the SEDs were normalized to 1.0 at $\lambda = 200\,\mu$m, the values of $L_{\rm dust}$ can be directly compared.

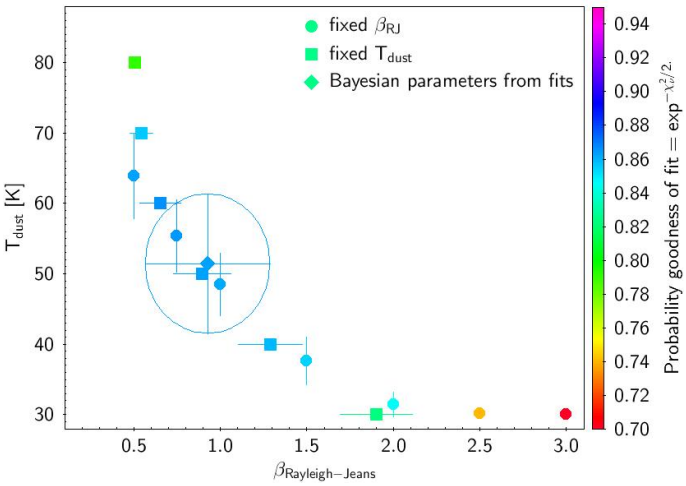

Fig. 5. Results of the tests on the determination of $T_{\rm dust}$ and $\beta_{\rm RJ}$ and their possible degeneracy are shown here. Dots show the evolution of $T_{\rm dust}$ when $\beta_{\rm RJ}$ was fixed during the fits. Boxes show the evolution of $\beta_{\rm RJ}$ when $T_{\rm dust}$ was fixed during the fits. Finally, the diamond symbol shows the result and uncertainties on both axes when $T_{\rm dust}$ and $\beta_{\rm RJ}$ are both free. The color coding indicates the level of the goodness of fit.

in the range $0.8 < \beta_{\rm RJ} < 2.5$. Lower $\beta_{\rm RJ}$ closer to 1.0 were estimated when fitting different types of galaxies and more specifically very low-metallicity galaxies such as SBS 0335-052 (Hunt et al. 2014), NGC 1705 (O'Halloran et al. 2010), and even low-metallicity regions in very nearby galaxies with excellent coverage to estimate $\beta_{\rm RJ}$ similar to Messier 33, for instance (Tibbs et al. 2018; Tabatabaei et al. 2014). Tabatabaei et al. (2014) found an apparent decrease in both $T_{\rm dust}$ and $\beta_{\rm RJ}$ with an increasing M33 radius. This corresponds to regions with low metallicities and they propose that the effect could help to find an origin in the different grain compositions and, possibly, different size distributions. Assuming such $\beta_{\rm RJ}$ values for Hiz-SFGs would mean that the mean dust temperature could be higher than $T_{\rm dust}$ estimated with emissivities in the range $1.5 < \beta_{\rm RJ} < 2.0$. This result ($\beta_{\rm RJ} \sim 1$) needs to be further confirmed for the SEDs of similar low-$M_{\rm star}$, low-$A_{\rm FUV}$ galaxies with a better RJ wavelength coverage.

The value of $T_{\rm dust}$ found from the IR composite template (54.1 ± 6.7 K) should be compared to other ALMA-based dust temperatures for objects at high redshift ($z > 4.5$). In a recent paper, Bakx et al. (2021) present the evolution of $T_{\rm dust}$ for "normal" (i.e., main sequence) galaxies from $z \sim 0$ to $z \sim 8$. A linear increase is suggested up to $z = 6$. At larger redshifts, a large dispersion in $T_{\rm dust}$ can be noticed even though the linear relation might hold, given the large uncertainties (Faisst et al. 2020b; Harikane et al. 2020; Sugahara et al. 2021; Laporte et al. 2019). Bakx et al. (2021) show that adding ALMA Band 9 significantly reduces the uncertainty on the dust temperature for a single object by further constraining the shape of the SED. At the mean redshift $z = 4.94 \pm 0.54$ of our entire sample, the dust temperature that could be estimated assuming the linear relation from Fig. 4 in Bakx et al. (2021) would be $T_{\rm dust} \approx 49$ K, which is not significantly different from our estimation of 54.1 ± 6.7 K. However, Bakx et al. (2021) derived a value of $\beta_{\rm RJ} = 1.61 \pm 0.60$ which is larger than the one found in the previous paragraph. Both are consistent if we account for the uncertainties. Lower values for $\beta_{\rm RJ}$ mean higher dust temperatures, as shown in Fig. 5. Thus measuring $\beta_{\rm RJ}$ with a good sampling of the RJ part of the spectrum is important to address the question about the decrease in $\beta_{\rm RJ}$ in low-metallicity regions toward the outskirts of local galaxies and in some local low-metallicity galaxies. If so, the increase in dust temperature might be larger than when evaluated with $\beta_{\rm RJ} \sim 1.5$–2.0.

3.2. Phase 3: Far-UV to far-IR fit of individual galaxies with the IR composite template

We now fit the complete sample of objects assuming the dust emission from the IRV2 composite SED. The rest-frame UV, optical, and near IR ranges are useful when constraining the stellar emission and, therefore, the properties of the stellar populations. However, attenuation also impacts the rest-frame UV spectral range, which is therefore useful to constrain the amount of dust attenuation. The assumptions used when fitting the entire galaxy sample with CIGALE are given in Table B.1. We focus on the properties of the stellar populations and the dust attenuation in these objects.

Even though the Bayes factor is conceptually more conclusive, its computation can still be very complex. We need to compute a quantity called the marginal likelihood or evidence ($P(D/M_i)$), where D are the photometric data and M_i are each model, which implies computing a very complicated and time-consuming integral because the likelihood of observation D under the model M_i must quantify over all possible parameters of that model. An analytic computation is almost never possible and direct evaluation by numerical quadrature is almost never feasible for models of real-world dimensionality and complexity. This is why a variety of approximations based on special properties of the models or their posterior distributions were developed (Kass & Raftery 1995).

Generally, it is found that the conclusions drawn from the Bayes factor are more satisfying, but also more complex methodologies have not been qualitatively very different from those drawn from the simpler BIC method (Raftery 1998). However, we can elaborate on the use of the BIC versus Bayes Factor for our specific case. From Raftery (1998), we determined that in our case, the unit information prior should reasonably cover the range of observed data because we have a homogeneous sample of galaxies and we have a rough idea of the general range within which the data are likely to lie in advance. So we defined our priors to homogeneously cover the expected range of parameters.

Table 5. Comparison of the reference model (SFH delayed: $t/\tau^2 \exp(-t/\tau)$ with $\tau = 500$ Myr) to all the others using the BIC.

DL2014 vs. PL+OT_MBB									
τ_{main}[Myr]	k	Age$_{main}$[Myr]	τ_{burst}[Myr]	Age$_{burst}$[Myr]	δ	Mean	SD	Min	Max
500 Myr	$2 \leq k \leq 5$	101 values in [2, 1200]				−0.95	1.58	−7.28	4.08
DL2014									
τ_{main}[Myr]	k	Age$_{main}$[Myr]	τ_{burst}[Myr]	Age$_{burst}$[Myr]	δ	Mean			
20 000 Myr	$2 \leq k \leq 5$	101 values in [2, 1200]				−3.35	11.21	−68.37	1.39
10 values in [100, 1000]	$3 \leq k \leq 6$	101 values in [2, 1200]				−0.75	5.83	−3.15	41.64
500	$3 \leq k \leq 6$	101 values in [100, 1200]	20 000	2, 5, 10, 20, 50		−1.62	5.87	−9.23	16.89
500	$3 \leq k \leq 6$	101 values in [2, 1200]			7 values in [−0.70, 0.70]	1.49	7.12	−3.59	43.43
PL+OT_MBB									
20 000 Myr	$2 \leq k \leq 5$	101 values in [2, 1200]				−3.49	11.40	−68.37	1.55
10 values in [100, 1000]	$3 \leq k \leq 6$	101 values in [2, 1200]				−0.67	6.00	−3.15	41.64
500	$3 \leq k \leq 6$	101 values in [100, 1200]	20 000	2, 5, 10, 20, 50		−1.05	6.57	−9.23	19.16
500	$3 \leq k \leq 6$	101 values in [2, 1200]			7 values in [−0.70, 0.70]	1.51	7.20	−3.04	42.94

Notes. This comparison was performed by fitting all the objects in our sample. We note that the IR composite SED is not used in this analysis, but only individual ALMA measurements (detections and upper limits). We first assumed a DL2014 model for the IR template. The, we assumed a PL+OT_MBB for the IR template. The BIC values do not change much for the two options for the IR template. The range in the number of parameters k is also indicated for each series of run. To the parameters listed in the table, we need to add the amount of dust attenuation, i.e., E_BVs_young. The sample has at least five photometric points in the rest-frame UV and optical as well as one photometric point in the rest-frame far-IR, so $n \geq 7$. More precisely, the complete sample of individual galaxies have $7 \leq n \leq 24$ with $\langle n \rangle = 13.3 \pm 4.3$ and 11/119 objects have more than ten photometric points.

Volinsky (1997) showed, via simulations, that the performance of Bayes factors can be better than that of BIC if the prior used is spread out less than the unit information prior. In our case, the unit information prior is quite spread out (see Table 5) and BIC should be at least as good as the Bayes factor. Because of this spread out prior, BIC provides more conservative results. Also, if an effect is favored by BIC, this should be a solid result. On the other hand, if BIC does not favor an effect, it might still be possible that another, justifiable prior could change the conclusion. For us, that means that the most conclusive results would be that an SFH that includes a burst is solidly ruled out when compared to a delayed SFH with $\tau = 500$ Myr SFH.

We decided to use the Bayesian information criterion (BIC) test to compare the various hypotheses made on the dust emission and on the star formation history in Fig. 6. To interpret the results from the BIC tests, we refer to Kass & Raftery (1995):

$$\mathrm{BIC} = \chi^2 + k \ln(n)$$

where k is the number of model parameters in the test and n is the sample size, that is to say the number of pieces of photometric data in our case. When comparing several models, the one with the lowest BIC is preferred. To interpret the results, $0 < \Delta\mathrm{BIC} < 2$ means that evidence for a difference between the two hypotheses is faint ($2 < \Delta\mathrm{BIC} < 6$ means positive, $6 < \Delta\mathrm{BIC} < 10$ means strong, and $\Delta\mathrm{BIC} > 10$ means very strong).

We start by comparing the two dust emission models, DL2014 (Draine et al. 2014) and PL+OT_MBB (Casey 2012), available in CIGALE. Table 5 presents all the results of the BIC analysis on our sample of Hiz-SFGs, numerically. The histogram of ΔBIC values strongly peaks at 0 with a small tail extending to $\Delta\mathrm{BIC} = -4$ (Fig. 6), meaning that we do not see any strong difference between DL2014 and PL+OT_MBB when fitting our sample. However, for a minority of objects, PL+OT_MBB might be favored. We show the results using both DL2014 and PL+OT_MBB later in the paper. However, in general, no significant difference as to the quality of the fit is observed, confirming the BIC analysis.

We now focus on the comparison between the various SFHs. Figure 6 shows the results of the BIC analysis by comparing the various kinds of SFHs used in the CIGALE analysis. We note that we only used the initial observed data and not the IR composite template. The only significant difference is that a simple delayed SFH with $\tau_{main} = 500$ Myr without any final burst is preferred to a delayed SFH with a burst. A constant SFH (with $\tau_{main} = 20$ Gyrs) and multi-τ_{main} are weakly disfavored when compared to a simple delayed SFH with $\tau_{main} = 500$ Myrs. These comparisons are compatible with both DL2014 and PL+OT_MBB. There is some dispersion in the results which suggests that the preferred modeling for the entire galaxy population might not be valid for each individual galaxy, as shown in Fig. 6.

In order to move a little bit further with our comparison of the models, we performed a mock analysis with CIGALE from the initial fit, again without using the IR composite template. We selected the PL+OT_MBB and DL2014 options for the dust emission in Fig. C.1. In brief, for each object, the CIGALE mock analysis consists in using the best fit model for each object to generate an input photometric catalog (called a mock catalog) to which we randomly added uncertainties drawn inside a Gaussian distribution with σ corresponding to the observed uncertainties (see Boquien et al. 2019). The SED fitting procedure was applied in the very same way as when fitting the observed SEDs. Then, we compared the derived output parameters to those of the known input (Fig. C.1). The results from this mock analysis (Table 6) show that both for the PL+OT_MBB and for the DL2014 dust emissions, we were able to recover the main physical parameters related to the SFH and to the dust emission. This means that we do not expect strong degeneracies ($r^2 = 0.80$ shown in Fig. C.1, where r is Pearson's correlation coefficient commonly used in linear regression). The mean value and standard dispersion of the main parameters derived from the individual fits of our galaxy sample are given in Table 7 and the individual values for the same parameters are listed in Tables E.1 and E.2 (available at the CDS) in their entirety.

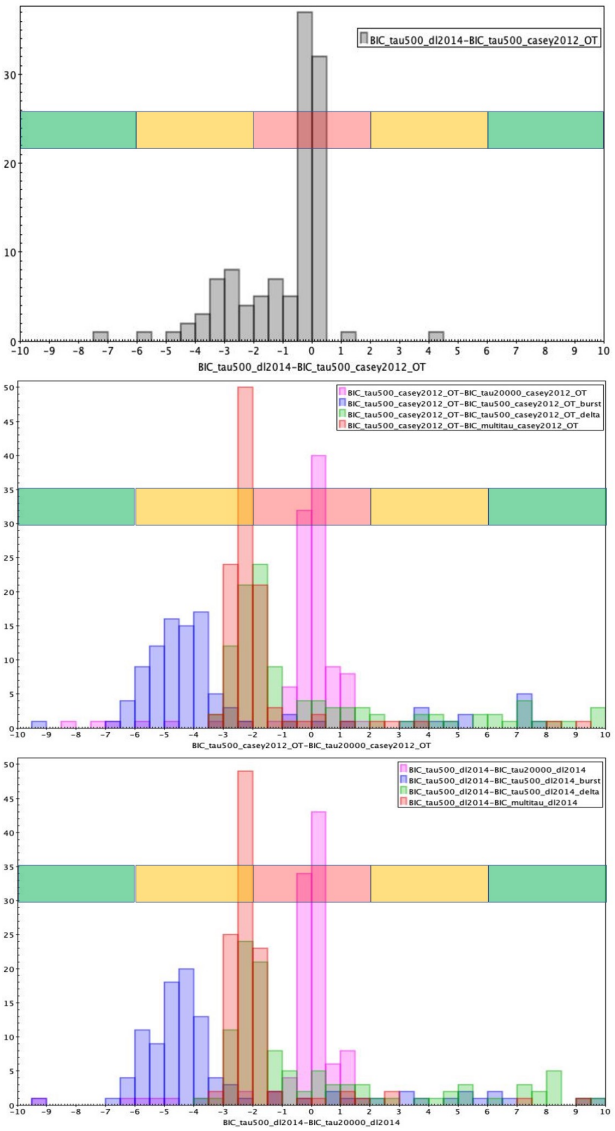

Fig. 6. Result of the ΔBIC test on our sample of Hiz-SFGs. A delayed SFH without a burst and $\tau_{main} = 500$ Myr is labeled as "tau500". With an additional burst at the end of the SFH, it is labeled as "burst". A constant SFH without a burst and $\tau_{main} = 20$ Gyrs is labeled as "tau20000". And when several τ_{main} could be selected in the SED fitting, it is labeled as "multitau" in the legend. *Top*: ΔBIC test that compares the influence of the DL2014 model and the PL+OT_MBB dust emissions in building the IR template. *Center*: ΔBIC test on the SFH assuming the PL+OT_MBB for the IR template. *Bottom*: ΔBIC test on the SFH assuming the DL2014 model for the IR template. The color band allows one to interpret the results of the evidence (ΔBIC) against the model with the higher BIC: red means "faint evidence", orange means "positive evidence", and green mean "strong evidence". We do not see any strong evidence that DL2014 or PL+OT_MBB are better for fitting the data. An SFH that includes a burst is positively ruled out, while a delayed SFH with $\tau = 500$ Myr is weekly favored.

4. Analysis of the results

From the previous analysis, we derived a set of physical parameters for each of the galaxies in our sample. These parameters allowed us to define and build diagnostic diagrams that permitted us to characterize these galaxies and, more specifically, their SFH and their dust properties. We analyzed the locations of our sample in the IRX versus β_{UV} diagram, the A_{FUV} versus M_{star} diagram, and in the specific dust mass versus specific star formation rate: sM_{dust} versus $sSFR = M_{dust}/M_{star}$ versus SFR/M_{star} (dust formation rate diagram or DFRD).

4.1. The SFR versus M_{star} diagram

Figure 7 presents the SFR versus M_{star} diagram[3]. The points corresponding to this work are found in the expected range when compared to Pearson et al. (2018) who also used CIGALE:

$$\log_{10}(SFR) = (1.00 \pm 0.22)\,(\log_{10}(M_{star}) - 10.6) + (1.92 \pm 0.21)$$

and compared to Speagle et al. (2014) with their "mixed" (preferred fit)":

$$\log_{10}(SFR) = [(0.73 \pm 0.02) - (0.027 \pm 0.006) \times t[\mathrm{Gyr}]]\log_{10}(M_{star}) - [(5.42 \pm 0.22) + (0.42 \pm 0.07) \times t[\mathrm{Gyr}]]$$

function evaluated at $z = 5.0$ (i.e., $t_{universe} = 1.186$ Gyr), which was converted to a Chabrier IMF by subtracting 0.03 to $\log_{10}(SFR)$ and to $\log_{10}(M_{star})$. The first result is that regardless of the dust emission used (DL2014 or PL+OT_MBB), we found about the same main sequence. Our data are in good agreement with Faisst et al. (2020a) and Khusanova et al. (2021) and also they generally follow the relations derived by Speagle et al. (2014) and Pearson et al. (2018). Most of the detections are found at a relatively large stellar mass ($\log_{10}(M_{star}) \sim 10$). We confirm the evolution of the main sequence to $z = 4.5 - 5.5$ with our sample of galaxies (mainly objects not detected in dust continuum), which extend to $\log_{10}(M_{star}) \sim 8.5$.

4.2. The A_{FUV} versus M_{star} diagram

The relation between the dust attenuation (A_{FUV} or its proxy, $IRX = L_{dust}/L_{FUV}$) and the stellar mass (M_{star}) is another way to estimate the dust attenuation in galaxies without far-IR data. This relation between the stellar mass and dust attenuation has been the focus of numerous studies (as early as Xu et al. 2007; Buat et al. 2009, and references therein). However, even if this relation could be very useful in addition to the IRX versus β_{FUV} one ($f_\lambda \propto \lambda^{\beta_{FUV}}$), the link between the far-UV (FUV) dust attenuation and the stellar mass (A_{FUV} versus M_{star}) is not well established at all redshifts.

Bouwens et al. (2016) define what a consensus relation could be: $\log_{10}(IRX) = \log_{10}(M_{star}/M_\odot) - 9.17$ assuming the dust temperature evolves with the redshift. This relation is linear in the plane $\log_{10}(IRX)$ versus $\log_{10}(M_{star}/M_\odot)$, and in the range $9.0 < \log_{10}(M_{star}/M_\odot) < 11.0$. In a recent paper, Carvajal et al. (2020) used the stacking method for 1582 UV LBGs with photometric redshifts in the range $z \sim 2$–8 to reach down to $\log_{10}(M_{star}/M_\odot) = 6.0$. However, the constraints from this stacking are only upper limits, which are less useful than detections (see their Fig. 16). Fudamoto et al. (2020) made use of the ALPINE data and show that the $\log_{10}(IRX)$ versus M_{star} relation derived from their observations is inconsistent with the previously determined relations at $z \leq 4$. They found a fast decrease in IRX at $z \sim 4$ in massive galaxies which suggests an evolution of the average amount of dust attenuation in star forming galaxies. Bernhard et al. (2014) assume an evolving normalization of the $\log_{10}(IRX)$ versus $\log_{10}(M_{star})$ relation in the

[3] We only present the results using the reference SFH derived in the present section, i.e., delayed $SFR(t) = t/\tau^2_{main}\ \exp(t/\tau)$ with $\tau_{main} = 500$ Myr, but with the following two options for dust emission: Draine et al. (2014) and a power law in a mid-IR and optically thin blackbody.

Table 6. Summary of the power of two for correlation coefficients, r^2, from the mock analysis on the main physical parameters performed by CIGALE.

Run	$L_{\rm dust}$	$L_{\rm FUV}$	IRX	$M_{\rm dust}$	$\beta_{\rm calz94}$	$\rm SFR_{10\,Myr}$	$f_{\rm burst}$	$\rm age_{burst}$	$\tau_{\rm main}$	$\rm age_{main}$	δ	$M_{\rm star}$	$A_{\rm FUV}$
$\tau_{\rm 500\,Myr}$_dl2014	0.98	0.89	0.91	0.98	0.89	0.96				0.81		0.95	0.92
$\tau_{\rm 500\,Myr}$_casey2012_OT	0.98	0.84	0.87	0.98	0.84	0.96				0.80		0.93	0.85
$\tau_{\rm 20000\,Myr}$_dl2014	0.97	0.92	0.89	0.97	0.87	0.95				0.71		0.94	0.89
$\tau_{\rm 20000\,Myr}$_casey2012_OT	0.98	0.90	0.89	0.98	0.87	0.97				0.74		0.95	0.89
$\tau_{\rm 500\,Myr}$_dl2014_burst	0.96	0.90	0.88	0.96	0.91	0.93	0.47	0.05		0.46		0.96	0.93
$\tau_{\rm 500\,Myr}$_casey2012_OT_burst	0.96	0.94	0.90	0.96	0.89	0.91	0.27	0.06		0.42		0.94	0.92
$\tau_{\rm multi}$_dl2014	0.98	0.56	0.87	0.98	0.73	0.96			0.20	0.65		0.13	0.90
$\tau_{\rm multi}$_casey2012_OT	0.98	0.64	0.88	0.98	0.80	0.97			0.18	0.62		0.19	0.91
$\tau_{\rm 500\,Myr}$_dl2014_delta	0.99	0.93	0.90	0.99	0.85	0.97				0.78	0.37	0.94	0.89
$\tau_{\rm 500\,Myr}$_casey2012_OT_delta	0.98	0.92	0.79	0.98	0.56	0.97				0.79	0.35	0.92	0.62

Notes. The delayed SFH with $\tau_{\rm main} = 500$ Myr is shown with "tau500" in the legend. If a final burst was added, "burst" is used in the legend. A constant SFH with $\tau_{\rm main} = 20$ Gyr is shown with "tau20000" in the legend, and multi-$\tau_{\rm main}$ is shown as "multitau" in the legend.

Table 7. Mean value and standard deviations of the physical parameters derived from the fit analysis of the individual objects in our sample.

Parameter	DL2014	PL+OT_MBB
$M_{\rm star}$ $[M_\odot]$	$(1.18 \pm 0.19) \times 10^{10}$	$(1.18 \pm 0.18) \times 10^{10}$
SFR $[M_\odot\ {\rm yr}^{-1}]$	47.6 ± 5.1	46.8 ± 5.0
$M_{\rm dust}$ $[M_\odot]^{(*)}$	$(5.64 \pm 0.69) \times 10^7$	$(2.07 \pm 0.25) \times 10^7$
$L_{\rm dust}$ $[L_\odot]$	$(3.38 \pm 0.41) \times 10^{11}$	$(3.32 \pm 0.40) \times 10^{11}$
$L_{\rm FUV}$ $[L_\odot]$	$(1.07 \pm 0.06) \times 10^{11}$	$(1.06 \pm 0.06) \times 10^{11}$
sSFR $[{\rm yr}^{-1}]$	$(1.16 \pm 0.34) \times 10^{-8}$	$(1.15 \pm 0.34) \times 10^{-8}$
$sM_{\rm dust}$ $^{(*)}$	0.010 ± 0.003	0.004 ± 0.001
IRX	0.31 ± 0.14	0.31 ± 0.13
$A_{\rm FUV}$	1.14 ± 0.15	1.14 ± 0.15
$\rm Age_{main}$ [Myr]	440 ± 98	444 ± 98

Notes. The Bayesian outputs are listed here. $^{(*)}$The values listed in the table are those computed with $\kappa_0 = 0.637\,{\rm m^2\,kg^{-1}}$, corresponding to Draine et al. (2014). For $\kappa_0 = 0.45\,{\rm m^2 kg^{-1}}$ [$\kappa_0 = 0.72\,{\rm m^2\,kg^{-1}}$, respectively], that is before [after, respectively] the reverse shock, we found the following: $M_{\rm dust} = (2.91 \pm 0.35) \times 10^7\ M_\odot$ [$M_{\rm dust} = (1.82 \pm 0.22) \times 10^7\ M_\odot$, respectively] and $sM_{\rm dust} = 0.005 \pm 0.002$ [$sM_{\rm dust} = 0.003 \pm 0.001$, respectively].

low redshift universe at $z < 1$. We need an opposite evolution (lower in IRX) in the high redshift universe at $z > 4$ as in Bogdanoska & Burgarella (2020).

Figure 8 shows that the two $M_{\rm star}$ stacks from Fudamoto et al. (2020) at $z \sim 4.5$ are marginally (accounting for the uncertainties) in agreement with Bogdanoska & Burgarella (2020). They are in better agreement at $z \sim 5.5$. However, the low stellar mass range is crucial, especially in the early universe where galaxies are expected to have lower stellar masses because they were still building their stars at that time. From our analysis, we confirm the effect found by Fudamoto et al. (2020): our galaxies have lower $A_{\rm FUV}$ or IRX values at a fixed mass, compared to previously studied IRX–$M_{\rm star}$ relations at $z < 4$, with quite a large scatter.

In order to constrain the amount of dust attenuation of these low-mass galaxies, it is possible to adopt a global approach and compare what the hypothesis on the $A_{\rm FUV}$ versus $\log_{10}(M_{\rm star})$ implies for the redshift evolution of the average dust attenuation in the universe as presented in Cucciati et al. (2012), Burgarella et al. (2013), Madau & Dickinson (2014), for example. Using this approach, Bogdanoska & Burgarella (2020) conclude that it is not possible to extend a linear relation to the lowest mass range without strongly underpredicting the average dust attenuation in the universe at all redshifts. We need a flattening of the relation at low stellar mass ($\log_{10}(M_{\rm star}/M_\odot) < 9.0$). This means that the apparent dust attenuation of the low-mass galaxies is significantly higher than 0. This very interesting and unexplained point is also suggested by other observational and theoretical works (e.g., Salim et al. 2016; Takeuchi et al. 2010; Cousin et al. 2019; Ma et al. 2016). They propose modeling the $A_{\rm FUV}$ versus $M_{\rm star}$ relation with the following broken law:

$$A_{\rm FUV} = \begin{cases} a \times 1.1 & \text{at } \log_{10} M_{\rm star} < 9.8 \\ a \times (\log_{10} M_{\rm star} - 8.7) & \text{at } \log_{10} M_{\rm star} \geq 9.8 \end{cases} \quad (1)$$

where $a = (z + \gamma) \times \alpha^{\beta-(z+\gamma)}$ with z being the redshift and the constants $\alpha = 1.84 \pm 0.11$, $\beta = 1.84 \pm 0.12$, and $\gamma = 0.14 \pm 0.04$. Although there is some dispersion and the completeness is very likely small at $\log_{10} M_{\rm star} < 10.0$, Fig. 8 suggests that the relation from Bogdanoska & Burgarella (2020) at $z = 5.0$ is in broad agreement with the data. However, the large number of upper limits at low mass could suggest that the level of the flat relation might be overestimated with respect to the present data. Alternate ways to measure $A_{\rm FUV}$ for low-mass galaxies should be explored, maybe via the Balmer decrements with JWST or with radio data using the radio-to-IR ratio $q_{\rm IR}$ that allows one to constrain the far-IR emission of star-forming galaxies from radio data (e.g., Helou et al. 1985; Delvecchio et al. 2021).

4.3. The IRX – $\beta_{\rm FUV}$ diagram

To estimate the UV slope $\beta_{\rm FUV}$, we used the definition given by Calzetti et al. (1994) in the range 125–260 nm within ten selected windows (see their Table 2) designed to remove all absorption features and the 217.5 nm dust bump ($\beta_{\rm Calzetti-1994}$) from the fitting procedure. The IRX – $\beta_{\rm FUV}$ is a classical tool to estimate the dust attenuation of galaxies. Figure 9 shows the location of the galaxies in the IRX versus $\beta_{\rm FUV}$ diagram. We also show the classical positions assuming a Calzetti law and a small Magellanic cloud (SMC) law. Our galaxies appear to be systematically shifted to the left of the diagram, that is to bluer values of $\beta_{\rm FUV}$ compared to the locus estimated by Overzier et al. (2010) for galaxies at $z = 0$. This might be related to the evolution of the stellar population at $z \sim 4.5 - 5.0$ as they were younger and bluer (and/or an intrinsic evolution of other parameters similar to the IMF). Age effects were already found at low redshift (e.g., Kong et al. 2004; Boquien et al. 2009).

The IllustrisTNG Project (TNG hereafter: Nelson et al. 2018; Pillepich et al. 2018) is a suite of cosmological simulations for the formation of galaxies. TNG50 does not model dust directly, but Schulz et al. (2020) assume that the diffuse dust content of a galaxy is traced by the gas-phase metal distribution

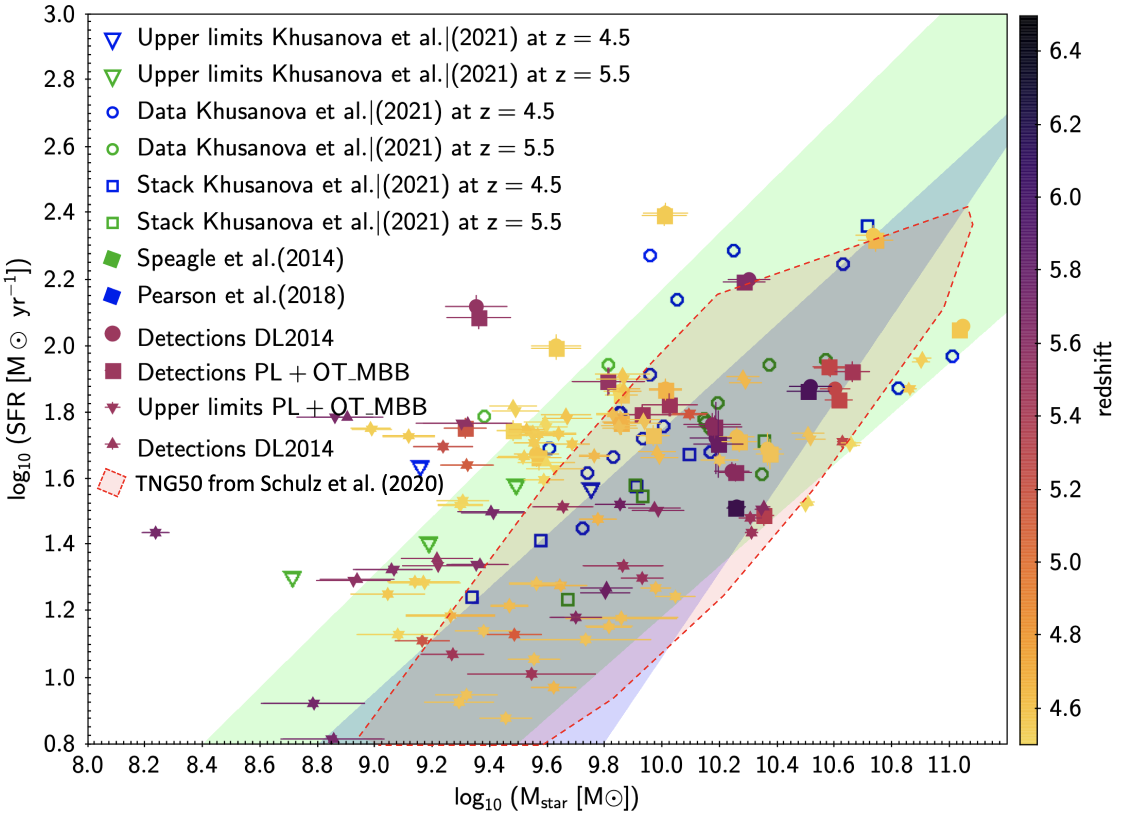

Fig. 7. In the $\log_{10}$ (SFR) vs. $\log_{10}$ ($M_{\rm star}$) diagram, the main part of the sample is found within the limits for the fits of the main sequence at $z = 5.0$ by Speagle et al. (2014; green shading), by Pearson et al. (2018) at $z \sim 5.2$ (purple shading), and by Faisst et al. (2020a), who found that the galaxies are in agreement with Speagle et al. (2014). Is is important to note, however, that some of our objects are at redshifts larger than the 4.5–5.6 ALPINE sample (see color code of the markers). For Speagle et al. (2014), we used the "mixed" (preferred fit)" function (as defined by Speagle et al. 2014). The results from the two fits with DL2014 and PL+OT_MBB are presented. The two types of dust emission do not significantly modify the location of the points in the diagram. Detections are shown as dots and boxes and upper limits are shown as downward- and upward-pointing triangles. The uncertainty range for upper limits extends to the bottom of the plot. In addition to having mainly upper limits, at $\log_{10}$ ($M_{\rm star}$) < 9.5, the sample is very likely incomplete which means that it is difficult to estimate a trend from these data over the entire mass range. We also added the objects and stacks from Khusanova et al. (2021) with open markers. Finally, the selection of TNG50 galaxies used in Schulz et al. (2020) is also provided (red-shaded area).

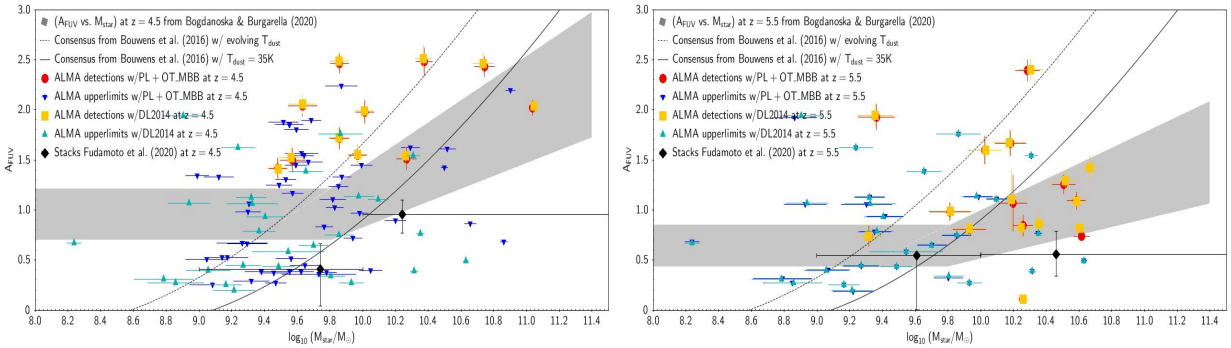

Fig. 8. $A_{\rm FUV} - M_{\rm star}$ diagram at $z \sim 4.5$ (*left*) and $z \sim 5.5$ (*right*). The gray areas correspond to the expected relation at $z = 4.5$ and 5.5 from Bogdanoska & Burgarella (2020). This relation was formed by a broken line, which is flat at $\log_{10} M_{\rm star} \leq 9.8$ and rises at $\log_{10}$ ($M_{\rm star}$) > 9.8. The ALPINE data are very dispersed at $z \sim 4.5$, while this flatness is supported by the data at $z \sim 5.5$. The conversion from IRX to $A_{\rm FUV}$ is from Burgarella et al. (2005): $A_{\rm FUV} = -0.028[\log_{10}({\rm IRX})]^3 + 0.392\,[\log_{10}({\rm IRX})]^2 + 1.094\,[\log_{10}({\rm IRX})] + 0.5$.

assigned to this galaxy. The dust density distribution is derived from the TNG50 gas density distribution with assumptions on the dust-to-metal ratio, the gas metallicity, the gas temperature, and the instantaneous SFR. Finally, SKIRT (Baes et al. 2011) is used to model the emission of the galaxies. Their fiducial model is a multicomponent dust mix, which models a composition of graphite, silicate, and polycyclic aromatic hydrocarbon (PAH) grains, with various grain size bins for each grain type which reproduce the properties of Milky Way (MW), large Magellanic cloud (LMC), and SMC type dust. In SKIRT, the dust of the molecular birth clouds mentioned is treated separately from the diffuse ISM dust.

Schulz et al. (2020) used the output of the TNG50 simulation and suggest a redshift-dependent systematic shift toward lower

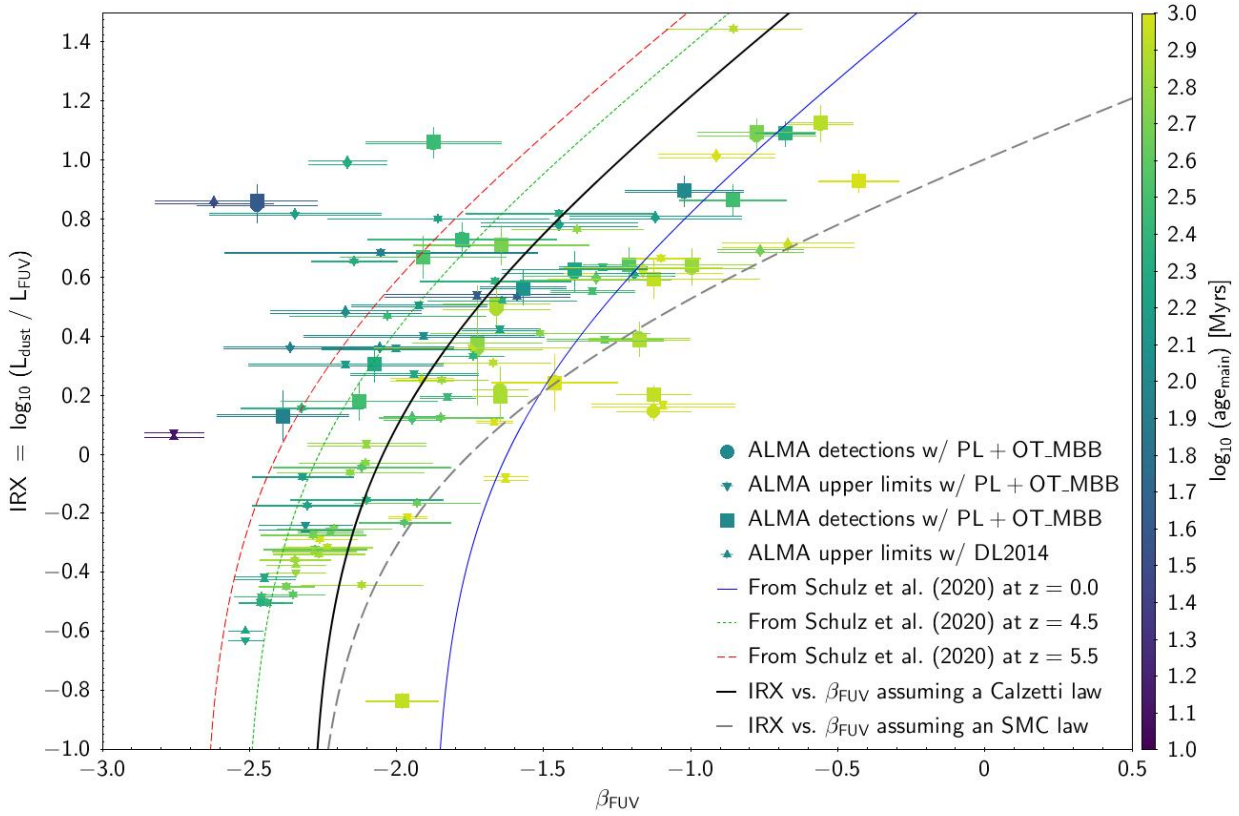

Fig. 9. IRX – $\beta_{\rm CFUV}$ diagram. IRX values were estimated with CIGALE and $\beta_{\rm FUV}$ were fitted on the data directly. They are not model-dependant. The black continuous line corresponds to the original Calzetti law, under the assumption that the underlying dust curve follows the Calzetti et al. (2000) attenuation. The dashed line to the predicted law assumes the SMC extinction law (e.g., Gordon et al. 2003). Both are from McLure et al. (2018). The color of the symbols are related to the axis to the right of the figure, the age of the stellar population. Both results with dust emission, DL2014 and PL+OT_MBB, are presented with different symbols with ALMA upper limits and ALMA detections. In the figures, we also plotted the laws from Schulz et al. (2020) at $z = 0.0$ (blue continuous line), 4.5 (green dotted line), and 5.5 (red dashed line). A comparison with the IRX – $\beta_{\rm FUV}$ plot in Fudamoto et al. (2020) with the same sample suggests that our (especially ALMA-detected) galaxies extend less to very blue $\beta_{\rm FUV}$. This is mainly true for the subsample of galaxies not detected in continuum with ALMA. This is probably due to two effects: first, in Fudamoto et al. (2020), 3σ upper limits are plotted. Another possible effect could be because we used a unique IR composite template in the SED fitting, which reduces the uncertainties on $L_{\rm dust}$.

$\beta_{\rm FUV}$ with increasing redshift modeled by adding a component $\beta_z(z) = 0.142z - 0.081$ to the $\beta_{\rm FUV}$ value at $z = 0$. The trend was calibrated up to $z = 4$. If we extrapolate their trend out to the redshift of our galaxies, the corresponding locus in Fig. 9 would appear too blue when compared to most of our galaxies. In order to extend the redshift range, we computed $\beta_z = \beta - \beta_{\rm Overzieret\ al.(2010)}$ because Overzier et al. (2010) is the reference at $z = 0$ used by Schulz et al. (2020).

An evolution in redshift of this effect is observationally confirmed. One of the main parameters that can be at the origin of the shift is likely to be the evolution of the stellar population, as mentioned above. So, even though using the redshift as the independent variable might be a simple solution, a more realistic and physical approach should be related to the stellar populations themselves. Schulz et al. (2020) present, in their Fig. 7 (middle), the variations of the intrinsic UV slopes β_0 of the galaxy stellar population (i.e., before the attenuation by dust) against their mass weighted mean stellar population ages. This figure shows that β_0 correlates with the stellar population age: the younger the stellar population, the lower β_0 is. From Fig. 7 (middle) from Schulz et al. (2020), we measured the mean and uncertainties over each axis of the intrinsic UV–slopes β_0 and of the mass-weighted mean stellar population ages (age_$M_{\rm star}$) for each redshift range. CIGALE provides mass-weighted mean stellar population ages for each of the galaxies and for our two best models defined above (i.e., delayed SFH with $\tau = 500$ Myr plus DL2014 and PL+OT_MBB for the IR emission). These values are plotted in Fig. 10. The average in the four bins of age_$M_{\rm star}$ from Schulz et al. (2020) and our data points seem to follow a linear relation. Although the points from Schulz et al. (2020) are not fully compatible with ours, there is a general trend. Statistical tests with the LINMIX library, which uses a hierarchical Bayesian approach for the linear regression with an error in both X and Y (Kelly 2007), suggest that the trend is highly significant (see correlation coefficient in Fig. 10), given the number of points used. The equations in Fig. 10 allow one to quantify this systematic shift along $\beta_{\rm FUV}$ at large redshift.

4.4. The dust formation rate diagram (DFRD)

Burgarella et al. (2020) and Nanni et al. (2020) built a diagram to follow the evolution of the dust mass called the dust formation rate diagram (DFRD) which shows the specific dust mass ($M_{\rm dust}/M_{\rm star}$ = sM$_{\rm dust}$) versus the specific star formation rate (SFR/$M_{\rm star}$ = sSFR). The specific dust mass was already identified by Calura et al. (2017) as a quantity that represents a true measure of how much dust per unit stellar mass survives the various destruction processes in galaxies. However, this is also a quantity that allows one to quantify the various dust formation processes. The interpretation of this DFRD is that galaxies

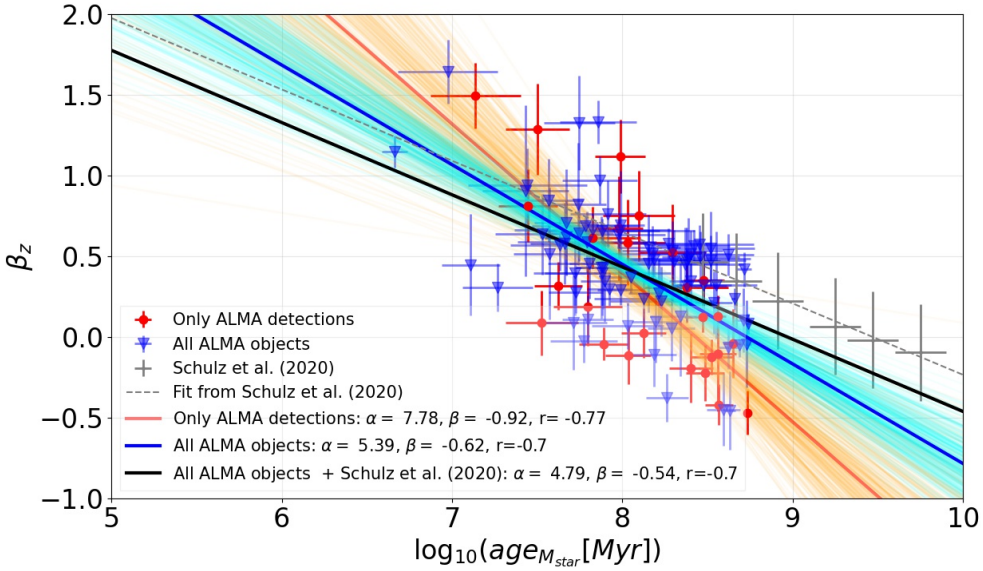

Fig. 10. Linear relation between the shift of the IRX-$\beta_{\rm FUV}$ relation at $z = 0$ (namely that of Overzier et al. 2010) vs. the mass-weighted age in years derived from the analysis of the galaxies studied here. Red symbols correspond to ALMA-detected objects, while blue objects correspond to upper limits from ALMA. We note, however, that these upper limits apply to ALMA, but not to the parameters presented in this figure: $\mathrm{age}_{M_{\rm star}}$ and β_z.

would follow a dust cycle where they start to build their dust grains at high sSFR leading to a fast rise in $sM_{\rm dust}$. After this phase, the galaxies would reach a maximum in $sM_{\rm dust}$ before losing their dust grains and going down in the DFRD. At the end of this dust cycle, Burgarella et al. (2020) and Nanni et al. (2020) found that about 80% of the mass fraction of the total baryons had been removed by the outflow and the rest had mainly been destroyed by supernovae (SNe). However, we still have difficulty understanding the evolutionary status of galaxies with very high $sM_{\rm dust} > 0.01$. Calura et al. (2017) propose that spiral galaxies are characterized by a nearly constant $sM_{\rm dust}$ as a function of the stellar mass and cosmic time, whereas proto-spheroids present an early steep increase of the $sM_{\rm dust}$, which stops at a maximal value and decreases in the latest stages.

We built this same diagram from the large galaxy sample studied in this paper and for our two main models (delayed SFH with $\tau = 500$ Myr plus DL2014 and PL+OT_MBB for the IR emission). When using the module DL2014 in CIGALE, the dust mass is provided with the models. We note that the models of DL2014 assume an optically thin dust. The CIGALE module casey2012_OT, that is PL+OT_MBB, does not give $M_{\rm dust}$, and we need to compute it.

The IR SED

$$S_\nu \propto \nu^{\beta_{\rm RJ}} B_\nu(T_{\rm dust})$$

was computed with a modified blackbody

$$B_\nu(T_{\rm dust}) = \frac{2h}{c^2} \frac{\nu^3}{e^{\frac{h\nu}{kT_{\rm dust}}} - 1}$$

and the dust mass was derived with the following formula:

$$M_{\rm dust} = \frac{L_\nu}{4\pi\kappa_\nu B_\nu(T_{\rm dust})}$$

where $\nu = c/\lambda_{200\,\mu\rm m}$, h is the Planck constant, and c is the speed of light. We note that the emission of the CMB was neglected given the dust temperatures $T \gtrsim 40$ K found in this paper (da Cunha et al. 2013).

In the models for DL2014, the dust composition (Weingartner & Draine 2001) corresponds to 30% of graphite and 70% of silicate (MgFeSiO4). We first adopted the constant given in Draine (2003) at $\lambda = 200$ µm: $\kappa_0 = 0.637\,\mathrm{m^2\,kg^{-1}}$ because we also assumed $\lambda_0 = 200\,\mu$m, $\kappa_\nu = \kappa_0\,(\lambda_0/\lambda)^{\beta} = \kappa_0$. When comparing $M_{\rm dust}$(DL2014) to $M_{\rm dust}$(PL+OT_MBB), we found the latter to be systematically smaller by a factor of 0.37 ± 0.01. This was already noticed in several works (Magdis et al. 2013; Santini et al. 2014; Bianchi et al. 2019; Magnelli et al. 2012). The origin of this shift might be found in the single-temperature models that are unable to account for the wide range in the temperature of dust grains that are exposed to different intensities of the interstellar radiation field (see Liang et al. 2019, for a very pedagogical description).

Figure 11 presents the DFRD with data points color-coded with the parameters $\mathrm{age}_{\rm main}$. Only individual results obtained using DL2014 are shown. However, the trends are also presented for other dust emissions (PL+OT_MBB with various assumptions on κ_0, as explained below). The lines are based on a fit with only the ALMA-detected objects. We see an age sequence from right to left, that is with decreasing sSFR.

We note that $\kappa_0 = 0.637\ \mathrm{m^2\ kg^{-1}}$ corresponds to the dust opacity in the models of DL2014. In the early universe, most if not all of the dust could only be produced by SNe (e.g., Burgarella et al. 2020; Nanni et al. 2020). Hirashita et al. (2017) propose values for κ_0 for dust condensed in SNe before reverse shock destruction, $\kappa_{158\ \mu\rm m} = 0.557\,\mathrm{m^2\,kg^{-1}}$, and for dust ejected from SNe after reverse shock destruction, $\kappa_{158\ \mu\rm m} = 0.894\,\mathrm{m^2\,kg^{-1}}$. The dust composition and grain size distribution assumed in Hirashita et al. (2017) are from Nozawa et al. (2003). After correction to get these dust mass absorption coefficients at $\lambda = 200\,\mu$m using $\kappa_\nu = \kappa_0\,(\lambda_0/\lambda)^{\beta_{\rm RJ}}$ with $\beta_{\rm RJ}$ from the SED fitting (Table 4), we obtained $\kappa_0 = 0.45$ and $0.72\,\mathrm{m^2\ kg^{-1}}$. This means that, when adopting the SNe value for κ_0, the dust masses would be roughly of the same order as PL+OT_MBB with $\kappa_0 = 0.637\,\mathrm{m^2\,kg^{-1}}$. This is certainly a crucial point: given the age of these galaxies, it is very likely that the dust grains have been produced by SNe. So we could wonder how to reconcile this assumption with the fact that the present models are far from being able to reproduce diagnostic diagrams such as Fig. 11. This point is also debated from a laboratory standpoint. For instance, Fanciullo et al. (2020), Ysard et al. (2019) suggest that current dust masses are overestimated by up to a factor of 10–20 or 2–5, depending on the assumptions on grain structure (porous or compact, respectively). Laboratory measurements of dust analogs show that FIR opacities, that is to

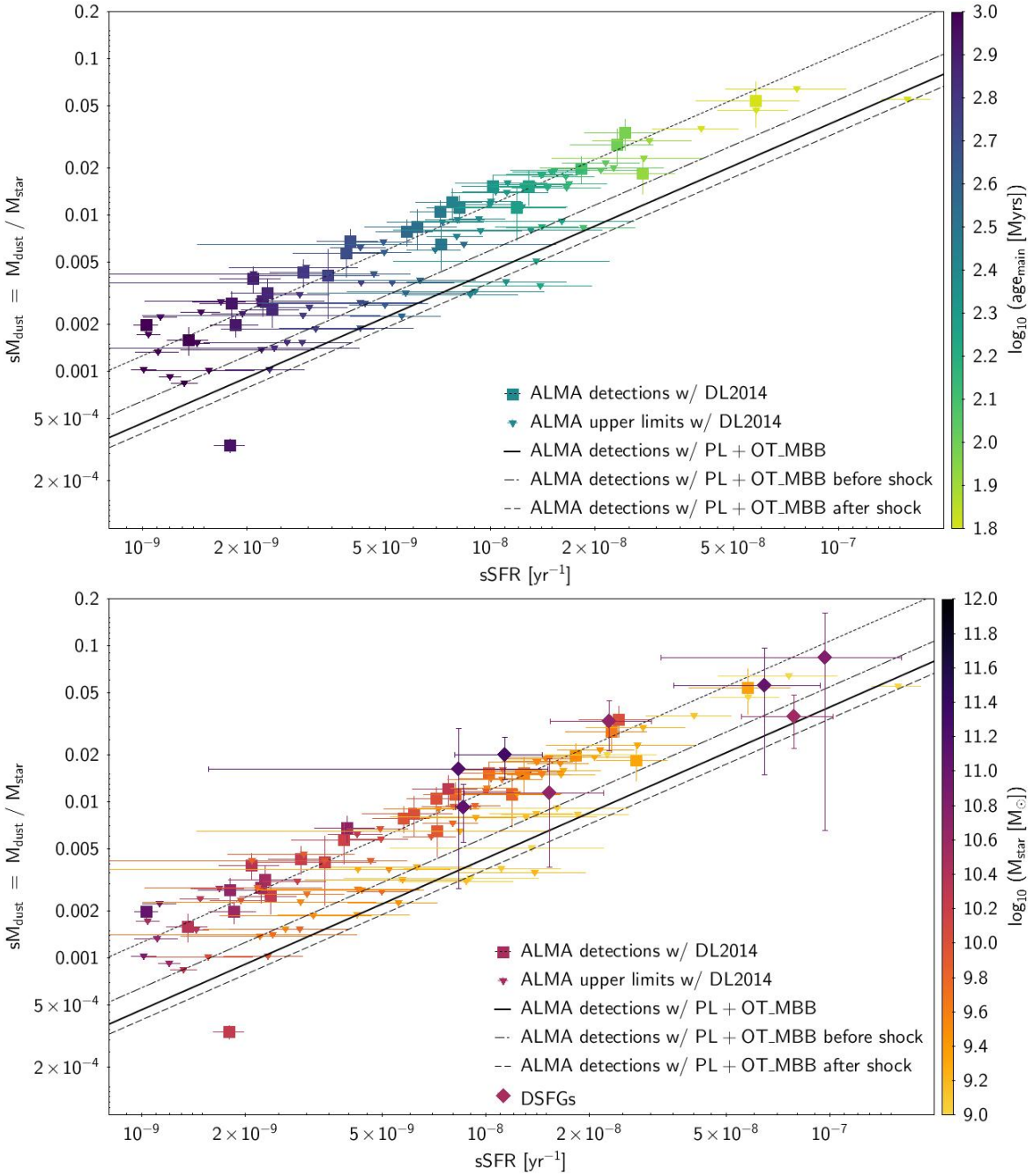

Fig. 11. Comparison of observed DFRDs with models. *Top*: DFRDs color-coded with $\log_{10}$age$_{\rm main}$. The individual symbols were computed assuming a PL+OT_MBB emission. We clearly observe an age sequence from right to left. The lines show the trend assuming different dust emissions and different values for κ_0. The top one assumes DL2014 dust emission. The second one from the top was derived when using an optically thin modified blackbody with $\kappa_0 = 0.637\,{\rm m^2\,kg^{-1}}$ (PL+OT_MBB). We note that the factor 0.37 needed to match DL2014 to PL+OT_MBB emission was not applied. The third one from the top assumes optically thin modified blackbodies with κ_0 corresponding to SNe dust mass absorption coefficients. It corresponds to the situation before the SNe reverse shock destruction, and the bottom line represents after the reverse shock destruction. Both from Hirashita et al. (2017). *Bottom*: same models as in as (*a*). The same objects plotted in (*a*) are color-coded in $M_{\rm star}$. A sample of DSFGs (Table 8), also color-coded in $M_{\rm star}$, was added to the plot with the code as follows: the upper triangle shows the maximum value, and the lower triangle shows the minimum value. These high redshift DSFGs are found on the same sequence as the other objects. However, these DSFGs have stellar masses larger than the underlying galaxy population that we study. It is important to note that the physical parameters (especially $M_{\rm star}$ because the IR emission is dominant) of these high redshift DSFGs have very large uncertainties and their position location in the diagram can almost cover the entire plot. Better estimates of these parameters coming from JWST would help.

say mass absorption coefficients, are usually higher than the values used in models and that they depend on several parameters, including temperature, composition, shape, and morphology, for instance. This would mean that dust mass estimates may be overestimated. The properties (e.g., dust composition and grain size) are still unknown for galaxies at a very large redshift. This is important when deriving the dust mass (e.g., Ysard et al. 2019; Hirashita et al. 2017; Inoue et al. 2020).

One interesting point, which is beyond of the scope of this work, is related to the nature of objects that are usually

Table 8. Physical parameters for the sample of high redshift dusty star-forming galaxies.

Id	z	μ	$M_{\rm dust}$	$M_{\rm dust}$_err	$M_{\rm star}$	$M_{\rm star}$_err	$M_{\rm gas}$	$M_{\rm gas}$_err	SFR	SFR_err	$f_{\rm gas}$ (*)	Ref
ADFS-27	5.7	1.0	4.2E9	0.4E9	2.1E11	0.6E11	2.1E11	0.2E11	2380	230	0.50	(1)
ADFS-27 N	5.7	1.0	2.6E9	0.4E9	1.6E11	1.3E11	1.2E11	0.1E11	1330	130	0.43	(1)
ADFS-27 S	5.7	1.0	1.5E9	0.2E9	4.6E10	1.5E10	9.4E10	0.8E10	1050	110	0.66	(1)
HFLS-3	6.3	2.2	1.3E9	0.3E9	3.7E10	1.1E10 (#)	1.0E11	0.1E11	2900	180	0.73	(2),(3)
SPT 0311-58 ($)	6.9	2.0	6.1E9	3.5E9	1.1E11	0.5E11	6.4E11	3.7E11	7082	3967	0.85	(4),(5)
SPT 0311-58W	6.9	2.2	5.5E9	3.5E9	6.6E10	4.4E10	5.9E11	3.7E11	6380	3960	0.90	(4),(5)
SPT 0311-58E	6.9	1.3	5.2E8	2.6E8	4.6E10	2.0E10	5.2E10	2.6E10	702	228	0.53	(4),(5)
GN10	5.3	1.0	1.1E9	4.4E8	1.2E11	0.6E10	7.1E10	0.9E10	1030	190	0.37	(6)

Notes. We note that the parameters were not corrected for the gravitational magnification. (*)$f_{\rm gas} = M_{\rm gas}/(M_{\rm gas} + M_{\rm star})$ were computed from the listed $M_{\rm gas}$ and $M_{\rm star}$ values. (#)No error quoted, we assume 30%. ($)The parameters for SPT031158 are the sum of the two components (W & E).
References. (1) Riechers et al. (2021), (2) Riechers et al. (2013), (3) Cooray et al. (2014), (4) Strandet et al. (2017); (5) Marrone et al. (2018), (6) Riechers et al. (2020).

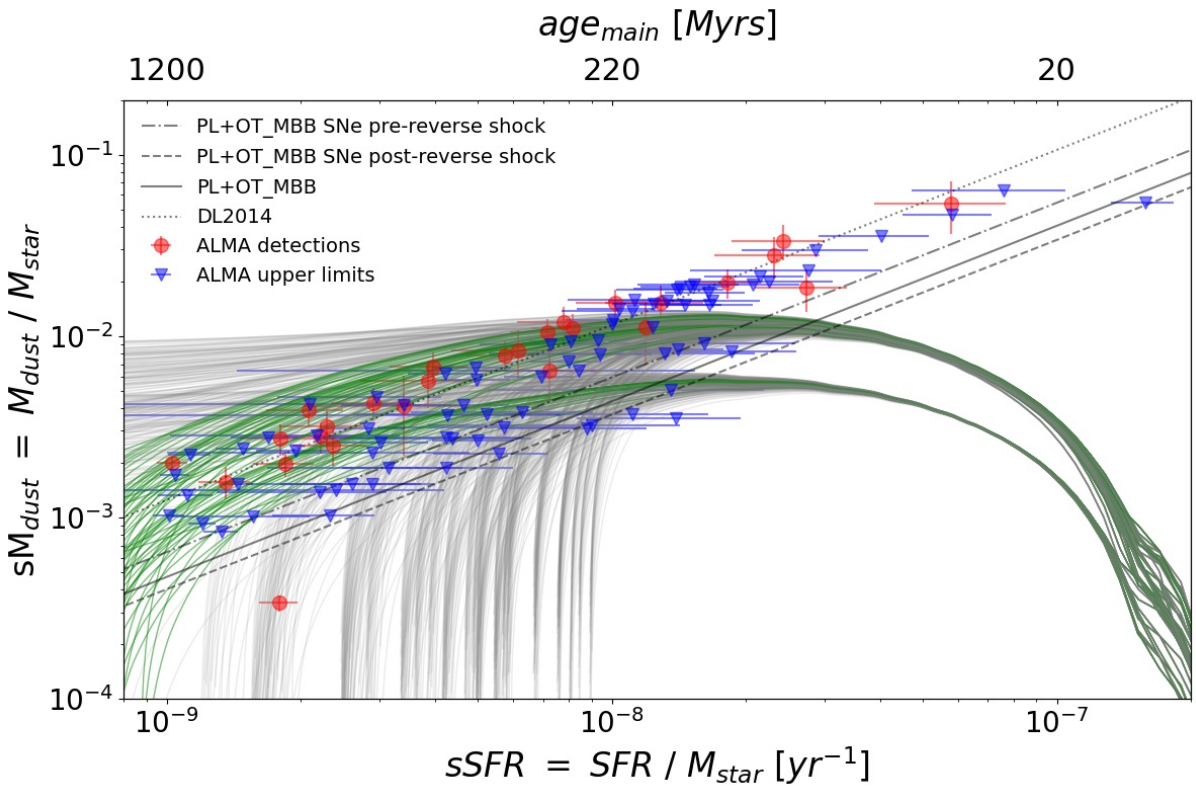

Fig. 12. DFRD for models with dust masses computed by CIGALE with DL2014 dust models. Only models with a delayed star formation history are plotted. A delayed star formation history only was consistently used in the SED fitting with CIGALE to estimate $sM_{\rm dust}$ and sSFR. The models shown do not have any grain growth in the ISM. We also show the other models in light gray to show which parameter space the models cover. On this figure, we superimposed the three lines that show the respective linear fits as in Fig. 11. The models shown are from Burgarella et al. (2020) and Nanni et al. (2020). This figure shows that most of the objects (ALMA detections and ALMA upper limits) are approximately located at the same positions as the models. Only HZ9 is found at larger sSFR and $sM_{\rm dust}$. If confirmed at this location in the DFRD, these objects would be very difficult to explain with these models.

considered to belong to another class: the high redshift dusty star-forming galaxies (DSFG) such as ADFS-27 (Riechers et al. 2021) or HFLS3 (Riechers et al. 2013). The very massive and very dusty galaxies have been found in the high redshift universe thanks to wide-field far-IR and submm observations with, for example, the South Pole Telescope or the European Space Agency's *Herschel* Space Observatory. High redshift DSFGs are at the high mass end, which suggests that they are not similar to the early phases of the SFGs analyzed here. In an attempt to check their location in the DFRD, we added the DFSGs from Table 8 to Fig. 12. All of them fall on the same sequence identified for our studied sample; however, they do not show the same stellar mass as our sample. We can wonder whether the stellar mass of these high redshift DSFGs are badly estimated or whether they follow a different path. It should be noticed that CIGALE with similar assumptions on the SFH and on the dust emission has been used for some of these objects, such as ADFS-27.

In Fig. 12, we compare the entire sample with the models built in Burgarella et al. (2020) and in Nanni et al. (2020). The models are fully explained in Nanni et al. (2020). In brief, we performed the calculations for the metal evolution using the

One-zone Model for the Evolution of GAlaxies (OMEGA) code (Côté et al. 2017). We assumed the metal yields for type II SNe from Kobayashi et al. (2006) computed up to 40 $M_\odot$, and from the FRUITY database for low-mass stars with $M > 1.3 M_\odot$ evolving through the thermally pulsing AGB phase and developing stellar winds (Cristallo et al. 2011, 2015; Piersanti et al. 2013). The yields for population III stars are from Heger & Woosley (2010) and are limited to the mass range $10 < M/M_\odot < 30$ in OMEGA. Dust removal from the galaxy through galactic outflow follows a rate proportional to the SFR through the "mass-loading factor": ML × SFR. This assumes that the galactic outflow is generated by the feedback of stars on the gas in the ISM (e.g., Murray et al. 2005). Two kinds of IMFs were tested: top-heavy IMFs and a Chabrier IMF. We assume that a fraction of silicates (olivine and pyroxene), iron, and carbon grains ejected in the ISM are condensed. The best models selected by Burgarella et al. (2020) generally agree with the Alpine sample. Only one object (HZ9 at sSFR $\sim 5 - 6 \times 10^{-8}$ yr^{-1}) lies at high sSFR. This is consistent with a fast evolution of these young objects, regardless of their $sM_{\rm dust}$. With the present data, we cannot rule out that the trend could keep rising to the right of the diagram. Galaxies have to start building dust grains early in their lifetime, at $\log_{10}$ sSFR $\geq 10^{-8} - 10^{-7}$ yr^{-1}, to the right of the DFRD. It therefore seems important to measure dust and stellar masses for galaxies at high sSFR and young ages to locate the locus of this rising $sM_{\rm dust}$ and thus bring some observational data to constrain the models.

5. Conclusions

This paper studies a sample of star-forming galaxies observed with ALMA in the redshift range $4.5 \lesssim z \lesssim 6.2$. Some of them, detected in the continuum with ALMA, were used to build a composite IR SED covering a large wavelength range from about 15 µm to 218 µm. Using CIGALE, we modeled the IR composite template and derived a set of physical properties. Building on the assumption that this IR composite template is valid for an ensemble of galaxies selected in the same way, such as ALPINE's SFGs and LBGs, we use it to fit the SEDs of the ALPINE sample plus the sample of LBGs from Burgarella et al. (2020) and Nanni et al. (2020) from the far-UV to the submm ranges.

The following results were found:

- We built a unique $z > 4$ IR SED. It is compatible with the ALPINE sample completed with galaxies from Burgarella et al. (2020) plus the $z \sim 4.5$ and $z \sim 5.5$ stacks from Bethermin et al. (2020). We provide a table to the readers with the raw composite IR SED and the modeled SEDs.
- Except for an SFH based on a delayed with a final burst history, all other SFHs (constant, delayed with $\tau_{\rm main} = 500$ Myr, and delayed with several $\tau_{\rm main}$) are in agreement with the data. For simplicity, we selected the delayed SFH with $\tau_{\rm main} = 500$ Myr.
- We checked the position of the sample in the SFR versus $M_{\rm star}$ diagram. The objects in the sample follow the same trend as those previously derived in papers at the same redshift.
- When comparing the position of the sample with the evolution in redshift of the IRX versus $M_{\rm star}$ relation found by Bogdanoska & Burgarella (2020) at $z \sim 4.5$ and at $z \sim 5.5$, we found a reasonable agreement. This agreement especially holds at $z \sim 5.5$. However, the absolute level of this flat relation must be reevaluated using detections of low-mass galaxies.
- The sample studied in this paper was placed in the IRX versus $\beta_{\rm FUV}$ diagram. An evolution in age is observed with younger galaxies having bluer $\beta_{\rm FUV}$.
- Moreover, our sample was found to be shifted to bluer $\beta_{\rm FUV}$ with respect to a $z = 0$ reference. We modeled this evolution with the mass-weighted age and provide an equation that allows one to predict the position of the sequence as a function of the redshift.
- We plotted our galaxies in the DFRD ($M_{\rm dust}/M_{\rm star}$ versus SFR/$M_{\rm star}$, DFRD). The objects form a sequence that can be described by evolution in various time-dependent parameters, and more specifically the age of the stellar populations and the stellar mass. This suggests that the sequence is due to the evolution of the galaxies over cosmic time.
- The models built by Burgarella et al. (2020), Nanni et al. (2020) are generally in agreement with the data, although the sample is much larger than in these previous papers.
- High redshift, high mass DSFGs over-plotted in the DFRD are found on the same sequence followed by our sample. However, the stellar mass estimated for these high redshift DSFGs are larger than the one found at the same locus for our sample. Uncertainties on the stellar mass of these objects are notoriously high because the stellar emission is faint, but the disagreement seems large. Better estimates of their stellar masses should be available if they are observed with JWST.

Acknowledgements. This program receives funding from the CNRS national program Cosmology and Galaxies. D.R. acknowledges support from the National Science Foundation under grant No. AST-1910107. D.R. also acknowledges support from the Alexander von Humboldt Foundation through a Humboldt Research Fellowship for Experienced Researchers. M.T. acknowledges the support from grant PRIN MIUR 2017 20173ML3WW 001. A.N. acknowledges support from the Narodowe Centrum Nauki (UMO-2018/30/E/ST9/00082 and UMO-2020/38/E/ST9/00077). G.C.J. acknowledges ERC Advanced Grant 695671 "QUENCH" and support by the Science and Technology Facilities Council (STFC). Y.F. further acknowledges support from NAOJ ALMA Scientific Research Grant number 2020-16B. M.R. acknowledges support from the Narodowe Centrum Nauki (UMO-2020/38/E/ST9/00077). M.B. gratefully acknowledges support by the ANID BASAL project FB210003 and from the FONDECYT regular grant 1211000. E.I. acknowledges partial support from FONDECYT through grant N° 1171710.

References

Álvarez-Márquez, J., Burgarella, D., Heinis, S., et al. 2016, A&A, 587, A122
Álvarez-Márquez, J., Burgarella, D., Buat, V., Ilbert, O., & Pérez-González, P. G. 2019, A&A, 630, A153
Arata, S., Yajima, H., Nagamine, K., Abe, M., & Khochfar, S. 2020, MNRAS, 498, 5541
Aretxaga, I., Wilson, G. W., Aguilar, E., et al. 2011, MNRAS, 415, 3831
Baes, M., Verstappen, J., De Looze, I., et al. 2011, ApJS, 196, 22
Bakx, T. J. L. C., Sommovigo, L., Carniani, S., et al. 2021, MNRAS, 508, L58
Bellstedt, S., Robotham, A. S. G., Driver, S. P., et al. 2021, MNRAS, 503, 3309
Bendo, G. J., Joseph, R. D., Wells, M., et al. 2003, AJ, 125, 2361
Bernhard, E., Béthermin, M., Sargent, M., et al. 2014, MNRAS, 442, 509
Bethermin, M., Fudamoto, Y., Ginolfi, M., et al. 2020, A&A, 643, A2
Bianchi, S., Casasola, V., Baes, M., et al. 2019, A&A, 631, A102
Bogdanoska, J., & Burgarella, D. 2020, MNRAS, 496, 5341
Boquien, M., Calzetti, D., Kennicutt, R., et al. 2009, ApJ, 706, 553
Boquien, M., Burgarella, D., Roehlly, Y., et al. 2019, A&A, 622, A103
Bouwens, R. J., Aravena, M., Decarli, R., et al. 2016, ApJ, 833, 72
Bruzual, G., & Charlot, S. 2003, MNRAS, 344, 1000
Buat, V., Takeuchi, T. T., Burgarella, D., Giovannoli, E., & Murata, K. L. 2009, A&A, 507, 693
Burgarella, D., Buat, V., & Iglesias-Páramo, J. 2005, MNRAS, 360, 1413
Burgarella, D., Buat, V., Gruppioni, C., et al. 2013, A&A, 554, A70
Burgarella, D., Nanni, A., Hirashita, H., et al. 2020, A&A, 637, A32
Calura, F., Pozzi, F., Cresci, G., et al. 2017, MNRAS, 465, 54
Calzetti, D., Kinney, A. L., & Storchi-Bergmann, T. 1994, ApJ, 429, 582
Calzetti, D., Armus, L., Bohlin, R. C., et al. 2000, ApJ, 533, 682
Capak, P. L., Carilli, C., Jones, G., et al. 2015, Nature, 522, 455
Carvajal, R., Bauer, F. E., Bouwens, R. J., et al. 2020, A&A, 633, A160
Casey, C. M. 2012, MNRAS, 425, 3094
Casey, C. M., Chen, C.-C., Cowie, L. L., et al. 2013, MNRAS, 436, 1919
Castellano, M., Sommariva, V., Fontana, A., et al. 2014, A&A, 566, A19
Chabrier, G. 2003, PASP, 115, 763

Ciesla, L., Boquien, M., Boselli, A., et al. 2014, A&A, 565, A128
Cooray, A., Calanog, J., Wardlow, J. L., et al. 2014, ApJ, 790, 40
Cormier, D., Abel, N. P., Hony, S., et al. 2019, A&A, 626, A23
Cortese, L., Boselli, A., Franzetti, P., et al. 2008, MNRAS, 386, 1157
Côté, B., O'Shea, W., Ritter, C., Herwig, F., & Venn, K. A. 2017, ApJ, 835, 128
Cousin, M., Buat, V., Lagache, G., & Bethermin, M. 2019, A&A, 627, A132
Cristallo, S., Piersanti, L., Straniero, O., et al. 2011, ApJS, 197, 17
Cristallo, S., Straniero, O., Piersanti, L., & Gobrecht, D. 2015, ApJS, 219, 40
Cucciati, O., Tresse, L., Ilbert, O., et al. 2012, A&A, 539, A31
Cunningham, D. J. M., Chapman, S. C., Aravena, M., et al. 2020, MNRAS, 494, 4090
da Cunha, E., Groves, B., Walter, F., et al. 2013, ApJ, 766, 13
De Breuck, C., Weiß, A., Béthermin, M., et al. 2019, A&A, 631, A167
Delvecchio, I., Daddi, E., Sargent, M. T., et al. 2021, A&A, 647, A123
Donnari, M., Pillepich, A., Nelson, D., et al. 2019, MNRAS, 485, 4817
Douglas, L. S., Bremer, M. N., Lehnert, M. D., Stanway, E. R., & Milvang-Jensen, B. 2010, MNRAS, 409, 1155
Draine, B. T. 2003, ARA&A, 41, 241
Draine, B. T., Aniano, G., Krause, O., et al. 2014, ApJ, 780, 172
Faisst, A. L., Capak, P. L., Yan, L., et al. 2017, ApJ, 847, 21
Faisst, A. L., Schaerer, D., Lemaux, B. C., et al. 2020a, ApJS, 247, 61
Faisst, A. L., Fudamoto, Y., Oesch, P. A., et al. 2020b, MNRAS, 498, 4192
Fanciullo, L., Kemper, F., Scicluna, P., Dharmawardena, T. E., & Srinivasan, S. 2020, MNRAS, 499, 4666
Fernández-Ontiveros, J. A., Spinoglio, L., Pereira-Santaella, M., et al. 2016, ApJS, 226, 19
Fudamoto, Y., Oesch, P. A., Faisst, A., et al. 2020, A&A, 643, A4
Fujimoto, S., Silverman, J. D., Bethermin, M., et al. 2020, ApJ, 900, 1
Galametz, M., Kennicutt, R. C., Albrecht, M., et al. 2012, MNRAS, 425, 763
Giacconi, R., Zirm, A., Wang, J., et al. 2002, VizieR Online Data Catalog: II/13
Gordon, K. D., Clayton, G. C., Misselt, K. A., et al. 2003, ApJ, 594, 279
Grogin, N. A., Kocevski, D. D., Faber, S. M., et al. 2011, ApJS, 197, 35
Gruppioni, C., Pozzi, F., Rodighiero, G., et al. 2013, MNRAS, 432, 23
Harikane, Y., Ouchi, M., Yuma, S., et al. 2014, ApJ, 794, 129
Harikane, Y., Ouchi, M., Inoue, A. K., et al. 2020, ApJ, 896, 93
Hashimoto, T., Laporte, N., Mawatari, K., et al. 2018, Nature, 557, 392
Hashimoto, T., Inoue, A. K., Mawatari, K., et al. 2019, PASJ, 71, 71
Heger, A., & Woosley, S. E. 2010, ApJ, 724, 341
Helou, G., Soifer, B. T., & Rowan-Robinson, M. 1985, ApJ, 298, L7
Hirashita, H., Burgarella, D., & Bouwens, R. J. 2017, MNRAS, 472, 4587
Hunt, L. K., Testi, L., Casasola, V., et al. 2014, A&A, 561, A49
Inoue, A. K., Tamura, Y., Matsuo, H., et al. 2016, Science, 352, 1559
Inoue, A. K., Hashimoto, T., Chihara, H., & Koike, C. 2020, MNRAS, 495, 1577
Jones, G. C., Maiolino, R., Caselli, P., & Carniani, S. 2020, MNRAS, 498, 4109
Juvela, M., Montillaud, J., Ysard, N., & Lunttila, T. 2013, A&A, 556, A63
Kass, R. E., & Raftery, A. E. 1995, J. Am. Stat. Assoc., 90, 773
Kelly, B. C. 2007, ApJ, 665, 1489
Khusanova, Y., Bethermin, M., Le Fèvre, O., et al. 2021, A&A, 649, A152
Kobayashi, C., Umeda, H., Nomoto, K., Tominaga, N., & Ohkubo, T. 2006, ApJ, 653, 1145
Koekemoer, A. M., Faber, S. M., Ferguson, H. C., et al. 2011, ApJS, 197, 36
Komatsu, E., Smith, K. M., Dunkley, J., et al. 2011, ApJS, 192, 18
Kong, X., Charlot, S., Brinchmann, J., & Fall, S. M. 2004, MNRAS, 349, 769
Koprowski, M. P., Coppin, K. E. K., Geach, J. E., et al. 2020, MNRAS, 492, 4927
Lagache, G., Cousin, M., & Chatzikos, M. 2018, A&A, 609, A130
Laporte, N., Katz, H., Ellis, R. S., et al. 2019, MNRAS, 487, L81
Le Fèvre, O., Béthermin, M., Faisst, A., et al. 2020, A&A, 643, A1
Leitherer, C., Calzetti, D., & Martins, L. P. 2002, ApJ, 574, 114
Liang, L., Feldmann, R., Kereš, D., et al. 2019, MNRAS, 489, 1397
Lutz, D., Poglitsch, A., Altieri, B., et al. 2011, A&A, 532, A90
Ma, X., Hopkins, P. F., Faucher-Giguère, C.-A., et al. 2016, MNRAS, 456, 2140
Madau, P., & Dickinson, M. 2014, ARA&A, 52, 415
Madau, P., Ferguson, H. C., Dickinson, M. E., et al. 1996, MNRAS, 283, 1388
Madden, S. C., Rémy-Ruyer, A., Galametz, M., et al. 2013, PASP, 125, 600
Magdis, G. E., Rigopoulou, D., Helou, G., et al. 2013, A&A, 558, A136
Magnelli, B., Lutz, D., Santini, P., et al. 2012, A&A, 539, A155
Marrone, D., Spilker, J. S., Hayward, C. C., et al. 2018, Nature, 553, 51
McLure, R. J., Dunlop, J. S., Cullen, F., et al. 2018, MNRAS, 476, 3991
Murray, N., Quataert, E., & Thompson, T. A. 2005, ApJ, 618, 569
Nanni, A., Burgarella, D., Theulé, P., Côté, B., & Hirashita, H. 2020, A&A, 641, A168
Nelson, D., Pillepich, A., Springel, V., et al. 2018, MNRAS, 475, 624
Nozawa, T., Kozasa, T., Umeda, H., Maeda, K., & Nomoto, K. 2003, ApJ, 598, 785
O'Halloran, B., Galametz, M., Madden, S. C., et al. 2010, A&A, 518, L58
Oliver, S. J., Bock, J., Altieri, B., et al. 2012, MNRAS, 424, 1614
Ouchi, M., Yamada, T., Kawai, H., & Ohta, K. 1999, ApJ, 517, L19
Overzier, R. A., Heckman, T. M., Schiminovich, D., et al. 2010, ApJ, 710, 979
Pavesi, R., Riechers, D. A., Capak, P. L., et al. 2016, ApJ, 832, 151
Pavesi, R., Riechers, D. A., Faisst, A. L., Stacey, G. J., & Capak, P. L. 2019, ApJ, 882, 168
Pearson, E. A., Eales, S., Dunne, L., et al. 2013, MNRAS, 435, 2753
Pearson, W. J., Wang, L., Hurley, P. D., et al. 2018, A&A, 615, A146
Piersanti, L., Cristallo, S., & Straniero, O. 2013, ApJ, 774, 98
Pilbratt, G. L., Riedinger, J. R., Passvogel, T., et al. 2010, A&A, 518, L1
Pillepich, A., Nelson, D., Hernquist, L., et al. 2018, MNRAS, 475, 648
Pozzi, F., Calura, F., Fudamoto, Y., et al. 2021, A&A, 653, A84
Raftery, A. E. 1998, Bayes Factors and BIC: Comment on Weakliem
Riechers, D. A., Bradford, C. M., Clements, D. L., et al. 2013, Nature, 496, 329
Riechers, D. A., Hodge, J. A., Pavesi, R., et al. 2020, ApJ, 895, 81
Riechers, D. A., Nayyeri, H., Burgarella, D., et al. 2021, ApJ, 907, 62
Rodighiero, G., Daddi, E., Baronchelli, I., et al. 2011, ApJ, 739, L40
Salim, S., Lee, J. C., Janowiecki, S., et al. 2016, ApJS, 227, 2
Santini, P., Maiolino, R., Magnelli, B., et al. 2014, A&A, 562, A30
Schaerer, D., Ginolfi, M., Béthermin, M., et al. 2020, A&A, 643, A3
Schulz, S., Popping, G., Pillepich, A., et al. 2020, MNRAS, 497, 4773
Scoville, N., Aussel, H., Brusa, M., et al. 2007, ApJS, 172, 1
Scoville, N., Sheth, K., Aussel, H., et al. 2016, ApJ, 820, 83
Shapley, A. E., Steidel, C. C., Pettini, M., & Adelberger, K. L. 2003, ApJ, 588, 65
Sherman, S., Jogee, S., Florez, J., et al. 2021, MNRAS, 505, 947
Strandet, M. L., Weiss, A., De Breuck, C., et al. 2017, ApJ , 842, L15
Speagle, J. S., Steinhardt, C. L., Capak, P. L., & Silverman, J. D. 2014, ApJS, 214, 15
Sugahara, Y., Inoue, A. K., Hashimoto, T., et al. 2021, ApJ, 923, 5
Tabatabaei, F. S., Braine, J., Xilouris, E. M., et al. 2014, A&A, 561, A95
Takeuchi, T. T., Buat, V., Heinis, S., et al. 2010, A&A, 514, A4
Tibbs, C. T., Israel, F. P., Laureijs, R. J., et al. 2018, MNRAS, 477, 4968
Volinsky, C. T. 1997, Ph.D. Thesis, University of Washington
Weingartner, J. C., & Draine, B. T. 2001, ApJ, 548, 296
Willott, C. J., Carilli, C. L., Wagg, J., & Wang, R. 2015, ApJ, 807, 180
Witt, A. N., & Gordon, K. D. 2000, ApJ, 528, 799
Xu, C. K., Shupe, D., Buat, V., et al. 2007, ApJS, 173, 432
Ysard, N., Koehler, M., Jimenez-Serra, I., Jones, A. P., & Verstraete, L. 2019, A&A, 631, A88
Yuan, F.-T., Burgarella, D., Corre, D., et al. 2019, A&A, 631, A123

[1] Aix Marseille Univ, CNRS, CNES, LAM, Marseille, France
e-mail: denis.burgarella@lam.fr
[2] National Centre for Nuclear Research, ul.Pasteura 7, 02-093 Warszawa, Poland
[3] INAF – Osservatorio di Astrofisica e Scienza dello Spazio di Bologna, Via Gobetti 93/3, 40129 Bologna, Italy
[4] Centro de Astronomía (CITEVA), Universidad de Antofagasta, Avenida Angamos 601, Antofagasta, Chile
[5] IPAC, California Institute of Technology, 1200 East California Boulevard, Pasadena, CA 91125, USA
[6] Department of Astronomy, University of Geneva, ch. des Maillettes 51, 1290 Versoix, Switzerland
[7] National Astronomical Observatory of Japan, 2-21-1, Osawa, Mitaka, Tokyo, Japan
[8] Research Institute for Science and Engineering, Waseda University, 3-4-1 Okubo, Shinjuku, Tokyo 169-8555, Japan
[9] Cosmic Dawn Center (DAWN), Jagtvej 128, 2200 Copenhagen N, Denmark
[10] Niels Bohr Institute, University of Copenhagen, Lyngbyvej 2, 2100 Copenhagen, Denmark
[11] University of Massachusetts, 710 N. Pleasant St, LGRB-520, Amherst, MA 01003, USA
[12] European Southern Observatory, Karl-Schwarzschild-Str. 2, 85748 Garching bei München, Germany
[13] Istituto Nazionale di Astrofisica: Osservatorio di Astrofisica e Scienza dello Spazio di Bologna, Via Gobetti 93/3, 40129 Bologna, Italy
[14] Space Telescope Science Institute, 3700 San Martin Drive, Baltimore, MD 21218, USA
[15] Instituto de Física y Astronomía, Universidad de Valparaíso, Avda. Gran Bretaña 1111, Valparaíso, Chile

[16] Cavendish Laboratory, University of Cambridge, 19 J. J. Thomson Ave., Cambridge CB3 0HE, UK
[17] Kavli Institute for Cosmology, University of Cambridge, Madingley Road, Cambridge CB3 0HA, UK
[18] Institute of Astronomy, School of Science, The University of Tokyo, 2-21-1 Osawa, Mitaka, Tokyo 181-0015, Japan
[19] Research Center for the Early Universe, School of Science, The University of Tokyo, 7-3-1 Hongo, Bunkyo, Tokyo 113-0033, Japan
[20] Department of Physics, University of California, Davis, One Shields Ave., Davis, CA 95616, USA
[21] Gemini Observatory, NSF's NOIRLab, 670 N. A'ohoku Place, Hilo, HI 96720, USA
[22] Department of Astronomy, University of Florida, 211 Bryant Space Sciences Center, Gainesville, FL 32611, USA
[23] Institute for Cosmic Ray Research, The University of Tokyo, 5-1-5 Kashiwanoha, Kashiwa, Chiba 277-8582, Japan
[24] Kavli Institute for the Physics and Mathematics of the Universe (WPI), The University of Tokyo, 5-1-5 Kashiwanoha, Kashiwa, Chiba 277-8583, Japan
[25] Cornell University, Space Sciences Building, Ithaca, NY 14853, USA
[26] Dipartimento di Fisica e Astronomia, Università degli Studi di Bologna, Via P. Gobetti 93/2, 40129 Bologna, Italy
[27] Dipartimento di Fisica e Astronomia, Università di Padova, Vicolo dell'Osservatorio 3, 35122 Padova, Italy
[28] INAF – Osservatorio Astronomico di Padova, Vicolo dell'Osservatorio 5, 35122 Padova, Italy
[29] Institut de Recherche en Astrophysique et Planétologie – IRAP, CNRS, Université de Toulouse, UPS-OMP, 14, avenue E. Belin, 31400 Toulouse, France
[30] University of Bologna – Department of Physics and Astronomy "Augusto Righi" (DIFA), Via Gobetti 93/2, 40129 Bologna, Italy
[31] Dipartimento di Fisica e Astronomia Galileo Galilei Universitá degli Studi di Padova, Vicolo dell'Osservatorio 3, 35122 Padova, Italy
[32] Institut Universitaire de France, IUF, Paris, France

Appendix A: CIGALE parameters for the initial fits

A.1. Star formation histories (SFHs)

* A delayed SFH: SFR(t) = $t/\tau^2_{\rm main}$ exp($-t/\tau_{\rm main}$) with $\tau_{\rm main}$ in the range 25 to 10000 Myrs and main ages (t or $age_{\rm main}$) in the range 2 - 1200 Myrs is the first option. This type of SFH allows for SFRs to increase or decrease, depending on the age of the stellar population.
* The second option is a delayed SFH and a final young burst with the burst age (age_{burst}) are in the range 2 to 50 Myrs, but main ages are in the range 100 to 1200 Myrs, and the fraction of burst (f_{burst}) is as follows: 0.0, 0.001, 0.01, 0.10, 0.50 and τ_{burst} = 20000Myrs, that is to say it is similar to a constant SFH given the burst ages.
* Fixed parameters: because it was not possible to estimate $\tau_{\rm main}$ with confidence, we also sequentially fixed and tried $\tau_{\rm main}$ = 25, 250, and 2500 Myrs both for the delayed and burst runs before comparing the results to the above runs.

A.2. Dust characteristics

* The models from Draine et al. (2014): because no data are available in the rest-frame near-IR and mid-IR, we could not constrain the mass fraction of PAH ($q_{\rm PAH}$). However, it is generally accepted (e.g., Douglas et al. 2010; Castellano et al. 2014; Yuan et al. 2019; Bellstedt et al. 2021) that the metallicity of these galaxies are likely sub-solar. Ciesla et al. (2014) show a relation between $q_{\rm PAH}$ and the metallicity. Without any other constraint, we arbitrarily chose a low value for the mass fraction of PAH: $q_{\rm PAH}$=0.47. The impact of this parameter on the dust mass or luminosity is very low. We used the full range of allowed parameters for the minimum of the distribution of the starlight intensity relative to the local interstellar radiation field, $U_{\rm min}$, for α, the power law slope dU/dM = U^{α}, as well as for γ, the fraction of the dust heated by starlight above the lower cutoff U_{min}. For the same reason as for $\tau_{\rm main}$, in the SFH parameters, we also sequentially tried fixed values for α = 1.0, 2.0, and 3.0.
* Modified blackbody plus a power law similar to Casey (2012): Our initial priors are the dust temperature in the range 30K $\leq T_{\rm dust} \leq$ 85K and the emissivity in the RJ part of the SED $0.5 \leq \beta_{\rm RJ} \leq 2.0$. We kept the MIR power slope at the default α_{MIR} = 2.0 because no data are available to constrain α_{MIR}. These values are consistent with Faisst et al. (2020b), that is $40 < T_{\rm dust}$[K] < 60 (called T_{SED}, i.e., SED dust temperature in their paper), with a median at 48 K and emissivity indices (β_d in their paper) between 1.6 and 2.4 for all galaxies, and a median of 2.0. As before, because it could not be safely estimated with the data available, we tried several fixed values for $\beta_{\rm RJ}$= 1.0, 1.5, and 2.0.
* Other parameters: In addition to these parameters, we selected a Chabrier IMF and a wide range of dust attenuation. We selected CIGALE's dust attenuation law from the Calzetti and Leitherer module. It is based on the Calzetti et al. (2000) starburst attenuation curve, extended with the Leitherer et al. (2002) curve between the Lyman break and 120 nm. A nebular contribution was also added (see Boquien et al. 2019) where D_λ is the Drude profile, and the last term renormalizes the curve so that E(B-V) remains equal to the input E(B-V) when δ is not 0:

$$k_\lambda = k_\lambda^{starburst} \times (\lambda/\lambda_V)^\delta \times D_\lambda) \frac{E(B-V)_{\delta=0}}{E(B-V)_\delta}.$$

In Boquien et al. (submitted), a variation of the dust attenuation law is studied. However, changes in the shape of the dust attenuation law do not impact the IRX versus $A_{\rm FUV}$ relation for star forming galaxies because it is almost completely independent of the extinction mechanisms (i.e., dust and star geometry, attenuation law (e.g., Witt & Gordon 2000; Cortese et al. 2008, and references therein).

Finally, from these initial fits, we examined and discarded the fits for which the reduced $\chi^2_\nu \geq 5.0$ for each of our detected objects. These bad fits only represent a few of them with respect to all of the attempts. For each object in the sample, we computed the mean normalization factor from the CIGALE Bayesian luminosity at 200 µm: $L_{200\mu m}$. After applying this normalization, all the observed SEDs started to share the same flux density at λ = 200 μm: f_ν(200 μm) = 1.0 (see Fig.1) and we could then proceed to the next phase to try and combine all the observed SEDs into a single one.

Appendix B: CIGALE parameters for the final fit

Table B.1. CIGALE modules and input parameters used for all the fits. BC03 means Bruzual & Charlot (2003), and the Chabrier IMF refers to Chabrier (2003).

Parameters	**Symbol**	**Range (Ph. 2, DL2014)**	**Range (Ph. 2, PL+OT_MBB)**
Target sample		Individual Hi-z LBGs	Individual Hi-z LBGs
Delayed SFH and recent burst			
e-folding time scale of the delayed SFH	τ_{main} [Myr]	500	500
Age of the main population	Age$_{main}$[Myr]	101 log values in [2 - 1200]	101 log values in [2 - 1200]
Burst	f$_{burst}$	No burst	No burst
SSP			
SSP		BC03	BC03
Initial mass function	IMF	Chabrier	Chabrier
Metallicity	Z	0.004	0.004
Nebular emission			
Ionization parameter	logU	-2.5, -2.0, -1.5	-2.5, -2.0, -1.5
Line width [km/s]	—	100	100
Dust attenuation law			
Color excess for both the old and young stellar populations	E_BV_lines	101 log values in [0.01, 1.0]	101 log values in [0.01, 1.0]
Bump amplitude	uv_bump_amplitude	0.0	0.0
Power law slope	power law_slope	0.0	0.0
Dust emission (DL2014)			
Mass fraction of PAH	q_{PAH}	0.47	—
Minimum radiation field	U$_{min}$	17.0	—
Power law slope dU/dM $\approx$ U$^{\alpha}$	— α	2.4	
Dust fraction in PDRs	γ	0.54	—
Dust emission (PL + OT_MBB)			
Dust temperature	T_{dust}	—	54.1
Emissivity	β_{RJ}	—	0.87
Slope of the MIR power law	α_{MIR}	—	2.0
No AGN emission			

Appendix C: Results for the mock analysis performed with CIGALE

Table C.1. IR composite built from the sample of ALMA-detected objects. S/N = -1.00 and negative errors mean that the data in the given band is an upper limit.

id	λ [μm]	f_ν / $f_{200\mu m}$	error	S/N
Stack_hiz_0	15.484	0.6041071368176998	-0.6041071368176998	-1.0
Stack_lowz_0	18.299	0.4070780403478624	-0.4070780403478624	-1.0
Stack_hiz_1	24.905	1.8794443589743441	-1.8794443589743441	-1.0
Stack_lowz_1	29.434	1.139818500842144	-1.139818500842144	-1.0
Stack_hiz_2	38.196	1.9465673074955887	1.141091225093072	1.7058822859117322
Stack_lowz_2	45.141	2.035390171409635	0.6513248402928382	3.1250000698491944
Stack_hiz_3	53.562	3.356150626736888	1.2753372221566444	2.631578980390385
Stack_lowz_3	63.3	3.5822866822699644	0.8141560806957248	4.399999910593035
Stack_hiz_4	77.043	2.8191664384404334	1.0068452280294997	2.799999801317859
Stack_lowz_4	91.051	3.9079490417570293	0.8141560806957248	4.799999821186068
Band_0	130.428	2.3607768939276412	0.2981832794287399	7.91720078486769
Band_1	130.436	2.165732599053267	0.6473943153826967	3.345306789994023
Band_2	130.593	1.7383349717928915	0.06065561941986783	28.65909190968541
Stack_hiz_5	131.912	2.886289587003844	0.7383531338812721	3.9090909952959745
Band_3	132.807	1.981433127078801	0.16127944689702453	12.285713804214174
Band_4	132.932	2.1963292681861524	0.37231538599521935	5.899109601165808
Band_5	132.969	2.080220715848803	0.4840117172916773	4.297872637234547
Band_6	132.988	2.1875912071262826	0.47910729937980717	4.56597344677918
Band_7	133.815	1.926573426556951	0.49219554067981136	3.914243968760878
Band_8	136.152	2.057241450590362	0.6135251699120721	3.353149229207984
Band_9	138.248	2.0799540884965326	0.3253903546858025	6.392181140418067
Band_10	140.737	1.967469090431378	0.5666501690993686	3.4721053618645614
Band_11	151.261	1.668029595671763	0.33084882759697015	5.0416669383024235
Band_12	155.91	1.7071804939961757	0.5190183719080613	3.2892486786548374
Band_13	155.958	1.7343377926481176	0.5241091851108297	3.3091154322765193
Band_14	155.98	1.7165841217676614	0.44392731378008465	3.866813481582782
Band_15	156.087	1.5105290584441402	0.2577302260446886	5.86089214922826
Band_16	156.44	1.6482686941510394	0.1983141484234364	8.31140242516479
Band_17	156.88	1.4993950340478046	0.08418023607021971	17.811722846643843
Stack_lowz_5	156.946	1.465480981647917	0.569909250421072	2.57142866266017
Band_18	156.974	1.6857717137991153	0.3374836213241303	4.995121562299597
Band_19	157.337	1.6392424594698074	0.327254926319203	5.009068856219135
Band_20	157.596	1.6579979296267946	0.30177525864408145	5.494147986406877
Band_21	157.628	1.4474635873563206	0.2757073666017081	5.249999683350329
Band_22	158.184	1.6549383338003856	0.36096258262153563	4.5847919243628805
Band_23	159.984	1.7296819522255344	0.5653448382309686	3.0595166617916165
Band_24	160.702	1.5750590728174647	0.05011551777173926	31.428570288176477
Band_25	160.8	1.5945760229282628	0.4517856276440482	3.529497012208174
Stack_hiz_6	172.389	0.671230135349486	0.46986108974358604	1.428571443776695
Band_26	174.461			
Band_27	176.835	1.2341998894178108	0.1234199931599031	9.99999965823025
Band_28	181.442			
Band_29	192.119	1.1993270334194406	0.19299515456701574	6.214285721888348
Stack_lowz_6	203.732	0.6513248402928382	0.3256624201464191	2.0
Band_30	204.438	0.9511903973153636	0.15163904854966956	6.272727285042283
Band_31	204.647	1.0023103287640929	0.028637439202970513	34.99999848660089
Band_32	218.164	0.7875295364087324	0.028637439202970513	27.499998544808548

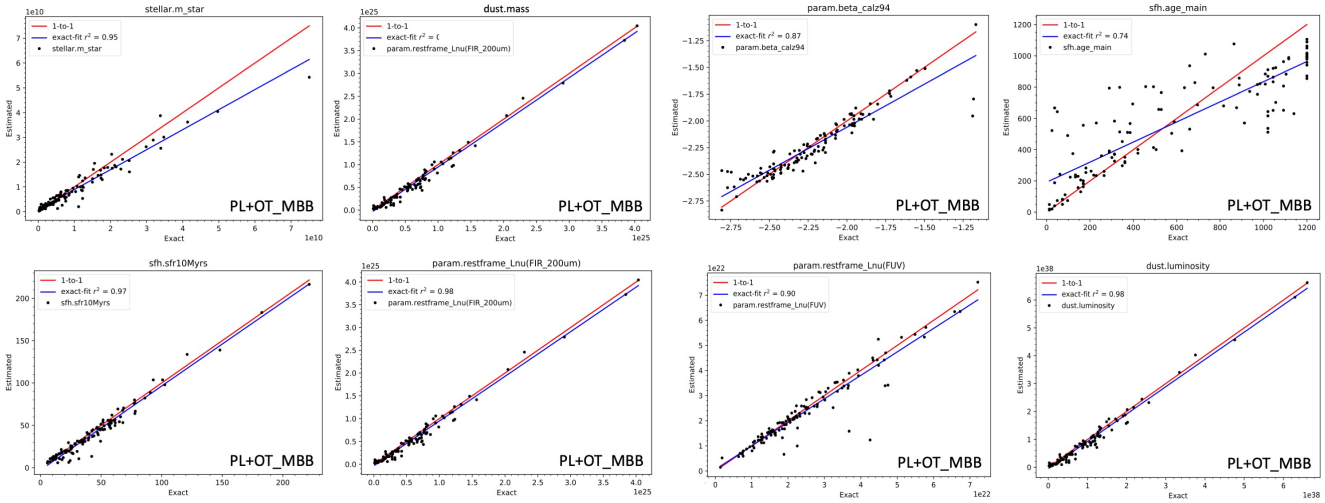

(a) Mock analysis using the power law and OT_MBB in the mid-IR as in Casey et al. (2012) for the IR template.

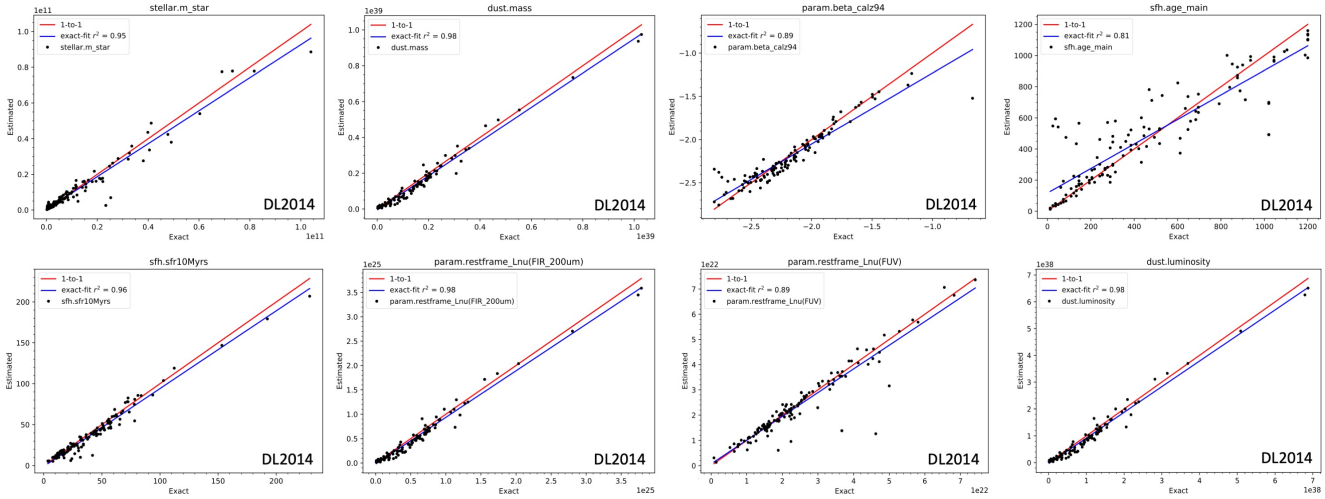

(b) Mock analysis using the DL2014 model for the IR template.

Fig. C.1. Results from the mock analysis performed with CIGALE where we compared input parameters (i.e., parameters from the best fit for each object) to the same parameters estimated by CIGALE with the very same priors used for the true analysis (see Boquien et al. 2019). We note that some parameters were estimated from another one via a linear relation, e.g., $M_{\rm dust}$ from $L_{200\mu m}$, which explains why the figures are identical.

Appendix D: The observed IR composite template

Table D.1. IR template for each of the models, normalized to 200 μm. Only the first rows are given here.

Beginning of table			
$\lambda[\mu m]$	F_ν(DL2014)	F_ν(PL+OTMBB)	F_ν(PL+GMBB)
20.0	0.18107749474964585	0.033371661115243596	0.22818696797630056
20.14	0.18551481313133614	0.03558839180505059	0.23284902077654243
20.32	0.1916912479528318	0.038600899856686154	0.23899800048124503
20.51	0.19834306021901293	0.0419773937900743	0.2456753421353187
20.7	0.20531825078431543	0.0455757038111942	0.25255705038272314
20.867	0.21165231238228988	0.048922292048504665	0.2587737366722555
20.89	0.21253443514863027	0.04939717591545251	0.2596425809753937
21.09	0.21999878126005848	0.05366062340145448	0.26731997222221277
21.28	0.22778655101786716	0.057962443464595954	0.27483454092275683
21.48	0.23581520065227968	0.0627535518665652	0.28297431584426264
21.68	0.24424326271690508	0.06781394324414101	0.291347963724405
21.88	0.25299471730114265	0.07316857457031122	0.29996899869856025
22.08	0.26199354449542767	0.07881443965404047	0.3088337861700852
22.082	0.26208493650531245	0.07887231603830122	0.3089236300384457
22.28	0.2712340694615609	0.0847529197682631	0.3179420030659557
22.49	0.2808044784109833	0.09132381546404349	0.3277767823905905
22.7	0.2906982948240248	0.0982402248996817	0.337888211755694
22.91	0.30092199306747625	0.10549864770034634	0.3482725682829296
23.12	0.31162760870823614	0.11312255020626029	0.358939632786215
23.33	0.32273912203875704	0.12111043969589304	0.3698864279648628
23.367	0.3246328638140299	0.12255295860875007	0.3718428283287594
23.55	0.33410507998527345	0.1298658169010314	0.3816513341074053
23.77	0.34580753271713527	0.13903942549564813	0.39372695656140905
23.99	0.3579158978811169	0.14862939797504734	0.406109743855343
24.21	0.3704366500235844	0.1586315049734245	0.418795702479763
24.43	0.3832937696207079	0.16906436125192464	0.4317889584821318
24.66	0.3964937065636398	0.18043150123404914	0.4456979944500126
24.728	0.40048918485669327	0.18387449065390407	0.44987131145069026
24.89	0.4101129611054971	0.19226129750006174	0.4599346258577945
25.12	0.4239927698164249	0.20457181854839696	0.4744999741413267
25.35	0.4383804218061039	0.21735893011265744	0.4893891153546033
25.59	0.4531109187014845	0.23120281058256145	0.5052659637022994
25.82	0.46819722620993215	0.24496358266472368	0.5208047830612047
26.06	0.48371533973635106	0.2598328633318763	0.5373512630332274
26.167	0.49078470206721386	0.26662418026629237	0.5448366626782501
26.3	0.49966558995663873	0.27521548353962055	0.5542326650492978
26.55	0.5160479316020455	0.2917929980735861	0.5721659193874856
26.79	0.5328055105216525	0.3082335832384853	0.5897098651878467
27.04	0.5499949190914902	0.32589907659217654	0.6083221832830993
27.29	0.5675660383130344	0.34411734454148923	0.6272664840356141
27.54	0.5855819344304354	0.36288115715867053	0.6465352562903721
27.69	0.5961897531348711	0.37439746768578636	0.6582511056055635
27.8	0.6040492950582195	0.3829655858786667	0.6669161355194035
28.05	0.6228986721642351	0.40282101937482206	0.686824222316167
28.31	0.642212273073861	0.424026173695583	0.7078423399760442
28.58	0.661914071623796	0.4466381770165294	0.7300068789223161
28.84	0.6820865555535788	0.46896879549147735	0.7516515252016847
29.11	0.7026537063446253	0.49272398228550457	0.7744316074517003
29.302	0.7175269391168585	0.5099619803515605	0.7908160789531954
29.38	0.7236286072319216	0.5170490187762744	0.7975206334362198
29.65	0.7450049892059205	0.5419215354053214	0.8208883852937892
29.92	0.7668650209888308	0.5673280370030406	0.8445244955008843
30.2	0.7890631462650731	0.5942344748886714	0.8693211602145551
30.48	0.8116753732562163	0.6216786189421348	0.8943731286693564
30.76	0.8350187262608603	0.6496426282732526	0.9196662732346107

Table D.1. Continuation of Table D.1

Beginning of table

$\lambda[\mu m]$	F_ν(DL2014)	F_ν(PL+OTMBB)	F_ν(PL+GMBB)
31.008	0.8548595738509837	0.6748402877570486	0.942270609355281
31.05	0.8582505863484577	0.679152332769373	0.9461231546231149
31.33	0.8823853875605483	0.7081317826121426	0.9718786649324272
31.62	0.9066496661110436	0.738629003785026	0.9987558240804495
31.92	0.9310434163236954	0.7706998525777717	1.0267876596063015
32.21	0.9563268030679799	0.8021530236075685	1.0540570673591256
32.51	0.9817396567584628	0.8351333801848314	1.0824275627010183
32.81	1.007281968227436	0.8685716890291104	1.1109746611844822
32.813	1.0075446730124258	0.868909047859161	1.111261644181376
33.11	1.0337790474781798	0.9024096089058432	1.1396496950577937
33.36952048760346	1.0560393087306388	0.9319805905608953	1.1645420030360834
33.39464036570259	1.0582115504391076	0.9348545544738494	1.1669534286864196
33.41976024380173	1.0626923923329474	0.9399071761961062	1.1719139063771202
33.41976024380174	1.0626923923330192	0.9399071761961744	1.1719139063771995
33.42	1.0650617835622656	0.9421483564797614	1.1745301604123795
33.444880121900866	1.311347503542033	1.1750696171260315	1.4464319397101713
33.47	2.2498406296966516	2.060436138498424	2.482624271611956
33.49511987809913	1.3165394955798453	1.181559076081142	1.4521015609782482
33.520239756198265	1.0715941423987758	0.9514893927655277	1.1816169847934666
33.545359634297405	1.0715034036795315	0.9521990062048595	1.1814770755177004
33.57047951239654	1.0737352779639726	0.9550814278494528	1.1838852226382652
33.73	1.0879865858558098	0.9735185421554495	1.1992602545702833
34.04	1.1156970249644156	1.0096149928150595	1.2292071182315665
34.36	1.1436016940785239	1.0471922740720416	1.260173788358445
34.67	1.1716358189903378	1.0839226554306802	1.2902469416334723
34.705497704615375	1.1748286258464762	1.0881622430138425	1.2937058352204787
34.724	1.1764950786640591	1.0903666084317185	1.2955034655614932
34.73162327846153	1.1771821459555976	1.0912693649186411	1.2962395748746254
34.75774885230769	1.1796110937194264	1.0944349673681302	1.2988441900058212
34.783874426153844	1.1897003707141884	1.10482345534816	1.3099066280379204
34.81	1.2214295542834774	1.1356111817395333	1.3448622397940095
34.836125573846154	1.1944525035319797	1.1110684738873944	1.3149979787685648
34.86225114769231	1.189068884633971	1.1068812061603506	1.3089755765784234
34.86225114769232	1.1890688846339716	1.1068812061603517	1.3089755765784241
34.88837672153847	1.1913681887220415	1.109938131798703	1.3114359428861413
34.88837672153848	1.1913681887220424	1.1099381317987038	1.311435942886142
34.91450229538463	1.1937433486085214	1.11306926754336	1.3139798426393043
34.99	1.200624633115099	1.122104510665785	1.321314063418568
35.32	1.2298077466558792	1.1617078271590886	1.3533393218672862
35.65	1.2591203305234633	1.2015835180506698	1.3853882802675854
35.90189521238723	1.2829061343859565	1.2321412938762055	1.4098222858554872
35.928921409290425	1.2854755905537694	1.2354429527507205	1.4124551015448998
35.95594760619362	1.2882370288379306	1.2389003621533614	1.4152786092645742
35.97	1.300050432448537	1.2504728790235664	1.4281991341532307
35.982973803096804	1.310889392396598	1.2611721986146858	1.440144722561829
36.01	1.3898850929373556	1.3366376400883713	1.5273205888022294
36.03702619690319	1.315765658136046	1.2677884572834808	1.4454364468477245
36.064052393806385	1.2979581645914604	1.2520186343312811	1.4257282181520141
36.06405239380639	1.2979581645914609	1.2520186343312822	1.4257282181520148
36.09107859070958	1.300183039997525	1.2551331252483844	1.4281383299426458
36.11810478761277	1.3026005236813172	1.2584321099574092	1.4307609931382297
36.31	1.3198485452813526	1.2818225227121032	1.4493262349702796
36.64	1.3497438067674599	1.3221803544285216	1.4812206797721812
36.745	1.3594358836959266	1.3350362571298837	1.491346153107139
36.98	1.3812891204872564	1.3638530299388258	1.5139819173579916
37.33	1.4123333456108014	1.406781024538769	1.5475580184356106
37.67	1.4435070304510424	1.4485666377584596	1.5800739790600902
38.02	1.47563514470154	1.4915662131019916	1.6133763122909133

Table D.1. Continuation of Table D.1

Beginning of table

$\lambda[\mu m]$	F_ν(DL2014)	F_ν(PL+OTMBB)	F_ν(PL+GMBB)
38.37	1.5071973042173712	1.5344911797106622	1.6464706947428127
38.73	1.5397138878175498	1.5786270338844341	1.680340374694506
38.884	1.5537235521768848	1.5974413480793515	1.6947369381842503
39.08	1.5716646489793473	1.6214184208156113	1.7130390796681183
39.45	1.6045699759773662	1.6664568910198836	1.7473181108456886
39.81	1.6368445807932281	1.7101592307165372	1.7804404168312757
40.0	1.653893524187227	1.7331042052113643	1.7977850586619681
40.18	1.6701383878381724	1.7548440995019126	1.8141803859315506
40.55	1.703561684187478	1.79922264065834	1.8475734750967412
40.93	1.7364837979408416	1.8445662521575608	1.8815651270589289
41.148	1.756361096888629	1.8703865167882257	1.9008758768065386
41.3	1.7702956529644966	1.8883825689650744	1.9143051344046942
41.69	1.8035417322945397	1.9341256932133124	1.94838703896362
42.07	1.8376774596159196	1.9783591402536802	1.9812363567961515
42.46	1.8713120126459066	2.023306870360616	2.0145242403192034
42.85	1.9058362295133404	2.067707991818182	2.0473323619836212
43.25	1.9397945116814084	2.1127887558246967	2.080550481355495
43.543	1.9647382840465029	2.1454328343121505	2.1045609210462537
43.65	1.9738823281801858	2.157304274906068	2.113278550623783
44.06	2.0081645568860407	2.202250793244862	2.1462678213467705
44.46	2.0418808240794695	2.24554857105137	2.177975522859556
44.87	2.076486776001725	2.289270251115802	2.2099402862095454
45.29	2.1105267981518123	2.3332613551014028	2.2420705050005956
45.71	2.1446315448191458	2.3765791536528935	2.2736540559644998
46.078	2.1746747822587658	2.413917723890621	2.3008477819247255
46.13	2.1789305519736017	2.4191269421430337	2.30464406279144
46.56	2.2126637985626325	2.461797455029981	2.3357144193738137
46.99	2.2472219588847424	2.503697021708634	2.3661892974516774
47.42	2.2804539928695964	2.5447411248603213	2.396030148908198
47.86	2.314510956008261	2.5857562985562734	2.42586575634425
48.31	2.347937234073877	2.62681863221204	2.4557213496836803
48.75	2.3814929802330784	2.6660211627217927	2.484234971570992
48.761	2.3822963009876186	2.6669807333861564	2.4849353904782 73
49.2	2.414353452061257	2.7050587658310707	2.512667710597855
49.66	2.4473434336286184	2.7439985472035904	2.5410372116041438
50.12	2.4803981459689948	2.7818908112818717	2.5686761581131767
50.58	2.512757404676036	2.8186569499226897	2.5955559801645367
51.05	2.544421225020205	2.855188841558905	2.6222951064259292
51.52	2.5762145309571363	2.8906218228939555	2.648283116495449
51.599	2.5813347755822864	2.8964281508224183	2.65256189651433
51.64449241881862	2.5842810544215933	2.8997694076387237	2.6550208166306386
51.68336931411397	2.586801223029032	2.902626845581103	2.657123253800103
51.683369314113975	2.5868012230290347	2.9026268455811066	2.657123253800105
51.722246209409306	2.5982074457304134	2.9138596432196566	2.6690357281279913
51.72224620940931	2.598207445730591	2.9138596432198245	2.669035728128187
51.76112310470465	3.5506301051886204	3.812040570329496	3.719956714282956
51.76112310470466	3.550630105189296	3.812040570330133	3.719956714283701
51.8	7.162055574583377	7.21644529367593	7.706776377720641
51.83887689529535	3.558537362055503	3.820456748452437	3.7273174357503174
51.877753790590695	2.6083100628718547	2.925261384124029	2.6774327911003013
51.916630685886034	2.6018748109316197	2.9196197159368107	2.6696173255130526
51.95550758118138	2.604379084075101	2.922403629681786	2.6716708637433886
51.95550758118139	2.6043790840751018	2.9224036296817872	2.671670863743389
52.0	2.6072477693091267	2.925591820572002	2.6740222125100153
52.48	2.638281009712066	2.9594663943705877	2.699007295242512
52.97	2.668618815681708	2.9928658694941053	2.7237208422286154
53.46	2.6982611695650474	3.0250103308535095	2.7476189866454135
53.95	2.7279034990525486	3.0560170941028004	2.7707467074828096

Table D.1. Continuation of Table D.1

Beginning of table

$\lambda[\mu m]$	F_ν(DL2014)	F_ν(PL+OTMBB)	F_ν(PL+GMBB)
54.45	2.7567208783746335	3.0864497772365205	2.7935464289581455
54.603	2.7653643957281715	3.095474701853549	2.8003504186377723
54.95	2.784842898788751	3.115606553435227	2.815529191827085
55.46	2.8129001997396257	3.1441475098303444	2.8371485508350394
55.98	2.8394371268424803	3.1719777154599442	2.858357277866999
56.49	2.8659092587883794	3.1979866452974455	2.8783406494942496
57.02	2.8923813998993797	3.223768367830644	2.898278061432585
57.03825118302342	2.8932638731051887	3.2246367450931412	2.8989500070961842
57.08118838726757	2.8953377363644477	3.2266765523413707	2.9005275474501544
57.081188387267574	2.8953377363644477	3.226676552341372	2.9005275474501544
57.12412559151171	2.898233872799194	3.2294836375806524	2.9030111954297073
57.124125591511714	2.898233872799209	3.229483637580666	2.903011195429724
57.167062795755854	2.9885724092413266	3.3146809256473633	3.0020392289350517
57.21	3.326000757748234	3.6327693952400932	3.3738868056062903
57.25293720424415	2.9929621124828567	3.3189124932271454	3.005446655690554
57.252937204244155	2.992962112482843	3.318912493227132	3.0054466556905375
57.295874408488295	2.9064824749021088	3.2374464621659347	2.9092399670137317
57.338811612732435	2.907703137375619	3.2386401703557954	2.9098651609087725
57.381748816976575	2.909750998019316	3.2406119996981717	2.911402539251711
57.38174881697658	2.909750998019317	3.2406119996981713	2.9114025392517116
57.54	2.917268377152138	3.247817740679351	2.9170240717503924
57.782	2.928438593604481	3.2585615657230207	2.925474277339764
58.08	2.942025916026273	3.2714548627292825	2.9356476391303428
58.61	2.966023288080562	3.293421642903743	2.953107595711561
59.16	2.9891309757741813	3.314924491067168	2.9703813067083336
59.7	3.011413685723719	3.3347453613022147	2.986525245376185
60.0	3.022833869627813	3.345243660196204	2.995141985424619
60.26	3.0325476870281256	3.3540230486610922	3.0024181908561878
60.81	3.054199706932453	3.3717011542353825	3.017203177092459
61.145	3.0657566973574717	3.381859530171892	3.025822794086201
61.38	3.073683847266279	3.3887171523341366	3.031700198777989
61.94	3.0931680153903964	3.404196410674762	3.045114297322599
62.52	3.111892012904835	3.418955096191708	3.0581646162829497
62.98035880495699	3.1251136801543664	3.4297654260639936	3.0679399964541063
62.980358804957	3.1251136801543673	3.429765426063994	3.067939996454107
63.027769103717745	3.126440064218981	3.4308347336578056	3.0689227035100575
63.02776910371775	3.1264400642189814	3.4308347336578056	3.0689227035100575
63.0751794024785	3.127796220946889	3.4319299125077123	3.0699381343101115
63.1	3.130520087464073	3.4344005632057186	3.072693278989121
63.12258970123925	3.1330631922641667	3.4366497582092355	3.0752020789725125
63.17	3.149284682635417	3.4516271333163164	3.0924845660285283
63.21741029876075	3.1359460592793393	3.438740262290685	3.077128088280058
63.2648205975215	3.133469570380644	3.4360888401599152	3.073764294732251
63.264820597521506	3.1334695703806448	3.436088840159916	3.0737642947322508
63.31223089628226	3.1348527562570667	3.437072745534996	3.074661519163616
63.359641195043004	3.1362662633188094	3.438082768536826	3.075592297643434
63.68	3.1456516469478855	3.444707504499125	3.0818133768108082
64.27	3.161447482655869	3.4559440844549285	3.092590534908159
64.705	3.1731915567366737	3.4634544931120463	3.1000256958283408
64.86	3.177243322957474	3.465986678278511	3.102594316812332
65.46	3.1908712988262224	3.4749857798399857	3.111935751312321
66.07	3.203739088294088	3.48291777950637	3.120601975854359
66.68	3.2158466750371124	3.4896999886067643	3.1285094237810944
67.3	3.2265465097609107	3.4953998285995023	3.1357118619982747
67.92	3.2378938897186496	3.4999420078514665	3.1421068533070105
68.472	3.24544245935847	3.503091150110064	3.147193700651981
68.55	3.2464257784460666	3.503474570121389	3.147872288486548
69.18	3.2556052892601226	3.5058733666657873	3.1528258688165636

Table D.1. Continuation of Table D.1

Beginning of table			
$\lambda[\mu m]$	F_ν(DL2014)	F_ν(PL+OTMBB)	F_ν(PL+GMBB)
69.82	3.2626168658712644	3.5071980750330938	3.157060403487827
70.47	3.2689808759870447	3.5075323120106687	3.160655841849954
71.12	3.2752322484970176	3.506773020632842	3.1634454522341873
71.78	3.2794283047892643	3.5049402413509116	3.16549263039284
72.44	3.28351172290785	3.502194310519959	3.166876975706858
72.458	3.2836040917549267	3.5021065942435476	3.1669052329146568
73.11	3.286187464678366	3.4983740523196847	3.1674964292037653
73.79	3.2874554588151024	3.4934890362393562	3.1673521855970783
74.47	3.288610816621775	3.487778335418922	3.1665801097035513
75.16	3.2877108594148305	3.4810083577933035	3.165026309277546
75.86	3.286810899456723	3.4731979632626624	3.162697598105061
76.56	3.2843905535991014	3.4646521894726625	3.1597772174794376
76.676	3.2840115021726324	3.463147823143745	3.159220967015762
77.27	3.2813226983171497	3.455073421785218	3.1560651998524247
77.98	3.277494654729431	3.444637181602952	3.1516372173406118
78.7	3.272258861475689	3.4334277723315934	3.1466076203477416
79.43	3.26626288229605	3.421221326195262	3.1407833151164244
80.0	3.2618132549300385	3.4111881750411697	3.1357921565621774
80.17	3.2602668988553507	3.4080452840230553	3.1341756020536873
80.91	3.251455395140615	3.394333933538386	3.1270674373906093
81.14	3.249159901765652	3.389883946104681	3.1246920042499844
81.66	3.2432914957084913	3.3796700886488096	3.119168501031777
82.41	3.2337198518153563	3.364290487855638	3.1106079606704675
83.18	3.2235006563585364	3.348072275920242	3.1013720215158775
83.95	3.2125212613789356	3.33115329400932	3.0914671153763664
84.72	3.200781666918236	3.3135953863369583	3.080936191536145
85.51	3.1883945190334844	3.295256570389305	3.0697404285085432
85.863	3.1824925826285027	3.286747714181738	3.0644461516152264
86.3	3.1745996372213354	3.276296042748575	3.057915233153818
87.1	3.160044594963329	3.256525750881487	3.0453445727566537
87.9	3.1454895385219506	3.236526403864775	3.032438970543451
88.06482655124033	3.1425867625643353	3.2323362438970085	3.0297060246386267
88.06482655124034	3.1425867625643353	3.232336243897007	3.0297060246386263
88.13111991343024	3.1414017724213488	3.2306297853424204	3.0285911350967063
88.19741327562018	3.158077531667425	3.2457551536973037	3.0471990163378684
88.19741327562019	3.158077531667843	3.245755153697698	3.04719901633833
88.26370663781009	5.067414849004426	5.044792328478824	5.155564261858417
88.2637066378101	5.067414849006017	5.044792328480325	5.155564261860173
88.33	12.324812572170227	11.88466371788531	13.16896390741692
88.39629336218991	5.0707281648511575	5.046901527872379	5.15976776856597
88.46258672437983	3.1532157615204532	3.2390844598310786	3.0428739217442264
88.52888008656976	3.133947479535505	3.220441359070052	3.02190164652343
88.59517344875967	3.1326474291896305	3.2187317416000685	3.02077112289283
88.72	3.130174309765373	3.2154825068190425	3.0186210722077
89.54	3.1135639374840536	3.1939407334913046	3.004245248421198
90.36	3.09760111482806	3.1722692453232986	2.9895968951972445
90.862	3.087488358121514	3.158704593748059	2.9803118715248864
91.2	3.0802305737753874	3.149605377210562	2.974050302362143
92.04	3.062099863980153	3.1265036460705464	2.9579796348115877
92.9	3.0433216018698612	3.1028327674510052	2.9413238115869103
93.76	3.023895761338858	3.078758609524992	2.9241620383148206
94.62	3.0043572869265587	3.054323295855479	2.9065274500253535
95.5	2.9834110745100895	3.0293922159135653	2.888347166474684
96.151	2.967657547358089	3.0107214253749026	2.8745934598142133
96.38	2.961817294548396	3.0041356256416107	2.86971603194849
97.27	2.940223545828825	2.9782916854572985	2.8504401436693105
98.17	2.9186297963322265	2.9523126456637714	2.8308761436006606
99.08	2.8956282970690532	2.9257916992266946	2.8106956884785985

Table D.1. Continuation of Table D.1

Beginning of table			
$\lambda[\mu m]$	F_ν(DL2014)	F_ν(PL+OTMBB)	F_ν(PL+GMBB)
100.0	2.871899794777506	2.8987698311505166	2.7899388972397112
100.9	2.8482509290236755	2.872533047129863	2.7695933841774107
100.92621909870483	2.8476442740689585	2.871773478381206	2.769001789232992
101.749	2.827695892129468	2.8476431294271185	2.750120584421581
101.86101701559753	2.824842713457005	2.8443348204180916	2.74751958394604
101.9	2.8238420150727066	2.8431752286437812	2.746607038504022
102.8	2.7994329746604305	2.8166045621858706	2.7256099554974225
102.80447320933098	2.7993293665208783	2.816468804626932	2.725502140791563
103.75666787451848	2.7761339722055887	2.7886576988232568	2.70334241415636
103.8	2.775024067183075	2.78739707160732	2.7023335187656934
104.7	2.749967437146378	2.760982496646556	2.6811011049651086
104.71768194855203	2.7495454947023554	2.760458725305474	2.6806783199905833
105.68759711848051	2.7252366765116576	2.7318864942637284	2.65752041471617
105.7	2.724910937215508	2.731535230220183	2.657234729858096
106.66649582795388	2.700732666573163	2.7034307141014646	2.634273809713007
106.7	2.6998544228359616	2.702462137530662	2.6334793176483586
107.6	2.6740375707372315	2.6762375305470094	2.611885965526453
107.65446128423159	2.6726972094743995	2.674639475447456	2.610565064932225
107.672	2.672264107379238	2.674123273868937	2.6101382586823303
108.6	2.6483334976620805	2.6470677538336087	2.587688730381337
108.65157746525372	2.647024621951013	2.645527011319336	2.586405345870602
109.6	2.621869229920112	2.618236917519213	2.563593527536167
109.65792912678099	2.6205799703630284	2.616588162289224	2.5622102658805193
110.67360180959746	2.596812519983463	2.5873639459917754	2.537596215118048
110.7	2.59616527206062	2.5865973166442573	2.536948119937409
111.69868184678226	2.5704964810018067	2.5578680453880027	2.512574706728836
111.7	2.5704611615350084	2.557831654597138	2.512543725785041
112.7	2.5433492899327876	2.5295298714674117	2.4883687534559265
112.73325637104871	2.5426077213449116	2.528598412494089	2.4875703473843065
113.77741332214902	2.5181975933790905	2.4990909565114636	2.4621905945429154
113.8	2.5176452889213228	2.4984474132905565	2.4616352087313866
113.94	2.514080561884231	2.4944339378971234	2.458169924454985
114.8	2.491293600981909	2.470259832505532	2.437229683139579
114.83124145435112	2.490616868504689	2.4693588119020036	2.436447240307095
115.89483034398118	2.4664724216912224	2.439900943972517	2.4107721073634 56
115.9	2.466349789572953	2.4397590905452398	2.410648062245558
116.9	2.439998082202881	2.4121435904015747	2.3864306323443087
116.96827039703847	2.438474706224246	2.4102501029006356	2.3847651016753186
118.0	2.414406680549163	2.3818705251610637	2.359722579989104
118.05165285688055	2.413253873380714	2.3804187351318524	2.3584380536522196
119.1	2.3888152655178017	2.35210723989937	2.3332992373942543
119.14506981197748	2.3878087765371787	2.3509050092472776	2.332228398979511
120.0	2.368036705701721	2.3279049795922435	2.311696699951885
120.2	2.3632238350713863	2.3225525494809585	2.3069051463098726
120.24861420374123	2.3621982704019735	2.3212402926017326	2.3057298276818607
120.573	2.35525305896661	2.3124527199032037	2.2978524216680767
121.3	2.339040148782856	2.2931386107321523	2.2804868823537845
121.33464724652947	2.3383557861103164	2.2921940395990292	2.279636421960174
121.36237983442417	2.337806618665048	2.2914363961311937	2.278954189695336
121.4259854348971	2.3365424204118437	2.289803046856629	2.277481412834328
121.42598543489711	2.3365424204118437	2.2898030468566284	2.2774814128343275
121.51732362326473	2.334737436854125	2.2874654875461915	2.275378582779528
121.60866181163236	2.3352260869334	2.2872875652156672	2.2758089316735965
121.7	2.342220276622244	2.2932391788637463	2.2834229766322043
121.79133818836763	2.3315123959992867	2.282503617718721	2.271492231372263
121.79133818836765	2.3315123959992854	2.28250361771872	2.271492231372262
121.88267637673526	2.3272960151418935	2.277884354191844	2.2667296826235277
121.88267637673528	2.3272960151418935	2.277884354191844	2.2667296826235277

Table D.1. Continuation of Table D.1

Beginning of table			
$\lambda[\mu m]$	F_ν(DL2014)	F_ν(PL+OTMBB)	F_ν(PL+GMBB)
121.9740145651029	2.325380000392842	2.2754310628737424	2.2645077510665526
122.06535275347053	2.323472390074124	2.2729834692089663	2.262295801053031
122.48646137509307	2.3145022091632663	2.261988887969871	2.252342790268411
122.5	2.314209024716114	2.2616378938759287	2.2520246687624663
123.6	2.289377758255	2.2329779109085264	2.225984087059327
123.62095437367691	2.288937165801552	2.232429487404717	2.225484539360818
124.7	2.2653066643785538	2.204510361146805	2.1999846774009173
124.76595526308684	2.2640746230614526	2.202769283845771	2.198391124801283
125.9	2.2418832491455016	2.174039145735583	2.1720029760615622
125.9215613694151	2.241494203211327	2.173499645188789	2.1715060844825347
127.08787092020596	2.219459430696998	2.144154263236583	2.144414988505632
127.1	2.2192200044896886	2.1438475661217304	2.144131193897688
127.592	2.209301366255013	2.1315515612156246	2.1327388828038303
128.2	2.1965566352831343	2.116397331794881	2.118666298412422
128.26498305280597	2.19542046238812	2.1147435212294035	2.1171293007701104
129.4	2.1746535749911855	2.087028809539482	2.091285884911917
129.4529978227916	2.1737595332815824	2.0857531207546067	2.090093194125313
130.6	2.1535106865014617	2.057982787463109	2.064075721973044
130.652016212472	2.152600073722537	2.056720184878696	2.0628902754552225
131.8	2.1316076014271452	2.02917406276614	2.0369643133322914
131.86214013947486	2.1305571262609275	2.0276543491477343	2.0355316584086975
133.0	2.110464688395028	2.000961163122442	2.0102874535884623
133.0834724654076	2.1091266635903057	1.999034338710427	2.0084606327008316
134.3	2.088674319593543	1.9707775946261268	1.981617648268549
134.31611700460155	2.0883817783981877	1.9704020844150958	1.981260235818409
135.02	2.0752915417993782	1.9542505776318737	1.9658632205312352
135.5	2.06601102154988	1.9431764116284913	1.9552880982237522
135.5601785329369	2.064946850630065	1.941766527628732	1.9539412190515346
136.8	2.0420527167783473	1.9139470653811292	1.927279597269806
136.81576279674707	2.0417214346711297	1.9135981824194979	1.9269444699383838
138.0	2.0159263467344375	1.8872898557136184	1.9016320227826653
138.08297652180923	2.0141428704378623	1.8854450795128308	1.8998538525555122
139.3	1.9869845871627834	1.858701122787877	1.8740198292246748
139.36192742241437	1.985551880542488	1.8573153754134704	1.8726795782744536
140.0	1.9705036926888424	1.8436726714814875	1.859454382096889
140.6	1.9558748798259733	1.8307828018226477	1.8469403370500002
140.65272421052364	1.9545681429757726	1.8296703830819911	1.8458588236588478
141.9	1.9225972245023235	1.80324214473236	1.8201252827100969
141.95547660501015	1.9211622053498767	1.8020653122580643	1.8189775148663927
142.88	1.8966556095967868	1.7827560165283038	1.8001136364740364
143.2	1.8879118129991068	1.7760057581456303	1.7935109696790152
143.27029534098293	1.8859823859200868	1.774507654622447	1.7920453966246292
144.5	1.8511710914219246	1.749399946198156	1.767413043379823
144.59729217920196	1.8487407037675823	1.7474485332972987	1.7654945633959531
145.06319781733802	1.8369415289866753	1.7379647770050652	1.7561690646484567
145.1723983630035	1.8341374405129827	1.7357085995215393	1.7539501136228228
145.28159890866903	1.831326917251074	1.7334687419268502	1.7517478958484154
145.28159890866905	1.8313269172510733	1.7334687419268502	1.7517478958484154
145.3907994543345	1.8293751271226877	1.7321615631524585	1.7506139705028225
145.5	1.8298766555873145	1.7331683174694807	1.752192827062191
145.6092005456655	1.8236666624031017	1.7278507525611477	1.7463652426359046
145.71840109133097	1.819904648323067	1.7248420915770935	1.7432445542581518
145.8276016369965	1.8170038680294478	1.7226467609249916	1.74107878453492
145.9	1.8150780389869563	1.7211896593855092	1.7396421875833632
145.93657991557578	1.814057911731342	1.7204513776791706	1.7389142711754486
145.93680218266198	1.814051708011738	1.720446887482922	1.7389098439716493
147.2	1.77777137776332	1.6953097265190624	1.7140801997742456

Table D.1. Continuation of Table D.1

Beginning of table			
$\lambda[\mu m]$	F_ν(DL2014)	F_ν(PL+OTMBB)	F_ν(PL+GMBB)
147.28827239075017	1.775586821830467	1.693522990629322	1.7123137070526102
148.6	1.7420499447228313	1.6681040987407059	1.687112584666423
148.6524844997857	1.740728052020541	1.6671035061424517	1.6861186821470038
150.0	1.7056978274965384	1.6413271744140054	1.6604823357426228
150.02933220192168	1.7049928975041055	1.6407654816576553	1.6599229613829853
151.198	1.6761364318467633	1.6187406793026693	1.6379536374938806
151.4	1.670995581546783	1.6148789337184386	1.634098418277913
151.4189325304352	1.6705429686143285	1.6145150482505373	1.6337351361560917
152.8	1.6364876079038115	1.589167524434709	1.6083615614009643
152.82140360258708	1.6359898932332428	1.5887807366727047	1.6079737089835566
154.2	1.6029340760943112	1.563812983356591	1.5829093739487126
154.23686462966273	1.602100697480855	1.5631449623127203	1.5822379794515422
155.6	1.5703349862509393	1.538801429459506	1.5577327759325972
155.66543592710622	1.5688598454908558	1.5376132182263558	1.5565359300131218
157.0	1.537865397804782	1.5144296108421595	1.5331264175949315
157.10723892474488	1.5356838803643813	1.512601813074055	1.5312776931388716
157.12687268737096	1.53528336774614	1.5122661726676634	1.5309382095533126
157.2451545155282	1.532863341934496	1.5102376894420846	1.5288865134536265
157.3634363436855	1.5306923877165932	1.508444505185907	1.5271122517875062
157.48171817184274	1.5562053724791753	1.5327451568432915	1.555907245284834
157.6	1.6599668328093442	1.6307988842732681	1.6711016092459805
157.71828182815725	1.5513622905942226	1.528689107299026	1.55181751286103
157.8365636563145	1.5208380769699523	1.5001777386851487	1.5187508802164322
157.9548454844718	1.5180794316491808	1.4979654354359744	1.516469486391268
158.07312731262905	1.5155713361514225	1.4959902234287896	1.514467565127204
158.5	1.5064151165238415	1.4887709740560624	1.5071508058397016
158.56239617711373	1.5051514980324892	1.4877037509066764	1.506069175492853
160.0	1.4750943352323502	1.4634561386527472	1.4814581931007313
160.03103137387018	1.474439883605701	1.4629238994746996	1.4809177181082338
161.4	1.4447278856436283	1.4404865662256452	1.4580802357749465
161.51326935030895	1.4425655782047446	1.4386659430285018	1.4562242543899833
162.9	1.4152512287142684	1.4162931388171502	1.4333986466818658
163.0092360979741	1.4131787144502845	1.4145339624666295	1.4316021227618372
164.4	1.3859688293097006	1.3924520622186618	1.4090219530002461
164.5190587753661	1.3839156707858309	1.3905322886948706	1.4070580846267973
165.959	1.358264142477074	1.3683213121273794	1.3842866186458338
166.0	1.3575114628771505	1.367701145031536	1.3836499119931895
166.04286571875295	1.3567268944316402	1.3670515704240056	1.3829830222253618
167.5	1.3292482355622255	1.344932171992382	1.3602578609902327
167.58078645307688	1.3278147267424747	1.3437074918953407	1.3589986029727392
169.0	1.301874694077822	1.3225188512124906	1.3371859172207239
169.1329517029647	1.2996759766213417	1.3205038350542324	1.3351109581283633
169.824	1.2880580000896868	1.3105185865300157	1.3248099419380597
170.6	1.2746307715338245	1.299232853473765	1.3131621063769352
170.6994934038408	1.2729933411222552	1.2978180239440735	1.3117003214546774
172.2	1.24751636630272	1.2764242266590808	1.2895835109633182
172.28054471313922	1.2462312426446192	1.2752776684541407	1.2883973670863582
173.78	1.2215654435573389	1.2542560051101244	1.2666266301948488
173.8	1.221226888719091	1.2539717463152984	1.2663321878199594
173.87624002162505	1.2200509193197686	1.2528860443844458	1.2652076153593177
175.4	1.1958157997763847	1.232163945557148	1.2437019373078797
175.4867149648152	1.1944806185005743	1.2310070852716626	1.242499965588319
177.0	1.170469455136789	1.2107756613522942	1.221469781703125
177.1121064345087	1.168771341040403	1.209280668158671	1.2199148113292098
177.828	1.1577592803643688	1.1998409420468303	1.210090691882295
178.6	1.145556699032507	1.189741941987124	1.1995731298690298
178.75255259042356	1.1434226980174849	1.1877096436892167	1.1974571310902693
180.3	1.1210776306435197	1.1679953508510563	1.1768945947131106

Table D.1. Continuation of Table D.1

Beginning of table			
$\lambda[\mu m]$	F_ν(DL2014)	F_ν(PL+OTMBB)	F_ν(PL+GMBB)
180.40819287193807	1.1195827576283368	1.1666444195501258	1.1754840804915712
181.97	1.097331156509757	1.1470997975777442	1.1550700896881962
182.0	1.0968913599314825	1.1467259384098158	1.1546793960439916
182.07916800994624	1.0958207144933712	1.1457372744824743	1.1536462488373722
183.7	1.0732146488213563	1.1258096509191902	1.132804595278979
183.76562003881722	1.0723404383768256	1.1249905694881523	1.1319479763406135
185.4	1.0498954928904756	1.1055320049246464	1.1115634956278524
185.46769230846976	1.0490100438657444	1.1047412196612771	1.1107343573065602
186.209	1.0391735280557661	1.0959475220456918	1.1015166630869566
187.1	1.0270099250732325	1.0856519852836706	1.0907136918834572
187.18552949655793	1.025908377408941	1.08465407829542	1.0896666984600292
188.8	1.0044931876136203	1.066120243071118	1.0702071508735045
188.91927762076642	1.0029798773974477	1.0647311236340555	1.0687488104887521
190.5	0.9823340055487041	1.047136031689305	1.0502498061374697
190.546	0.9817937219464742	1.0466365033303713	1.0497241474416288
190.66908405122518	0.9803438165272927	1.0452957298544605	1.048313328124586
192.3	0.9605437026661922	1.0274946287557178	1.0295793591799585
192.43509752303325	0.9589798812186274	1.0260253084659012	1.0280325712290757
194.1	0.93911095328976	1.0081973915947908	1.0092535570083625
194.21746814890244	0.9377785829037235	1.0069215066194788	1.0079098691373385
194.984	0.9289541925309939	0.9990002095376473	0.9995560990076983
195.9	0.9181117898583923	0.9894758356015939	0.9895121076393266
196.01634743191858	0.9168099764895101	0.9882943459940956	0.9882652938464529
197.7	0.897405437066142	0.9711703692630022	0.970193336592743
197.83188827841622	0.8959597393313563	0.9698338387756056	0.9687825346048135
199.5	0.8771326572507394	0.9532013302735367	0.9512171028260479
199.526	0.8768673399267976	0.9529391633749255	0.9509402893091586
199.66424501097933	0.875452803096201	0.9515412744226669	0.9494643995452718
201.4	0.8571414726103378	0.9347869640066355	0.9317536659062942
201.51357338155586	0.8559358363504833	0.9337133682499332	0.9306181479420881
203.2	0.8375190170176399	0.9177488481964976	0.9137332573907346
203.38003058469798	0.835742718183928	0.9160527146290899	0.9119391116640254
204.174	0.8277865729855587	0.9086482583570549	0.904104894280881
204.78337341361672	0.8215443983045618	0.9030527560522308	0.8981824293705278
204.93753006021254	0.8199465192657921	0.9016190046501497	0.8966653890986416
204.93753006021257	0.8199465192657918	0.9016190046501495	0.896665389098641
205.09168670680833	0.8183565220709474	0.9001924622708154	0.8951578259343197
205.09168670680836	0.8183565220709474	0.9001924622708155	0.8951578259343199
205.1	0.8183588399307853	0.9001985287647479	0.8951737817460568
205.24584335340415	0.8185133308502078	0.9003036725994032	0.8954526868970799
205.2458433534042	0.8185133308502088	0.9003036725994041	0.8954526868970811
205.26377527092524	0.8190697259760373	0.9008230879175532	0.8960803647224774
205.4	0.8233016614383512	0.9048555207233371	0.9009391812409728
205.55415664659583	0.8155136469385794	0.897564111691276	0.8925514721612493
205.70831329319165	0.8123406344588058	0.8946222514646883	0.8892600132987846
205.86246993978747	0.8108045132896677	0.8932229427826831	0.8877765669162665
206.0166265863833	0.8092766766540143	0.891831153584293	0.8863029308080753
206.01662658638332	0.8092766766538975	0.8918311535841829	0.8863029308079463
207.0	0.7993583606642332	0.8829684213719055	0.8769189538881255
207.1649675602067	0.7977847382936084	0.8815200248448969	0.875384461222256
208.9	0.780744029629149	0.8662554098907714	0.8592145753927803
208.93	0.7804795199768959	0.8659934369935486	0.8589370383474328
209.08376905557498	0.7791198490425748	0.8646466245388518	0.8575103250153084
210.9	0.762563336601287	0.8489924434264833	0.8409229906196174
211.02034285685966	0.7614601007288136	0.8479408607822354	0.839809199553369
212.8	0.7446753553821845	0.8330988126764785	0.8240743139376803
212.97485357455187	0.7431776840270428	0.8316736464499626	0.82256284164805
213.796	0.7360379923500083	0.8248728428553227	0.8153534206041089

Table D.1. Continuation of Table D.1

Beginning of table

$\lambda[\mu m]$	F_ν(DL2014)	F_ν(PL+OTMBB)	F_ν(PL+GMBB)
214.8	0.7270690130711056	0.8167711338078887	0.8067612363638423
214.94746734379805	0.7258324173542962	0.8155722483703779	0.8054901181404202
216.8	0.7098315012398279	0.8007584236975482	0.7897810132544886
216.93835183851823	0.7086951318849619	0.7996371341115864	0.7885925458406733
218.776	0.6931598979357606	0.7854243467702612	0.7735160766669931
218.8	0.6929515464585502	0.7852433487108795	0.773324014966373
218.94767628566208	0.6917581651588115	0.7841266506507371	0.7721391544977182
220.8	0.6763531053944353	0.7701030140945804	0.7572636612539085
220.97561147959033	0.6749644747640113	0.7687800852935883	0.7558605879284922
222.8	0.6601234841684362	0.7552654198840694	0.7415259568123753
223.02232979659362	0.6584795717829268	0.7535977219644331	0.7397580389601821
223.872	0.652100176643532	0.7475334453156083	0.7333236426768599
224.9	0.644175486949383	0.7401417646627522	0.7254842981418442
225.0880052095462	0.6428110175649145	0.7388256934741634	0.7240880062747336
227.0	0.6285202898862284	0.7254206653848398	0.7098711644818114
227.17281330269074	0.6272945490859341	0.7242151185306305	0.7085929179226009
229.087	0.6133200607133726	0.7110855160493347	0.6946717475152124
229.1	0.6132226502915383	0.7109954384084402	0.6945762902304229
229.2769312865649	0.6119911792147521	0.7097660866286779	0.6932736334593389
231.2	0.5982178308131564	0.697011518742778	0.6797512585699849
231.40053801306541	0.5968472844965086	0.6957128165581308	0.6783742778384975
233.3	0.5834945504899378	0.6833896584940256	0.6653141252465641
233.5438139906477	0.5819522570849427	0.6818179892865297	0.6636489580675774
234.423	0.5763054025492645	0.6762023973637318	0.65769958917539
235.5	0.5692049177366697	0.669410545935712	0.6505051772529913
235.70694139967276	0.5679087874556185	0.6680815218857407	0.649098230844306
237.7	0.5550560363450804	0.6558641895462409	0.6361593713045492
237.89010410788958	0.5539017869390114	0.6547260350173121	0.6349540441744866
239.883	0.5414497268413642	0.6427799256616328	0.622309323969637
239.9	0.541340730776886	0.6426788873364313	0.6222024088902384
240.09348768606517	0.5401596227866151	0.6415255371448455	0.6209821002590085
242.1	0.5275606763462269	0.6297686586717555	0.6085451084043474
242.31727942376008	0.5262605682213521	0.6284798048749288	0.6071826959926239
244.3	0.5140621609835082	0.6172454523788762	0.5953038611300078
244.56166834524439	0.5125896081308796	0.6158002451524783	0.5937758994682765
245.471	0.5073956413078294	0.610696686731126	0.5883831769685259
246.6	0.5007804976832472	0.6045195204504858	0.5818564727675327
246.82684522556923	0.4995247861788771	0.6032718295462624	0.5805387540063385
248.9	0.4877156047972655	0.5920602737146685	0.5687014859322979
249.1130026067791	0.4865360629544829	0.5908941748309815	0.5674712803425351
251.189	0.47471491415837264	0.5800470912431631	0.5560259871987104
251.2	0.47465070095478346	0.5799911846247904	0.5559670034684836
251.42033481427967	0.47342978292970705	0.5788678967533353	0.5547820271429506
253.5	0.4615857849380713	0.5682515294404129	0.5435898602730075
253.74903797335716	0.4603018308752512	0.5669886080978254	0.5422591566657844
255.9	0.4488897660465753	0.5562620413796384	0.5309613918435243
256.0993100258457	0.4478454220423222	0.555255821100692	0.5299024850666068
257.04	0.4428503457773681	0.5507453752376769	0.5251536376487004
258.2	0.43653997245585124	0.5451339185548837	0.5192499512818115
258.4713507469564	0.4352029748643151	0.5438597231348106	0.5179093496565844
260.6000000000001	0.424418308597835	0.5338459364675615	0.5073813456228762
260.8653617622551	0.4231396132599622	0.5326062040245826	0.5060787427903568
263.0	0.41256692140026796	0.5228027070747695	0.49578280644571926
263.027	0.4124463876223504	0.5226776673017862	0.4956515865063651
263.281546564802	0.41130633778185044	0.5214947016724047	0.4944103185017906
265.5	0.40108440896302794	0.5116577084469104	0.4840893414135892
265.7201105324507	0.4000760332024629	0.5107052725170199	0.4830904503659206

Table D.1. Continuation of Table D.1

Beginning of table			
$\lambda[\mu m]$	F_ν(DL2014)	F_ν(PL+OTMBB)	F_ν(PL+GMBB)
267.9	0.3898186030049148	0.5012633449462124	0.47319548049799687
268.1812609453013	0.3886130683772376	0.5000538277474289	0.4719287829032015
269.153	0.38438916338556584	0.49591018525747305	0.4675904334463782
270.4	0.3788344186165407	0.4906740089699294	0.4621109476451922
270.6652070033241	0.3777346091401302	0.4895397495258546	0.460924836978223
272.9	0.3682077988320573	0.48041627796842923	0.4513860779084721
273.1721598441379	0.367109834876147	0.4793334061859296	0.45025445509493617
275.4	0.3578739797208842	0.47045597030073744	0.4409850732630005
275.423	0.3577868640586111	0.4703653123441136	0.44089046992773134
275.70233256095827	0.35672535190852783	0.4692603075448936	0.43973754516299485
278.0	0.3477457347523265	0.4603265112130297	0.4304221859596842
278.25594022071255	0.3467701823086432	0.45931972701278956	0.4293734398985621
280.5	0.33798623559948443	0.4508907596320281	0.42059559079512226
280.833199882317	0.33679100380066396	0.44967278339758954	0.4193278917362178
281.838	0.33313490047043803	0.44594163978415263	0.4154469287706153
283.1	0.3284323288689355	0.44136912301618236	0.410693082164814
283.43433061513093	0.32730482514690756	0.4401542617900213	0.40943078560022056
285.8	0.3190952753373235	0.4317015432658968	0.40065441199233276
286.0595535175745	0.3182129213861182	0.4307633682131869	0.39968132146892454
288.4	0.31003968844242047	0.4226905652563343	0.3913112930356635
288.403	0.3100302208042872	0.4226805234081609	0.3913008865502848
288.7090917359235	0.3090611247788026	0.4216523287454361	0.39023551882423646
291.1	0.3012769861903445	0.413610395978985	0.3819108312137016
291.3831704832789	0.30039476394755515	0.41266479986313154	0.3809328460417734
293.8	0.29265504738719944	0.4047357505230102	0.37273848750207766
294.08201705870607	0.29181269311031016	0.4037999665872225	0.3717724313909785
295.121	0.28866745776034036	0.40052704509380904	0.36839345832423304
296.5	0.2843906565735824	0.3961446733859593	0.36387340910195254
296.80586086656024	0.28348487058364197	0.3952015267491634	0.3629009380891479
299.2	0.2762022646589659	0.38780856447816436	0.3552856307546914
299.55493343598164	0.27522408695683753	0.3867216520573216	0.3541670686537827
301.995	0.26830998961996355	0.3793772707819177	0.3466152335279644
302.0	0.26829548081082133	0.37936210969327067	0.34659965920169356
302.3294684405776	0.2674198234173036	0.378359520365013	0.345569902209465
304.8	0.2606702332040651	0.3711830299817262	0.3382034172521044
305.1297017182871	0.25980230162849555	0.37025067502519	0.3372471425477155
307.6	0.25312099281598016	0.3632549523185391	0.3300794367752446
307.95587129142234	0.2522600493342754	0.3622554796795312	0.3290564050178019
309.03	0.24962494301114732	0.3592604383489879	0.32599218130623425
310.5	0.24592938308643814	0.35523330790919955	0.3218753724323869
310.8082173869064	0.2451643266978075	0.3543731149770575	0.3209967372415829
313.3	0.23881371780987973	0.34773388433908486	0.31421974406011094
313.68698245668793	0.2379132354748148	0.3467313270677413	0.3131972691543732
316.2	0.23190364054105223	0.34020798725837537	0.3065516778188232
316.228	0.23184289813413922	0.3401362109532938	0.306478620389656
316.59241119835207	0.23104941802625198	0.3391983052245063	0.30552414791032695
319.2	0.2252103950420852	0.33260351067055166	0.29881948698224836
319.52475057592136	0.22450216596315625	0.33177317333350914	0.29797632540640423
322.1	0.2187338647777695	0.32548829026046927	0.29159931313871534
322.4842498408439	0.21794164321355777	0.32457630774884905	0.2906748323565064
323.594	0.2156219005352494	0.3219023476487652	0.2879660693244112
325.1	0.21239816329675287	0.31835828055094695	0.2843788763158564
325.4711605531848	0.21165902522178995	0.3174834026114907	0.28349401180214284
328.1	0.2062792427670856	0.31139615131115916	0.27734359972851913
328.4857366030047	0.20552839796079053	0.3104935546856649	0.2764327597401309
331.1	0.2003010858503392	0.3046501697890223	0.2705411680880661
331.131	0.2002442927242565	0.30458310332354105	0.2704736041234342

Table D.1. Continuation of Table D.1

Beginning of table			
$\lambda[\mu m]$	F_ν(DL2014)	F_ν(PL+OTMBB)	F_ν(PL+GMBB)
331.52823423194235	0.1995137549155991	0.3037200945434313	0.26960436703383905
334.2	0.1944637668377588	0.2979062645171934	0.26375555679167617
334.59891205499747	0.19375760753770865	0.29704582929094064	0.2628909461698056
337.3	0.18884322952416321	0.2913221146982515	0.25714575161134345
337.6980310825088	0.18815604792778198	0.29046986488430576	0.25629138443122873
338.844	0.1861506488412259	0.2881409260271701	0.2539574253152642
340.4	0.18336344818233816	0.28494510245250404	0.25075825899188237
340.82585474234514	0.1826614299716487	0.2840988452544707	0.24991163824199097
343.6	0.17795972991370781	0.2785774566634893	0.24439478603310663
343.98264890229285	0.17734198480036978	0.27782233035975884	0.24364119412628857
346.7	0.17283748674403407	0.2725566950889298	0.23839212786407746
346.737	0.17277982367317374	0.27248457186268055	0.23832031150172697
347.16868189265597	0.1721043963168061	0.27163947499029245	0.2374789812842192
349.9	0.16771529225721132	0.26652992669478315	0.23239751420141913
350.3842245290676	0.16702182522791195	0.2656505234866486	0.23152394667843226
353.2	0.1628746981502981	0.2605261784304232	0.22644021134303455
353.6295501355039	0.16226755417196387	0.25975152493317616	0.22567266308331027
354.813	0.16057205192441432	0.2576297529178733	0.22357161291885505
356.5	0.15809715801026517	0.25466645334920424	0.22064039011326228
356.90493456752296	0.15752446772106524	0.2539416585415969	0.2199240767634531
359.7	0.1534667942037523	0.2491624498911913	0.21520600250822688
360.2106562357074	0.1528177034840213	0.2483151057180915	0.21437051154093156
363.078	0.14906981928352012	0.24354661343866815	0.20967498070312052
363.1	0.14904038349872745	0.24351051720979228	0.20963947639097016
363.5469961293318	0.14846042248418295	0.242774079313688	0.20891526200017843
366.4	0.14465923760789592	0.23815782574911726	0.20438124131988822
366.91423784024937	0.14402972203198483	0.23731775027192215	0.20355725648956555
369.8	0.14039948894639076	0.23281157732899163	0.1991428023465715
370.31266758699235	0.13980855899301428	0.23203457485172996	0.1983825858723878
371.535	0.13837987207906546	0.2301537734923114	0.19654375197849436
373.3	0.13626760532978124	0.22749854686891416	0.19395067933166338
373.74257423910643	0.13575750738075323	0.22683264033583575	0.19330094061400638
376.7	0.13225699129549504	0.22246331665576088	0.18904320339378497
377.2042493417001	0.13171518483793299	0.22171108475493512	0.18831120517813998
380.189	0.12841933679804304	0.21745722894482244	0.18417713247852174
380.2	0.12840690843021105	0.21744207296958912	0.18416241989157017
380.6979871402284	0.1278821914584303	0.216752981211728	0.18349363449900669
383.7	0.12463254796417234	0.2125911811980162	0.17946002167188227
384.2240846055061	0.1241121211987201	0.21187192841221686	0.17876389968773013
387.3	0.12097198040055142	0.20772457568264582	0.17475547236560868
387.78284145894537	0.1204919071447407	0.20706709530658507	0.17412091861204
389.045	0.1192203442184534	0.20543684627805198	0.17254852183684383
390.8	0.11741213638243483	0.2031414321571201	0.1703372214722934
391.3745601980384	0.11688955606933116	0.2024164625764893	0.16963944865358413
394.5	0.11396614119975804	0.19846440047417033	0.16584114668149624
394.9995461220647	0.11351131394758408	0.19783882635060238	0.16524078135578557
398.1	0.1106121433106847	0.1940261988646803	0.16158688125967008
398.107	0.11060615226560704	0.19401754755530215	0.16157860034266897
398.6581073580439	0.11013254221672508	0.19333342040032017	0.16092390985426278
401.8	0.10735786596659046	0.18960699191082184	0.15736295982402712
402.35055488692933	0.10689819476492314	0.18897332599433783	0.15675831880416513
405.5	0.10419676972780324	0.18534106014043217	0.15329740927399668
406.07720257003695	0.10374139471440251	0.18468234792149077	0.15267070483092257
407.38	0.10269938698706559	0.18320128590328238	0.1512626259173051
409.3	0.10112777876060842	0.18106912274289247	0.14923814353046416
409.83836717572615	0.10070535317249132	0.18045974517059027	0.14866009175908373
413.0	0.09815838236392506	0.1770391144712664	0.14542007841550295

Table D.1. Continuation of Table D.1

Beginning of table			
$\lambda[\mu m]$	F_ν(DL2014)	F_ν(PL+OTMBB)	F_ν(PL+GMBB)
413.6343684063278	0.09769792060593277	0.17637399284763242	0.14479103431309306
416.869	0.09528426466876873	0.17297399079151346	0.14158025310834965
416.9	0.09526059938532247	0.17294188994816348	0.14154997840386274
417.46552892531344	0.09485351405991602	0.17235362061949783	0.14099530616751887
420.7	0.0924624147290514	0.1690495170568054	0.13788451417632316
421.3321743847289	0.09202920102772534	0.1683978918857663	0.13727193896971387
424.6	0.08972818523872633	0.16517726007943534	0.13424906868595138
425.2346334528686	0.08930902032310684	0.16457096754410833	0.13368089900643926
426.58	0.08840816621428188	0.16326637083195317	0.13245924696052508
428.5	0.08709361103217116	0.16144334768115778	0.13075432851181892
429.17323784221577	0.08667072931732628	0.160805867924802	0.13015876607109117
432.5	0.08452298960266812	0.1577104785770204	0.12727141352806906
433.14832233764025	0.08412825003010106	0.15710182196520642	0.12670453532542342
436.5	0.08203147157759878	0.15409327560933225	0.12390706584699103
436.516	0.08202233416336652	0.15407942262517063	0.12389420251162074
437.1602248248502	0.08165279455122508	0.15351895531447204	0.12337391083565097
440.6	0.07962446524537317	0.1505200481814911	0.12059427588497726
441.209286319119	0.07927451407202088	0.14999444154030095	0.12010788606419484
444.6	0.07727482940831368	0.14712219950459896	0.11745408523391433
445.295850994266	0.07689676553938452	0.14652757142031014	0.11690553347865172
446.684	0.07613210992449194	0.145402121044499	0.11586827087980253
448.7	0.07499674321208549	0.1437447797744499	0.11434271997009522
449.42026621191417	0.07462670765129706	0.1431746404213258	0.11381853430925123
452.9	0.07278907936649523	0.14041267924975107	0.11128317772170108
453.58288255101905	0.07244735360142274	0.13987674264822691	0.11079202559923224
457.088	0.07064514813223843	0.13717456506416337	0.10831966739800702
457.1	0.07063883942658615	0.13716527590961497	0.108311179609464
457.78405383766165	0.07030764438838225	0.1366332305798098	0.10782515771416866
461.3	0.06855897211159295	0.13401834058643503	0.1054406150689818
462.02413717513	0.06822607562295106	0.13349674687899077	0.10496579555721916
465.6	0.06653658070326347	0.13091444555145293	0.10261879707748359
466.30349297427364	0.06622333508849193	0.13041215124675604	0.10216304068025407
467.735	0.06557727098823615	0.12939209129928345	0.101238220372045
469.9	0.06457808753063034	0.12788994394885908	0.09987833588193042
470.62248498412816	0.06426571071075865	0.1273788487918312	0.09941611127792457
474.2	0.06267701717554049	0.12495785884729049	0.09723052410030314
474.9814803228505	0.06235664775521522	0.12444603246001724	0.09676929198053687
478.6	0.060832295662525085	0.12206891692775801	0.09463058611688677
478.63	0.060820704138030965	0.12204954137463868	0.09461317921904684
479.38084950891067	0.060529207506014836	0.12156211474555272	0.09417540211879112
483.1	0.059045045366273724	0.11919029913470687	0.09204882542746082
483.82096649259574	0.05875639042458982	0.1187264783914532	0.09163364024787383
487.5	0.057299964973577165	0.11646283770499902	0.08961107405873235
488.30220868778844	0.05700686027107512	0.11598514949841147	0.0891850395789354
489.779	0.05645980973809878	0.11509260498854534	0.0883896169619376
492.0	0.05561883272553598	0.11377654906435587	0.08721846563909792
492.8249570040513	0.055331690361636425	0.11328988996353467	0.08678590179996797
496.6	0.05398109477245934	0.11110163587259145	0.08484428078732316
497.3895958790068	0.05371570007345576	0.11064005915526601	0.08443540487954125
501.187	0.052404243777931236	0.10851680970984308	0.08255816135229588
501.2	0.05239965437444061	0.10850980931937101	0.08255198194908149
501.99651331100796	0.052137891116573784	0.10807870357647555	0.08217154671727693
505.8	0.05085396242398327	0.10601423926662913	0.08035269167780128
506.64610089212687	0.05059065171237447	0.10556066875779622	0.07995380326722483
510.5	0.04935814147413253	0.10353081298226378	0.07817182128701165
511.3387538414332	0.049105742229505124	0.10308536656589666	0.07778142089808485
512.861	0.04864139390188678	0.10231872420099414	0.07711030267956319

Table D.1. Continuation of Table D.1

Beginning of table			
$\lambda[\mu m]$	F_ν(DL2014)	F_ν(PL+OTMBB)	F_ν(PL+GMBB)
515.2000000000002	0.04791213743123037	0.10112307299372875	0.07606498973762606
516.0748710385907	0.04766196748832367	0.10069304128655039	0.07568956598431441
520.0	0.04650839664114787	0.09875773940569993	0.07400283628070112
520.8548550577666	0.04627012964794895	0.09834142125699634	0.073640657224716
524.8	0.04514040025019878	0.09645399719282294	0.07200161540569812
524.807	0.04513856814025446	0.09645063833325089	0.07199870266683177
525.6791122018419	0.044909204568280646	0.09602999198372023	0.07163403415130172
529.7	0.0438222706179898	0.09417497149372633	0.07002911425341737
530.5480525369575	0.04360526543126589	0.09379628826285062	0.06970213545656925
534.6	0.04253988528934938	0.0919821392761137	0.0681383085817949
535.4620899273614	0.04232514626108066	0.0916008391538759	0.0678102307186136
537.032	0.04192884076171079	0.09090637314159948	0.06721319328335351
539.5	0.04129211656226355	0.08984675325203721	0.06630373808328914
540.4216420705915	0.04107500645134781	0.08944318177996413	0.06595772673970299
544.5	0.04008773930561047	0.08773403608642198	0.06449535155328494
545.4271305329836	0.03987575517938348	0.08735831015399577	0.0641745266073891
549.5	0.038919106476117335	0.08570221851424502	0.06276278848981025
549.541	0.03891018206510773	0.08568585348708305	0.0627488603600011
550.4789807854968	0.03870496782195181	0.08530937946733744	0.06242855114184971
554.6	0.03777865948226828	0.08368439783700365	0.061048538582526304
555.5776222398879	0.03757679896512218	0.08329590109290365	0.060719183615354014
559.8	0.03668047825194461	0.0816902927228817	0.05936087465992324
560.7234882852038	0.036491083828684566	0.08135056513094302	0.0590740626876828
562.341	0.036154908962089234	0.0807469152464106	0.058564817809963324
564.9	0.03561151812803603	0.07980931877490327	0.05777508934409877
565.9170163246242	0.035417463026910546	0.07943900132072966	0.057463588346316014
570.2	0.0345772652906656	0.07790644770965464	0.056176891190052106
571.1586478126435	0.034395982776158386	0.07756068431095259	0.055887107248296666
575.4	0.03357223582915192	0.0760960109735079	0.05466214592972753
575.44	0.03356524295773076	0.07608274146358956	0.05465106801254132
576.4488282925873	0.03338795215147213	0.0757461613780897	0.0543701753117123
580.8	0.03260191170759886	0.0742897456681053	0.053156822109487786
581.7880074344935	0.032428867856663476	0.0739632790941359	0.052885375902397655
586.1	0.03165320957288315	0.07256368328932718	0.051723841846269505
587.1766390733261	0.031478450996872055	0.07221158741448853	0.05143215002254493
588.844	0.031204018014999703	0.07169453767220836	0.05100439508427225
591.6	0.03074033879984179	0.07082683414672154	0.050287504825529225
592.6151812475553	0.030576394572384633	0.07051960049956844	0.050034091670588934
597.0	0.02984908876766787	0.06918797923790097	0.04893760823120411
598.1040962380944	0.029683950959390873	0.06885726932186888	0.04866584259189302
602.56	0.02899882956779135	0.06754563979178208	0.047590073607706125
602.6	0.02899254454249072	0.06753383932171973	0.04758040943127058
603.6438506075863	0.028837494483977863	0.0672241875991092	0.047326900867434005
608.1	0.02815761985202236	0.06595818880390056	0.04629269733272154
609.2349152400711	0.027999275666986106	0.06564690671377015	0.04603897265540144
613.8	0.027344448636989104	0.06439019790178523	0.045016432973080237
614.8777653810029	0.027195136512757425	0.06409740849263015	0.044778679209267834
616.595	0.026954031249205933	0.06362963955963848	0.04439915629670636
619.4	0.026551773108995286	0.0628906237144187	0.04380064926685552
620.5728806776501	0.02640208897322217	0.06257536326252305	0.04354561382666465
625.2	0.02579492598960991	0.06138415456313704	0.042584138367337224
626.3207452198692	0.02565330609584162	0.0611054491916463	0.042359690859124964
630.957	0.025051371020281616	0.0599483058110681	0.041429432994647436
631.0	0.02504566772056936	0.05993777936445586	0.04142098509101693
632.1218475812449	0.02491188667760111	0.05966158290363633	0.041199406367095646
636.8	0.024338625671943434	0.05853007806797414	0.04029342878219597
637.9766808606282	0.02420343675178055	0.058243388873040786	0.040064305050167226

Table D.1. Continuation of Table D.1

Beginning of table			
$\lambda[\mu m]$	F_ν(DL2014)	F_ν(PL+OTMBB)	F_ν(PL+GMBB)
642.7	0.02364569055157824	0.05714109198669547	0.03918534289608454
643.8857427240426	0.02351215491750919	0.0568739059215463	0.038972774022978295
645.654	0.023310300440698022	0.05646963984782007	0.03865138824071011
648.6	0.022966818653948534	0.055807474721926445	0.03812584447997764
649.8495354469889	0.022834455615458594	0.055528849536104354	0.0379050332394079
654.6	0.022317255374932825	0.05448776757796431	0.03708160467700682
655.8685659571436	0.022186413919890156	0.054207805561707754	0.036860586893604046
660.693	0.021674954164146387	0.05318746629697038	0.036056930714040966
660.7	0.02167419624978946	0.0531860459390182	0.03605581418485937
661.9433458774388	0.021551562000440564	0.05293227745801421	0.03585640683569454
666.8	0.02105927558638434	0.05193700535436683	0.03507570342705446
668.0743915695614	0.020939997195067766	0.051679571372755424	0.03487420179481503
673.0	0.020466062296313776	0.05070172744938592	0.03411034731982755
674.2622241778349	0.020350672902241677	0.050449332936968426	0.03391355037552486
676.083	0.0201819466166861	0.050104287666181226	0.03364492688924853
679.2	0.0198869118188877	0.04950327875946665	0.033177641595643265
680.5073696735207	0.019773739448391014	0.04926163602413779	0.032990122850184406
685.5	0.019329466562920374	0.04833498915981613	0.032272293757070594
686.8103588995307	0.019217305327026105	0.04809526628267841	0.032086995689864256
691.8	0.018778484008467055	0.04719822214437754	0.03139499606254687
691.831	0.018776055614657592	0.047192643989691925	0.03139069949770313
693.17172761554	0.018670440704791073	0.04694993283964068	0.03120382588433646
698.2	0.018263282401015598	0.04607718519380382	0.030533432886095363
699.5920165435375	0.01815533244226247	0.04584426819697149	0.03035495777642102
704.7	0.017748107528804125	0.04498575996712325	0.02969827701069988
706.0717714137779	0.017644589224168485	0.0447585443141641	0.02952485309525262
707.946	0.017501209422543847	0.04444633209210507	0.029286752816761675
711.2	0.01724699512007113	0.04392384005259763	0.0288890859176205
712.6115430111745	0.01714667574465266	0.04369253081631297	0.028713243338296324
717.8	0.0167675864561757	0.04287738458889924	0.028095040432444346
719.2118872221192	0.016670843861187445	0.04266350982093689	0.02793324269778384
724.4	0.01630548003258942	0.04187397414908114 5	0.027336992937051403
724.436	0.01630312022423095	0.04186861120924593	0.027332950304332148
725.8733650817246	0.01620836578705468	0.04165315047402767	0.027170603595894075
731.1	0.01585423621614782	0.04088309857100026	0.02659155499559183
732.596542821523	0.01575981955089642	0.04066117216994083	0.026425001968928226
737.9	0.015415800289471294	0.03990686626860505	0.025860266780676596
739.3819919175874	0.01532512209308912	0.03970369885122742	0.02570853601112141
741.31	0.015205515943483265	0.03943550930725551	0.025508392101012772
744.7	0.014990779132525268	0.038971248397017794	0.02516251770638889
746.2302891391108	0.014901311847633672	0.03876370595452889	0.02500815244661776
751.6	0.014578563526520925	0.03804778259552502	0.024476754474608252
753.1420165974375	0.01449233735980741	0.037840862991544495	0.024323471714092798
758.578	0.014179799042060084	0.03714117725448915	0.023806412736745903
758.6	0.01417850750127425	0.03713846553795319	0.023804413098231815
760.1177617955323	0.014096171888672885	0.036950218344495876	0.02366566163186469
765.6	0.013790457432805558	0.036267057945556375	0.023163000968762094
767.1581176779302	0.013709717945197554	0.03607585983593073	0.023022646363185476
772.7	0.01341445397558811	0.03540738259017745	0.022532940382981988
774.2636826811278	0.013335688622220397	0.035217517001033746	0.02239411926807862
776.247	0.013234405410470244	0.03498933172657035	0.02222756492003706
779.8	0.01304916239670927	0.03457262860636374	0.02192379297289528
781.4350607844542	0.012970475808247058	0.034389237327506525	0.021790394006396895
787.0	0.012695154962929084	0.03376176877156267	0.021334762084077575
788.6728615614156	0.012617999084252676	0.033576140635449725	0.021200288442977652
794.3	0.012351138133136994	0.03296219513372335	0.02075644723658115
794.328	0.012349908395782346	0.032959140458395104	0.02075424238170866
795.9777002314978	0.012277035422115331	0.03277801689666973	0.020623569029311728

Table D.1. Continuation of Table D.1

Beginning of table			
$\lambda[\mu m]$	F_ν(DL2014)	F_ν(PL+OTMBB)	F_ν(PL+GMBB)
801.7	0.012017108066864369	0.032175278473293656	0.020189789438341973
803.3501977124735	0.011946524561907947	0.03200786840226597	0.020069632077097416
809.1	0.011693678964471058	0.031421619452905745	0.01964958171543652
810.7909806731694	0.011624330987396568	0.03125189162738287	0.01952825199864808
812.831	0.011539500719830028	0.031045302905652244	0.019380686526108984
816.6	0.011379477941125496	0.03067877767418161	0.019119455452049898
818.300681586739	0.011311632507641351	0.030509935386166257	0.01899926617269638
824.1	0.011073821002530284	0.029957240763951537	0.018606800892468234
825.8799387844273	0.011007101796459985	0.0297940248537239	0.01849122202669258
831.764	0.010780254032447784	0.02925152500325678	0.01810772025909166
831.8	0.010778837158148456	0.02924827927081416	0.018105430267708108
833.5293965098188	0.01071571700252101	0.029091355807829962	0.01799477049225375
839.5	0.010491635203925936	0.028558768125333908	0.017619974883490246
841.2497049736119	0.01042965410499367	0.028401725155964497	0.017509689860546622
847.2	0.010212978961494559	0.027889019519920143	0.01715052694301433
849.0415204088755	0.01015133162515544	0.027736354697705138	0.01704387095978644
851.138	0.01008015594994809	0.027559987023447988	0.016920740975317535
855.1	0.009942824764678938	0.027231456973620442	0.01669178950460221
856.9055051268348	0.009884313173910673	0.027083383856650788	0.016588786638710943
863.0	0.009681214094837274	0.026591986931999535	0.01624766525754477
864.8423275731726	0.00962384931017032	0.02644255121465781	0.01614414832134403
870.964	0.009427840168616553	0.02596581820781922	0.015814730573531784
871.0	0.009426663682620278	0.02596313865091522	0.015812883342010947
872.852662384837	0.00937075117626944	0.02582433158813772	0.015717245140793416
879.0	0.009180007970288999	0.025361167920063068	0.015398657265727759
880.9371904473991	0.009124780431464714	0.025217633299207818	0.01530017772382973
887.2	0.00894109440158612	0.024761289721566777	0.014987727932631348
889.0965989529167	0.008888607453740217	0.024622248461566177	0.014892721420522694
891.251	0.008828155887624999	0.024472634702712562	0.014790680909445282
895.4	0.008709315246032984	0.024178718575140735	0.01459046988980363
897.3315814583519	0.008657336036372297	0.024047965271443233	0.014501623345709445
903.6	0.00848391064202763	0.023621135228116423	0.014212068833291323
905.6428379445293	0.008431948474508911	0.023484399227624506	0.01411955010214899
912.0	0.00826559949060176	0.023065869274558816	0.013836946013062046
912.011	0.008265329518416143	0.023065145803284524	0.013836458296435067
914.0310748756223	0.008215461874583826	0.022931402318188254	0.013746348172853166
920.4	0.008053777970111756	0.022526192405674172	0.013474019399980318
922.4970052592174	0.008004747494983953	0.02239800670630533	0.013388130459377461
929.0	0.007848288835518998	0.02199807017770258	0.013120600380378843
931.0413487069085	0.007802011227588521	0.02187459345990684	0.013038208346032148
933.254	0.007751145919468563	0.02173908467979479	0.012947847161091314
937.6	0.007649174985508399	0.02148457223465486	0.012778546006794194
939.6648314954691	0.00760387658341905	0.02136108297357862	0.012696509238833637
946.2	0.00745643670024439	0.020985487927169748	0.012447618099557377
948.3681866285928	0.007411518826846472	0.02086578723046853	0.012368543125744142
954.993	0.0072702946562708095	0.020497721573060304	0.012125787461882016
955.0	0.007270142401880194	0.020497341882429774	0.012125537560529821
957.1521538991856	0.007226735973305476	0.020379816177254817	0.012048233463931319
963.8	0.00708881396016523	0.020022753992145925	0.011813847130327433
966.0174799522646	0.007045969268965141	0.019903023889161417	0.011735430571521837
972.7	0.00691313565037921	0.01955617175288998	0.011508833914758414
974.9649183484096	0.006871064533218734	0.019443174713848804	0.011435233155491222
977.237	0.00682825283617295	0.01932820830307758	0.011360396548700495
981.7	0.006742457152727386	0.01910521032729535	0.011215500987845305
983.9952296278226	0.006701717746183665	0.018992065342998455	0.011142137503247699
990.8	0.006577425714976435	0.01866204282577087	0.010928581939595233
993.10918137498	0.00653814573341676	0.018549478216102144	0.010855910447172549

Appendix E: Physical parameters for each galaxy of the studied sample

Table E.1. Physical parameters. Only the first rows are shown. For each object in the sample, the table contains the following information for PL+OT_MBB: id, redshift, $\beta_{\rm FUV}$, sSFR, sM_dust, M_dust, A_FUV, IRX, age_main, L_dust, L_FUV, SFR, and M_star.

id	redshift	β_{FUV}	β_{FUV}_err	sSFR [yr^{-1}]	sSFR_err [yr^{-1}]	sM$_{dust_dl2014}$	sM$_{dust_dl2014}$_err	sM$_{dust_pwr-shock}$	sM$_{dust_pwr-shock}$_err	sM$_{dust_pwr-shock}$	sM$_{dust_pwr-shock}$_err	M$_{dust_dl2014}$ [Myrs]	M$_{dust_dl2014}$_err [Myrs]	M$_{dust_pwr-shock}$ [$L_\odot$]	M$_{dust_pwr-shock}$_err [$L_\odot$]	M$_{dust_pwr-shock}$ [$M_\odot$]	M$_{dust_pwr-shock}$_err [$M_\odot$]	A_{FUV} [$L_\odot$]	A_{FUV}_err [$L_\odot$]	IRX [$M_\odot$ yr^{-1}]	IRX_err [$M_\odot$ yr^{-1}]	age$_{main}$ [$M_\odot$ yr^{-1}]	age$_{main}$_err [$M_\odot$ yr^{-1}]	L_{dust}	L_{dust}_err	L_{FUV}	L_{FUV}_err	SFR	SFR_err	M$_{star}$	M$_{star}$_err
CANDELS_GOODSS_12	4.431	−2.144	0.146	1.007×10^{-8}	3.062×10^{-9}	0.005	0.001	0.007	0.002	0.004	0.001	1.996×10^{7}	2 060 778.415	2.802×10^{5}	2 893 210.047	1.746×10^{7}	1 802 592.837	1.567	0.094	0.652	0.050	225.655	73.748	3.193×10^{11}	3.297×10^{10}	7.081×10^{10}	3.540×10^{9}	42.620	4.403	4.233×10^{8}	1.211×10^{8}
CANDELS_GOODSS_14	5.553	−1.963	0.066	1.326×10^{-9}	1.154×10^{-10}	3.160×10^{-4}	7.183×10^{-5}	4.437×10^{-4}	1.009×10^{-4}	2.764×10^{-4}	6.283×10^{-5}	6 498 864.566	1 414 214.724	9 124 018.438	1 985 473.167	5 684 651.309	1 237 034.177	0.391	0.076	−0.212	0.108	1028.264	20.583	1.038×10^{11}	2.264×10^{10}	1.650×10^{11}	8.249×10^{9}	27.271	1.557	2.056×10^{10}	1.351×10^{8}
CANDELS_GOODSS_19	4.500	−0.558	0.109	1.977×10^{-8}	3.844×10^{-10}	0.001	2.613×10^{-4}	0.001	3.669×10^{-4}	0.001	2.286×10^{-4}	3.316×10^{7}	4 073 900.706	4.655×10^{5}	5 719 513.737	2.900×10^{7}	3 563 500.169	2.480	0.137	1.119	0.057	817.400	126.363	5.307×10^{11}	6.519×10^{10}	4.004×10^{10}	2.002×10^{9}	46.845	6.290	2.369×10^{10}	3.331×10^{8}
CANDELS_GOODSS_21	5.572	−1.385	0.224	2.961×10^{-9}	1.188×10^{-9}	0.002	6.927×10^{-4}	0.002	9.726×10^{-4}	0.002	6.060×10^{-4}	1.256×10^{7}	1 051 205.683	1.764×10^{5}	1 475 830.114	1.099×10^{7}	919 504.892	1.757	0.112	0.762	0.057	605.767	195.005	2.011×10^{11}	1.683×10^{10}	3.470×10^{10}	1.735×10^{9}	21.611	1.695	7.298×10^{9}	2.872×10^{8}
CANDELS_GOODSS_32	4.411	−0.679	0.101	9.789×10^{-9}	1.838×10^{-9}	0.005	9.893×10^{-4}	0.008	0.001	0.005	8.653×10^{-4}	3.971×10^{7}	3 097 332.169	5.575×10^{5}	4 348 469.726	3.473×10^{7}	2 709 281.474	2.463	0.091	1.086	0.041	231.668	50.424	6.353×10^{11}	4.955×10^{10}	5.204×10^{10}	2.602×10^{9}	70.705	6.688	7.225×10^{9}	1.171×10^{8}

Table E.2. Physical parameters. Only the first rows are shown. For each object in the sample, the table contains the following information for PL+OT_MBB: id, redshift, $\beta_{\rm FUV}$, sSFR, sM_dust, M_dust, A_FUV, IRX, age_main, L_dust, L_FUV, SFR, and M_star.

id	redshift	β_{FUV}	β_{FUV}_err	sSFR [yr^{-1}]	sSFR_err [yr^{-1}]	sM$_{dust}$	sM$_{dust}$_err	A_{FUV}	A_{FUV}_err	IRX	IRX_err	age$_{main}$ [Myrs]	age$_{main}$_err [Myrs]	L_{dust} [$L_\odot$]	L_{dust}_err	M$_{dust}$ [$M_\odot$]	M$_{dust}$_err [$M_\odot$]	L_{FUV} [$L_\odot$]	L_{FUV}_err [$L_\odot$]	SFR [$M_\odot$ yr^{-1}]	SFR_err [$M_\odot$ yr^{-1}]	M$_{star}$ [$M_\odot$ yr^{-1}]	M$_{star}$_err [$M_\odot$ yr^{-1}]
CANDELS_GOODSS_12	4.431	−2.144	0.146	1.115×10^{-8}	3.433×10^{-9}	0.014	0.004	1.589	0.095	0.658	0.051	205.268	68.803	3.289×10^{11}	3.444×10^{10}	5.489×10^{7}	5 747 427.271	7.200×10^{10}	3.600×10^{9}	44.298	4.648	3.973×10^{9}	1.150×10^{9}
CANDELS_GOODSS_14	5.553	−1.963	0.066	1.326×10^{-9}	1.158×10^{-10}	8.389×10^{-4}	1.928×10^{-4}	0.389	0.076	−0.219	0.109	1028.233	20.616	1.034×10^{11}	2.275×10^{10}	1.725×10^{7}	3 797 266.582	1.664×10^{11}	8.318×10^{9}	27.268	1.562	2.056×10^{10}	1.354×10^{9}
CANDELS_GOODSS_19	4.500	−0.558	0.109	2.079×10^{-9}	4.087×10^{-10}	0.004	7.390×10^{-4}	2.510	0.138	1.127	0.058	792.206	126.165	5.492×10^{11}	6.808×10^{10}	9.165×10^{7}	1.136×10^{7}	4.074×10^{10}	2.038×10^{9}	48.610	6.609	2.337×10^{10}	3.318×10^{9}
CANDELS_GOODSS_21	5.572	−1.385	0.224	2.955×10^{-9}	1.183×10^{-9}	0.005	0.002	1.761	0.112	0.762	0.057	606.651	194.588	2.019×10^{11}	1.697×10^{10}	3.370×10^{7}	2 831 886.784	3.484×10^{10}	1.742×10^{9}	21.673	1.699	7.334×10^{9}	2.878×10^{9}
CANDELS_GOODSS_32	4.411	−0.679	0.102	1.019×10^{-8}	1.902×10^{-9}	0.015	0.003	2.484	0.090	1.090	0.040	223.200	48.486	6.524×10^{11}	5.007×10^{10}	1.089×10^{8}	8 355 540.517	5.293×10^{10}	2.647×10^{9}	72.815	6.798	7.149×10^{9}	1.156×10^{9}